NASA SP-23

SESSION Q

Aerodynamics of Space Vehicles

Chairman, LAURENCE K. LOFTIN, JR.

LAURENCE K. LOFTIN, JR., *is Assistant Director of the NASA Langley Research Center. He received his B.S. degree in Mechanical Engineering from the University of Virginia in 1943.*

As Assistant Director, Loftin directs and guides research activities of the Aero-Physics Division, the Aero-Space Mechanics Division, and the Full-Scale Research Division. He initiated establishment of a space station research program at Langley and set up committees which conducted early studies in the field of space vehicle rendezvous. He is widely known for his research work in the fields of airfoils, high-lift devices, boundary-layer problems, and transonic flutter. Of particular importance was his pioneering work on the use of the variable-density feature of the transonic blowdown tunnel to accelerate the accumulation of transonic flutter information. Mr. Loftin is consultant and adviser to Government and industry in a wide variety of advanced research and development fields. He is an Associate Fellow of the Institute of the Aerospace Sciences.

50. Aerodynamic Problems of Launch Vehicles

By Robert W. Boswinkle, Jr.

ROBERT W. BOSWINKLE, JR., *Head, Aeroelasticity Branch, Dynamic Loads Division, NASA Langley Research Center, received his Bachelor of Science degree in Aeronautical Engineering from Purdue University in 1943, and his Master of Aeronautical Engineering degree from the University of Virginia in 1952. He joined the Langley staff after graduation from Purdue. Boswinkle has done extensive work in fluid mechanics and in the aerodynamic design of wind tunnels. Considered an expert in the field of aircraft flutter, he presently heads a professional staff engaged in a broad experimental and theoretical research program on the aeroelastic problems of spacecraft and aircraft from subsonic to hypersonic speeds. In this work, many new techniques have been devised for the study of flutter, buffet, and gust response. He is author or coauthor of numerous NASA technical publications on research that he has conducted at Langley. He is an Associate Fellow of the Institute of the Aerospace Sciences; Secretary, Hampton Roads Section of the Institute of the Aerospace Sciences; and a member of the Engineers' Club of the Virginia Peninsula.*

SUMMARY

The airflow about a launch vehicle causes problems which may affect the entire vehicle or may affect only localized areas; the problems can occur when the vehicle is on the launcher as well as during flight. Specific problems discussed include local steady-state loads, overall steady-state loads, buffet, ground wind loads, base heating, and rocket-nozzle hinge moments.

INTRODUCTION

Figure 50-1 indicates the subject under discussion—the aerodynamic problems of launch vehicles—and provides an orientation for the subject. Aerodynamics is shown as the hub of a wheel which has three spokes. The spokes are attached to the rim at points labeled inertia, elasticity, and heat. Aerodynamics alone and in combination with one or more of the items shown on the rim represents separate areas of investigation wherein the airflow about a launch vehicle may be an important factor. For example, the different spokes represent the areas of dynamics, aeroelasticity, and aerothermody-
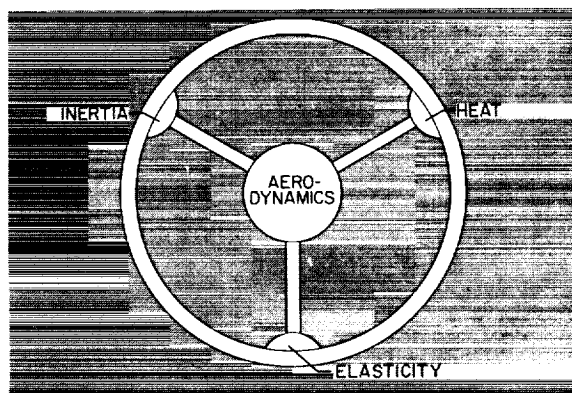

FIGURE 50-1.—Aerodynamic problems of launch vehicles.

namics. The whole wheel represents the broad area of aerothermoelasticity.

A very large number of specific problems are represented by this diagram. Only a few of the problems, as shown figure 50-2, have been chosen for discussion herein. A typical large launch vehicle is shown at the right of the fig-
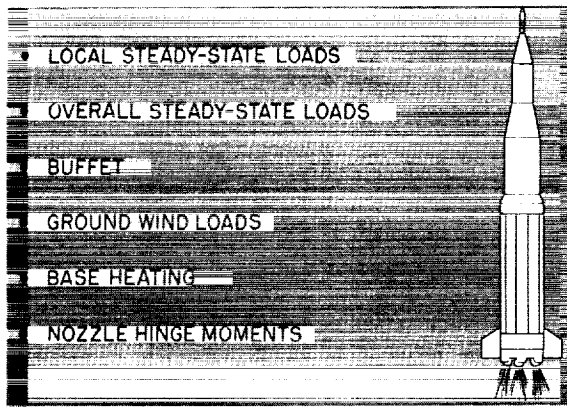
FIGURE 50-2.—Problems to be discussed.

FIGURE 50-3.—Pressure distribution. $M = 1.3$; $\alpha = 0°$.

ure. The treatment is directed more toward the problems of large launch vehicles than toward small ones; however, much of the discussion also applies to small launch vehicles.
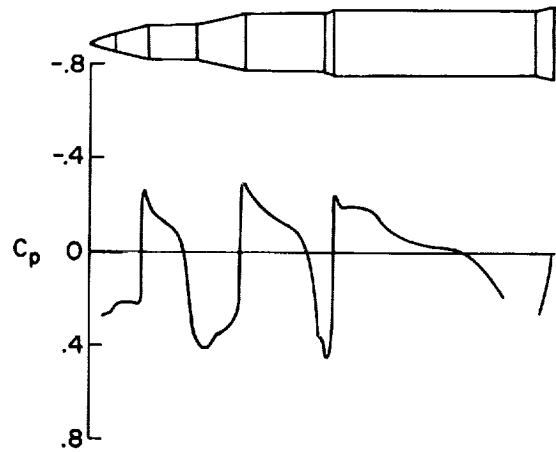
SYMBOLS

C_p	pressure coefficient, $\dfrac{p - p_\infty}{q}$
$C_{p,\text{peak}}$	peak negative pressure coefficient
f	frequency
M	Mach number
p	local static pressure
p_∞	free-stream static pressure
q	free-stream dynamic pressure
$\overline{V}(x)$	steady wind velocity
$V(x, t)$	unsteady wind velocity
V_{WIND}	horizontal wind velocity
α	angle of attack
σ_M	root-mean-square bending moment
Φ	power=spectral density

LOCAL STEADY-STATE LOADS

The first subject to be discussed is local steady-state aerodynamic loads. Figure 50-3 shows the distribution of pressure coefficients over a typical vehicle. The Mach number is 1.3 and the angle of attack is zero. Negative pressure coefficients, which indicate pressures below ambient, are shown above the horizontal axis.

Note that large changes in pressure occur in the regions of the flares. Both negative and positive pressure-coefficient peaks are obtained, and these peaks represent concentrated local loads. The negative pressure-coefficient peaks

occur at each corner where the flow is required to expand.

The peak negative pressure coefficient near the first corner of a different nose cone is shown as a function of Mach number in figure 50-4. The dynamic pressure is also shown as a function of Mach number for a typical trajectory. The local load is proportional to the product of C_p and q as shown by the solid curve. It may be seen that the local load at a Mach number of 0.8 is about four times higher than the load at maximum dynamic pressure.

The local load is a particularly important factor in the design of secondary structures, such as insulation panels or fairings. Several vehicle failures have occurred because local loads near a corner were underestimated. The assumption has been made in several instances that all aerodynamic loads are a maximum at the maximum dynamic-pressure condition. These data indicate the error of such an assumption.

Figure 50-5 again shows the variation of pressure coefficient with Mach number. The configuration is a cone-cylinder. During launch the Mach number continually increases and the Mach number scale may be thought of as a time scale. Maximum negative pressure coefficients at transonic speeds occur near the corner as indicated by the solid curve. In interstage sections of launch vehicles and also in adapter sections behind payloads, of which this configuration might be an example, the volume
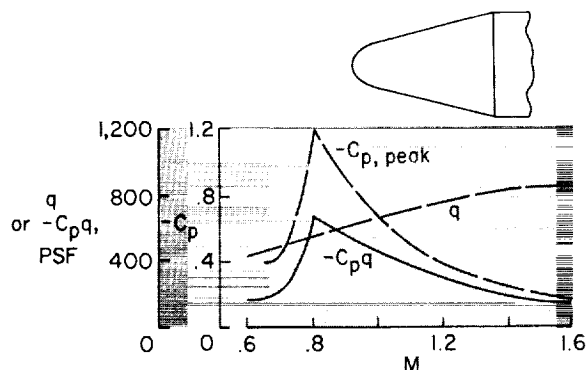
194

FIGURE 50-4.—Maximum local load for typical cone-cylinder.

enclosed is often vented to the external flow. A vent located at the corner, at point A, might reduce the net local load across the skin at point A to very low values. However, it may be seen that if the internal pressure is maintained at the value plotted here for point A, the net pressure difference across the skin at point B would be the difference between the two curves, and the local loads might become large at point B. Thus in the very important problem of locating vents, a detailed knowledge of the variation of the pressure with Mach number is required.

OVERALL STEADY-STATE LOADS

Figure 50-6 introduces the subject of overall steady-state loads. The Mach number and dynamic pressure are plotted as functions of altitude for an example trajectory. The velocity
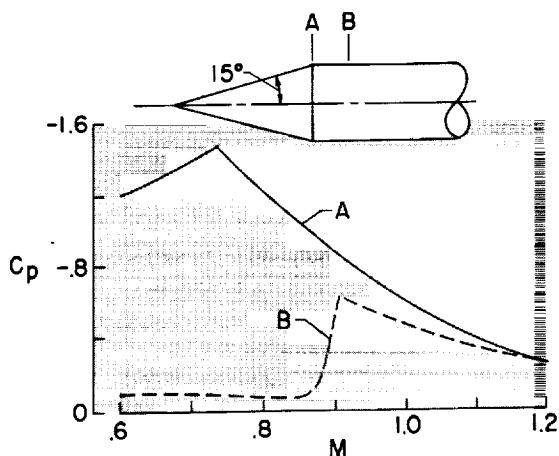

FIGURE 50-5.—Local load for cone-cylinder.

of horizontal winds which the vehicle might encounter is shown also as a function of altitude. This variation of wind velocity with altitude is about an average of the different profiles used for design purposes (ref. 1). The response of an elastic vehicle to varying horizontal winds is discussed briefly in reference 1; in the present paper, only the steady-state aspects of the problem are considered.

The horizontal winds cause the vehicle to fly at an angle of attack. Note that the maximum dynamic pressure occurs at about the same altitude as the maximum horizontal winds so that the maximum dynamic pressure and maximum
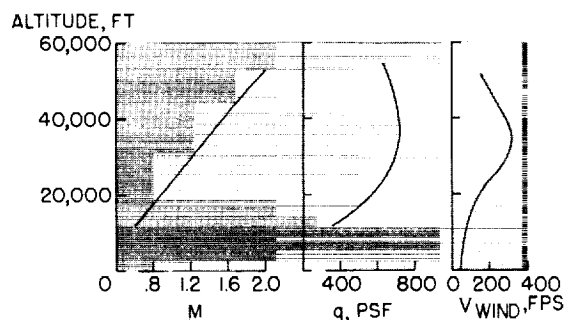

FIGURE 50-6.—Example launch-vehicle flight characteristics.

angle of attack occur at about the same time. As will be shown subsequently, the effect of angle of attack is to produce a bending moment along the vehicle length. The bending moment is nearly proportional to the product of dynamic pressure and angle of attack so that the maximum bending moments will be obtained in this region. The Mach number for large launch vehicles is usually between 1.5 and 2.0. This is a very important load condition for the design of the vehicle structure. Thus, maximum bending moments generally occur at supersonic Mach numbers, and maximum local loads (discussed previously) usually occur at high subsonic Mach numbers.

Figure 50-7 shows the pressure distribution obtained on a vehicle at an angle of attack of 8° for the top and bottom surfaces. As just discussed, the angle of attack might be caused by horizontal winds. The vehicle shown in figure 50-7 is the same as that shown in figure 50-3 and the Mach number again is 1.3. These
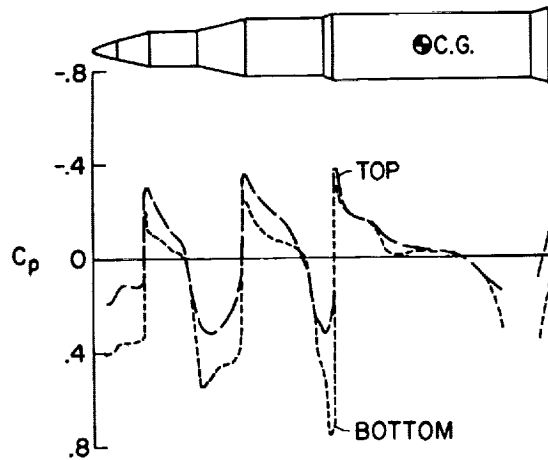
195

FIGURE 50-7.—Pressure distribution. $M = 1.3$; $\alpha = 8°$.

data indicate that at each point along the vehicle length there is an upward force on the vehicle. To calculate the pitching-moment distributions along the vehicle length, the vertical component of the pressure force is integrated circumferentially and longitudinally. Typically, for a vehicle without fins at the base, a nose-up pitching moment is obtained about the vehicle center of gravity for positive angles of attack. The pitching moment is counteracted by the stabilization system, which for example, might be swiveling rocket nozzles. The two opposing moments produce the bending moment in the vehicle.

Thus, accurate determination of the bending-moment distribution, as well as the local loads discussed previously, requires an accurate determination of the pressure distribution. No completely satisfactory theoretical method exists for computing the pressure distributions throughout the required Mach number and angle-of-attack ranges. Slender-body, shock-expansion, and piston theories give trends for some conditions, but the theoretical treatment is grossly inadequate. In practice, most designers have a collection of load distributions obtained experimentally for various shapes, and these data are used in preliminary design. For final verification, wind-tunnel studies of the configuration are often made and add more data to the collection. A much more satisfactory situation would be to have a reliable theoretical method of predicting pressure, particularly at transonic speeds.

Figure 50-8 illustrates another aspect of the need for accurate prediction of the pressure distributions. A typical vehicle is shown at the left of the figure. The upper curve is the predicted center-of-pressure location on the vehicle obtained by use of theory and the generalized experimental data available. The middle curve is the center-of-pressure location as measured in wind-tunnel studies. The center of gravity of the vehicle, shown by the bottom curve, varies with burning time. With the center of pressure ahead of the center of gravity, the vehicle is aerodynamically unstable. It may be seen that somewhat greater instability was predicted than was measured. An engine-swiveling requirement for automatic stabilization, based on the analytical prediction, would yield a considerably conservative design. The problem of attitude stabilization for large guided vehicles is discussed in reference 2.

BUFFET

Buffet is simply pressure oscillations caused by separated flow. The greatest buffet problems occur at transonic speeds where shock interactions with the separated flow augment the pressure fluctuations. Often buffet produces the greatest loads at the same locations and conditions where the local steady-state loads
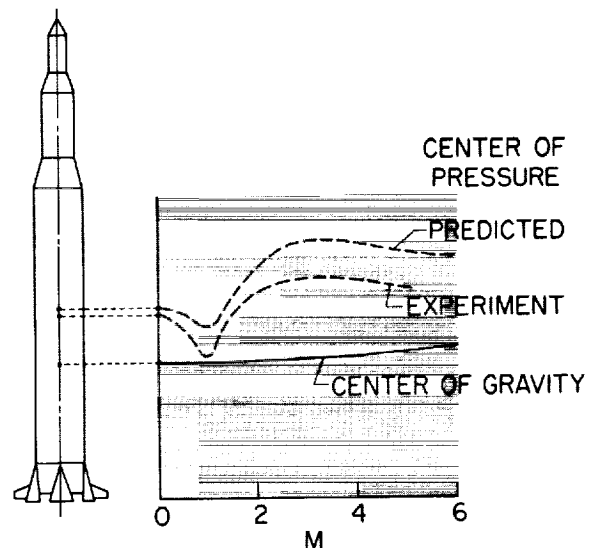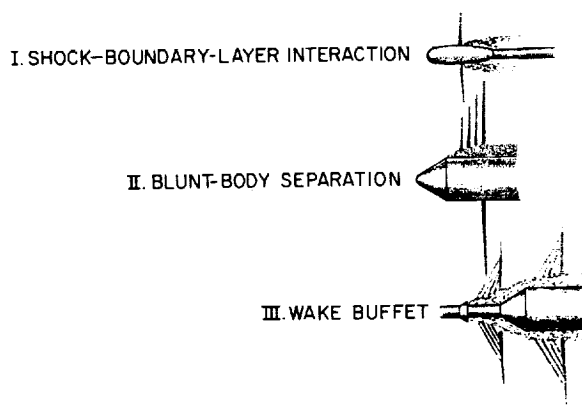

FIGURE 50-8.—Static stability.

I. SHOCK–BOUNDARY-LAYER INTERACTION

II. BLUNT-BODY SEPARATION

III. WAKE BUFFET

FIGURE 50.9.—Types of buffet flow on launch vehicles.

are a maximum. Three types of buffet which have been observed are shown in figure 50–9.

Shock-boundary-layer interaction buffet is often obtained on hammerhead configurations of the type shown. The flow resembles that over thick airfoils at transonic speeds.

Blunt-body separation buffet is characterized by unstable flow at the shoulder of a blunt cone-cylinder. At subsonic Mach numbers the flow is separated at the corner and at supersonic speeds it is attached. At Mach numbers just below one, the flow is alternately separated and attached.

Abrupt protuberances cause an unsteady wake which impinges on downstream parts of the vehicle and causes wake buffet. It is this type of buffet which appears to have caused the failure of the first Mercury-Atlas vehicle. Sub-

$\dfrac{\Phi,}{(PSI)^2}$
$\dfrac{}{CPS}$

SHOCK—BOUNDARY-LAYER INTERACTION

WAKE BUFFET

0   80   160   240
f, CPS

FIGURE 50–10.—Pressure power spectra; transonic wind-tunnel results.

sequent vehicles were strengthened and no further structural problems have been encountered.

As shown in figure 50–10, different types of buffet may have considerably different characteristics. These power spectra of the pressures show that the energy of the wake buffet is distributed over the frequency range, while most of the energy of the shock-boundary-layer interaction buffet is concentrated at low frequencies. These two types of buffet would be expected to cause considerably different elastic responses of the structure. With the buffet energy concentrated at low frequencies, overall bending modes might be excited. With distributed buffet energy, local response of the structure might be excited.

Before model buffet data such as these can be applied with confidence to full-size vehicles, the scaling relationships must be derived and verified experimentally. Simple dimensional considerations would indicate, for example, that the buffet frequency spectrum would be shifted to higher frequencies as the model scale is reduced. Buffet-pressure studies have been conducted with models which differed only in size, and the scaling laws based on the simple dimensional considerations appear to have been verified.

Since buffet is suspected to be the cause of several vehicle failures, a wind-tunnel study program on buffet pressures has been undertaken. (References 3 and 4 present results obtained to date.) The value of this buffet-pressure program is well recognized; however, considerable difficulty exists in applying the buffet-pressure data to the structural design. The obvious approach is to use experimental buffet pressures as force inputs in a dynamic analysis of the structure; however, the task of obtaining sufficiently detailed experimental data and of making the calculations appears to be overwhelming.

Figure 50–11 illustrates an alternate to such a response analysis. The two models (ref. 5) are a hammerhead configuration and a blunted cone-cylinder. The models had the same dynamic and elastic properties and were supported in a wind tunnel in such a way that they were free to respond in their elastic free-free bending modes. The response of the models
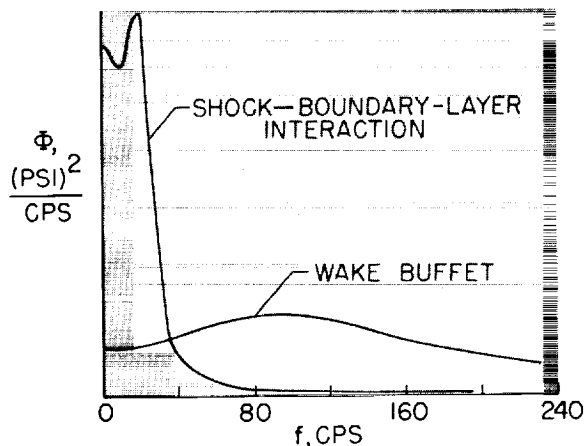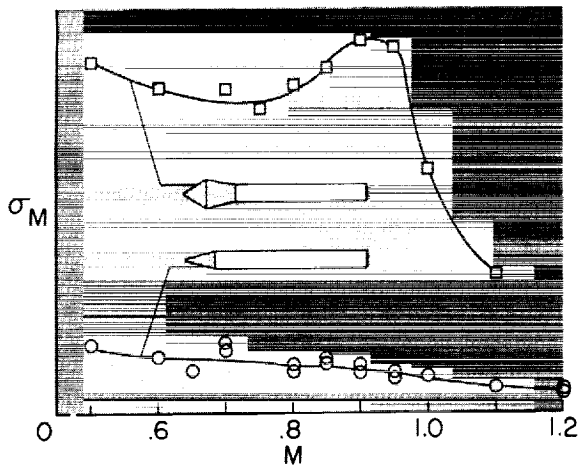
197

FIGURE 50–11.—Effect of nose shape on buffet response.

was measured in terms of the root-mean-square bending moment as a function of Mach number. Thus, the aeroelastic models were used as wind-tunnel analogues to measure the response directly. The low-level response for the cone-cylinder model is believed to be caused primarily by wind-tunnel turbulence. The much higher level response of the hammerhead configuration is due to buffeting produced by the reflex frustum.

Figure 50–12 shows the power spectra of the bending moment for the same two models at a Mach number of 0.90. Naturally, the data for the cone-cylinder model are at a very low level. Of considerable interest is that the response for the hammerhead configuration was primarily in the first two bending modes, and each mode
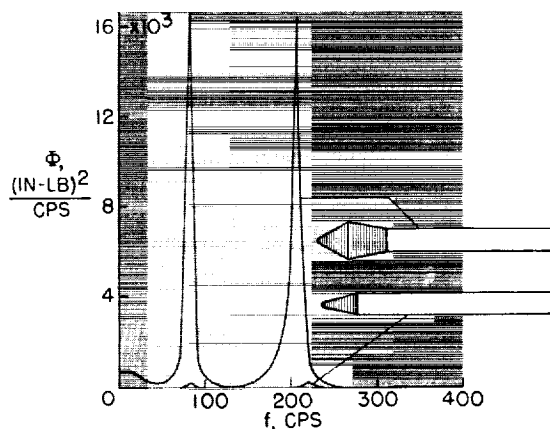

FIGURE 50–12.—Bending-moment power spectra. $M = 0.90$; $\alpha = 0°$.

contributed about equally to the total response. The technique of using aeroelastic models for buffet-response studies such as these has been used previously for aircraft wings (ref. 6). In aircraft wing models the simulation of only the first elastic wing mode usually sufficed. However, it appears from this result that at least two elastic modes must be simulated for launch-vehicle models.

To date no flight data have been available for correlation with the wind-tunnel response measurements. Correlation will have to be shown, of course, before the technique can be considered reliable for prediction of buffet response. It is anticipated that models might be satisfactory for predicting overall bending response; however, the prediction of localized response of panels might require structural replica models at small scale and might therefore be infeasible. Meanwhile, additional emphasis is needed on analytical solution of the buffet loads, using power-spectral approaches for very simple shapes.

Figure 50–12 may also be referred to in connection with another aspect of vehicle response. The sharpness of the peaks indicates that the total of the structural and aerodynamic damping was low for both modes. In fact, negative aerodynamic damping was measured in the first mode at slightly greater Mach numbers, and this situation is of concern because of the possibility that sustained or divergent oscillations of the vehicle may be produced. However, in most applications, the magnitude of any negative aerodynamic damping is very small compared with the positive damping usually provided by the structure, the thrust-vector control system, and the liquid fuel so that sustained or divergent oscillations of the vehicle have not yet materialized as a major problem.

GROUND WIND LOADS

The ground wind-loads problem is introduced in figure 50–13. The launch vehicle is shown on the launch pad during prelaunch operations. The horizontal wind is considered to consist of a steady wind vector which varies both with time and with height above the ground. The unsteady part is due to gusts and turbulence. The winds produce a steady drag
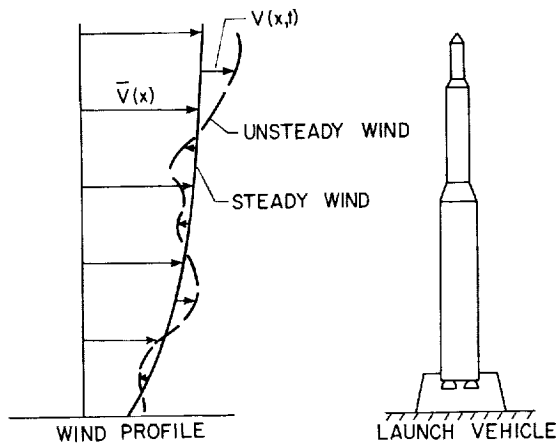
FIGURE 50–13.—Launch vehicle exposed to ground winds.

deflection and oscillatory deflections in both the lateral and drag directions. The deflections cause problems in structural strength, guidance alinement, and flight-instrumentation checkouts. The problem is of sufficient importance that design or operations changes have been required for several vehicles.

The oscillatory lateral deflections are caused primarily by the steady wind vector and no satisfactory analytical technique exists for predicting the input aerodynamics, even for two-dimensional cylinders. Wind-tunnel studies of models (refs. 7 and 8) are therefore required for lateral load predictions. Figure 50–14 shows such a model used in reference 9. On the right is shown the Scout vehicle and on the left, the dynamically and elastically scaled 15-percent wind-tunnel model. The model, complete with simulated launch tower, is shown
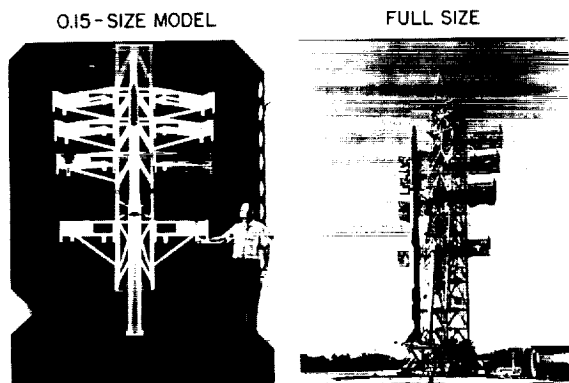

FIGURE 50–14.—Scout vehicles.

mounted in the wind tunnel. The accuracy with which ground wind response to steady winds can be simulated in wind tunnels is a moot question because of a lack of response data on full-scale vehicles which could be used for comparison with wind-tunnel data. Thus, a need exists for improving the analytical prediction methods for steady winds and for obtaining response data for full-scale vehicles.

The oscillatory drag deflections, caused primarily by the unsteady wind vector, can probably be handled analytically by using power-spectral density techniques (ref. 10). The handicap has been the lack of power-spectra information on winds near the ground. The small amount of data available have been obtained, for the most part, with conventional wind-measuring devices which are not responsive to the higher wind frequencies that can represent important dynamic load inputs to the vehicle. Thus, a need exists to determine the ground-wind properties in greater detail. A fast response anemometer under development for this purpose is described in reference 11.

BASE HEATING

Figure 50–15 illustrates the base-heating problem (refs. 12 to 15). The base of a launch vehicle which has a cluster of four rocket nozzles is shown. At high altitudes the rocket exhausts plume and intersect. Trailing shock waves are formed at the intersection of the jets. The energy of the air near the jet boundaries is too low to allow the flow to move back through the shock waves, so the flow reverses and flows toward the base of the vehicle. It escapes by flowing laterally across the base. At high altitudes, this recirculated flow of hot
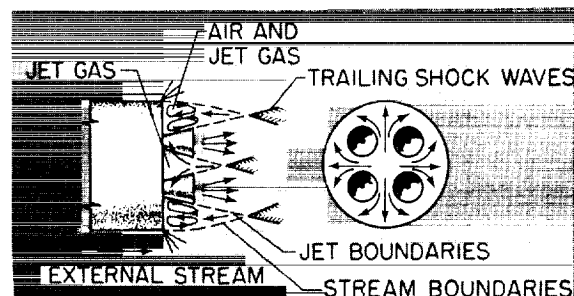

FIGURE 50–15.—Base flow for clustered nozzles.

exhaust gases reaches supersonic velocities and can cause severe damage to surfaces which are not heat protected.

The intersection of the jet exhaust with the external stream also produces trailing shock waves and a reversed flow. In this case, oxygen from the external stream combined with the fuel-rich exhaust produces a combustible mixture which could lead to burning in the base region. A much more likely source of base burning, however, is from the exhaust of the turbines which pump the propellants, since the
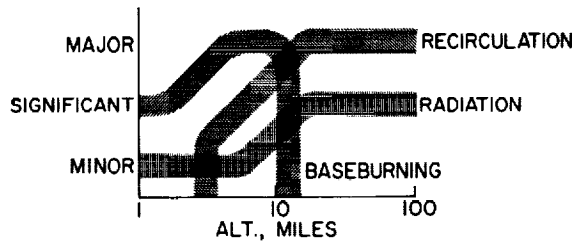

FIGURE 50–16.—Sources of base heating for clustered nozzles.

turbine exhaust is even more fuel-rich than the rocket jets.

The significance of the sources of base heating as a function of altitude in miles is shown qualitatively in figure 50–16. This figure is based on information from reference 14. Recirculation of the hot exhaust gases is indicated to be a major problem into space. At lower altitudes the jets plume less, the trailing shock strength decreases, and less of the hot gases is recirculated. At still lower altitudes, the jets do not intersect, and act instead as ejectors in pulling the external stream over the base to produce base cooling rather than heating. Base burning is indicated to be a major problem at altitudes from 3 to 10 miles. At higher altitudes, the lack of oxygen precludes combustion. Radiation is shown as the third source of base heating. Much of the radiation comes from afterburning of the rocket jet downstream of the nozzle.

Base-heating problems are generally studied by use of scaled models in wind tunnels and altitude chambers. Considerable work remains to be done in improving model-testing techniques.

NOZZLE HINGE MOMENTS

Figure 50–17 introduces the subject of the aerodynamic hinge moments on swiveling rocket nozzles. The bases of two Saturn vehicles are shown; both vehicles utilize swiveling nozzles to produce thrust-vector control.

For the C–1 Block I vehicle shown at the left, the H–1 engines are contained within the periphery of the booster and relatively large shrouds extend over the nozzles. Consequently there is very little impingement of the external flow on the nozzles.
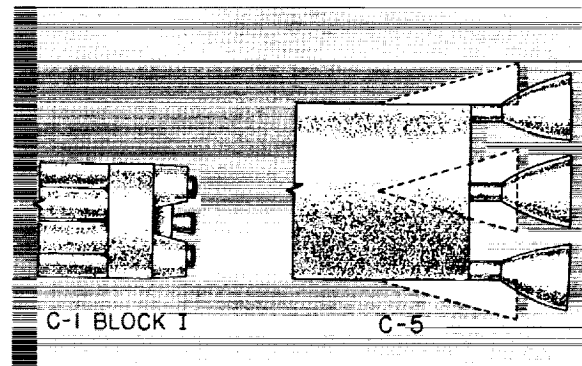

FIGURE 50–17.—Base regions of Saturn vehicles.

However, with the C–5 vehicle, the center lines of the outer F–1 engine nozzles lie nearly on the booster periphery. If no shrouds are used, the external stream impinges on a large area of the nozzles. This impingement produces very large hinge moments which lead to impractically large actuators in order to overcome the hinge moments. Elaborate backup structure would also be required for the actuator. Large shrouds may be used to shield the nozzles from the external flow, but the shroud loads then become large, and excessive backup structure is required for the shrouds. In addition, the base drag of the vehicle becomes large and the recirculation of exhaust gases at the base can become a serious problem. A probable solution is to use a shroud of moderate length, perhaps about as shown by the dashed lines, and to use scoops to guide airflow into the base area. A proper arrangement can reduce hinge moments as well as recirculation and base drag.

Wind-tunnel studies are used for predicting the nozzle hinge moments since present theories are inadequate for prediction of the complicated flow field behind the base of a launch vehicle. It would probably not be profitable to expend a great deal of effort in developing a theoretical method because the problem is so dependent on the details of the configuration and the operating conditions. However, the problem is an interesting example of the many different kinds of aerodynamic problems encountered in the design of launch vehicles.

CONCLUDING REMARKS

In conclusion, some of the aerodynamic problems of launch vehicles have been discussed. The importance of the problems has been cited and areas where additional work is required have been indicated.

REFERENCES

1. RUNYAN, HARRY L., and LEONARD, ROBERT W.: Research, Design Considerations, and Technological Problems of Structures for Launch Vehicles. NASA University Conference, 1962. (Paper no. 72 in this compilation.)
2. GEISSLER, ERNST D.: Problems in Attitude Stabilization of Large Guided Missiles. Aerospace Eng., vol. 19, no. 10, Oct. 1960, pp. 24–29, 68–71.
3. COE, CHARLES F.: Steady and Fluctuating Pressures at Transonic Speeds on Two Space-Vehicle Payload Shapes. NASA TM X–503, 1961.
4. COE, CHARLES F.: The Effects of Some Variations in Launch-Vehicle Nose Shape on Steady and Fluctuating Pressures at Transonic Speeds. NASA TM X–646, 1962.
5. HANSON, PERRY W., and DOGGETT, ROBERT V., Jr.: Wind-Tunnel Measurements of Aerodynamic Damping Derivatives of a Launch Vehicle Vibrating in Free-Free Bending Modes at Mach Numbers From 0.70 to 2.87 and Comparisons With Theory. NASA TN D–1391, 1962.
6. HUSTON, WILBER B., RAINEY, A. GERALD, and BAKER, THOMAS F.: A Study of the Correlation Between Flight and Wind-Tunnel Buffeting Loads. NACA RM L55E16b, 1955.
7. BUELL, DONALD A., and KENYON, GEORGE C.: The Wind-Induced Loads on a Dynamically Scaled Model of a Large Missile in Launching Position. NASA TM X–109, 1959.
8. EZRA, A. A., and BIRNBAUM, S.: Design Criteria for Space Vehicles To Resist Wind Induced Oscillations. [Preprint] 1081–60, American Rocket Soc., Apr. 1960.
9. JONES, GEORGE W., JR., and GILMAN, JEAN, JR.: Measured Response to Wind-Induced Dynamic Loads of a Full-Scale Scout Vehicle Mounted Vertically on a Launching Tower. NASA TN D–757, 1961.
10. BOHNE, QUINTIN R.: Power Spectral Considerations on the Launch Pad. Proc. Nat. Symposium on Winds for Aerospace Vehicle Design. Vol. I. Air Force Surveys in Geophysics, No. 140 (AFCRL–62–273(I)), Mar. 1962.
11. REED, WILMER H., III, and LYNCH, JAMES W.: A Simple Fast Response Anemometer. Presented at Conference on Low Level Winds (El Paso-Dallas, Texas), Aug. 7–9, 1962. (Sponsored by the U.S. Army Missile Support Agency and the American Meteorological Soc.)
12. SCHUELLER, CARL F.: Interactions Between the External Flow and Rocket-Exhaust Nozzle. Paper no. 59–133, Inst. Aeronautical Sci., Oct. 1959.
13. GOETHERT, B. H.: Base Flow Characteristics of Missiles With Cluster-Rocket Exhausts. Aero/Space Eng., vol. 20, no. 3, Mar. 1961, pp. 28–29, 108–117.
14. GOETHERT, B. H.: Base Heating Problems of Missiles and Space Vehicles. [Preprint] 1666–61, American Rocket Soc., Mar. 1961.
15. BEHEIM, MILTON A., and OBERY, LEONARD J.: Wind Tunnel Studies of Booster Base Heating. Paper no. 62–166, Inst. Aerospace Sci., June 1962.

51. Low-Speed Aerodynamic Research Related to the Landing of Space Vehicles

By John P. Campbell

JOHN P. CAMPBELL, *Assistant Chief, Aero-Space Mechanics Division, NASA Langley Research Center, attended the U.S. Naval Academy and graduated from Auburn University, receiving a Bachelor of Science degree in Aeronautical Engineering in May 1939. Campbell, who joined the Langley staff in November 1939, is recognized as a leading specialist in the field of research with dynamic models and has been instrumental in the development of free-flight model testing techniques at Langley.*

Campbell plans and directs low-speed aerodynamic research dealing with VTOL and STOL aircraft, conventional aircraft, and spacecraft landing configurations. He has authored or co-authored some 35 research reports and has represented the NASA in making presentations at technical conferences and before various high-level groups in this country and at international symposiums held in Brussels, Madrid, Toronto, and London.

At Auburn, he was elected to Tau Beta Pi and Phi Kappa Phi honorary fraternities and he is a member of the Engineers' Club of the Virginia Peninsula.

SUMMARY

Aerodynamic research results related to the low-speed approach and landing of space vehicles are presented. Two basic types of space vehicles are covered: those designed for vertical or near-vertical descent (which require some auxiliary device for landing) and those which perform glide landings. Spacecraft discussed include nonlifting bodies (such as the Mercury spacecraft), low-lift-drag-ratio lifting bodies, fixed-geometry glide-landing types similar to the Dyna-Soar, and variable-geometry glide-landing types which involve a change in configuration between reentry and landing. Aerodynamic characteristics are also presented for auxiliary landing aids which may replace the parachute for some recovery applications. These landing aids include the steerable parachute, the rotor-chute, and the parawing which is being developed for use in the Gemini recovery system.

INTRODUCTION

The landing of all space vehicles recovered to date has been accomplished by means of para-chutes which are relatively simple, well-proven, and reliable devices that will, no doubt, continue to be used for space-vehicle recovery in the future. Since the parachute is inherently limited to an essentially vertical and uncontrolled descent, however, other means of performing space-vehicle landings involving controlled gliding flight are also being developed to give the astronaut greater latitude in the choice of a landing site. It is the purpose of this paper to present some recent aerodynamic research results related to the various means of landing space vehicles, with particular emphasis on those means which involve the performance of glide landings.

Table 51-I shows the types of space vehicles and auxiliary landing aids to be considered, grouped into two general categories: those designed for vertical or near-vertical descent and

TABLE 51–I.—*Types of Vehicles and Landing Aids*

	Vertical landing		Glide landing
	Zero L/D	Low L/D (<1)	Moderate L/D (>3).
Reentry vehicles.	Nonlifting bodies.	Lifting bodies.	Fixed geometry. Variable geometry.
Auxiliary landing aids.	Parachute.	Steerable parachute.	Parawing. Rotorchute.

those which perform glide landings. The vertical-landing reentry vehicles can be classed either as nonlifting bodies, such as the Mercury spacecraft, or as low-lift-drag-ratio lifting bodies. Both of these types require some form of auxiliary device for landing. Glide landing vehicles are considered to be those which have a large enough value of subsonic lift-drag ratio (greater than about 3 or 4) to permit safe glide landings to be made consistently. These vehicles may be either fixed-geometry types, such as the Dyna-Soar, or variable-geometry types which involve a change in configuration between reentry and landing.

SYMBOLS

L	lift, lb
D	drag, lb
C_L	lift coefficient, $\dfrac{\text{Lift}}{qS}$
C_N	normal-force coefficient, $\dfrac{\text{Normal force}}{qS}$
C_D	drag coefficient, $\dfrac{\text{Drag}}{qS}$
C_m	pitching-moment coefficient, $\dfrac{\text{Pitching moment}}{qS\bar{c}}$
C_n	yawing-moment coefficient, $\dfrac{\text{Yawing moment}}{qSb}$
C_l	rolling-moment coefficient, $\dfrac{\text{Rolling moment}}{qSb}$
q	dynamic pressure, lb/sq ft; pitching velocity, radians/sec
S	wing area, sq ft
b	wing span, ft
$\bar{c}$	mean aerodynamic chord, ft
α	angle of attack, deg
β	angle of sideslip, deg
ϕ	angle of bank, deg
$\dot{\alpha}$	rate of change of angle of attack, radians/sec
p	rolling velocity, radians/sec
r	yawing velocity, radians/sec; rotor radius, ft
δ_a	aileron deflection, deg
δ_r	rudder deflection, deg

V	free-stream velocity, ft/sec
V_s	rate of descent, ft/sec
z	vertical distance from center of gravity to wing pivot, ft
W	weight, lb
I_X	moment of inertia about X-axis, slug-ft^2
I_Z	moment of inertia about Z-axis, slug-ft^2
P	period of oscillation, sec
$T_{1/2}$	time to damp to one-half amplitude, sec

$$C_{L_\alpha}=\frac{\partial C_L}{\partial \alpha} \qquad C_{N_\alpha}=\frac{\partial C_N}{\partial \alpha} \qquad C_{m_\alpha}=\frac{\partial C_m}{\partial \alpha}$$

$$C_{n_\beta}=\frac{\partial C_n}{\partial \beta} \qquad C_{l_\beta}=\frac{\partial C_l}{\partial \beta} \qquad C_{l_p}=\frac{\partial C_l}{\partial \frac{pb}{2V}}$$

$$C_{n_r}=\frac{\partial C_n}{\partial \frac{rb}{2V}} \qquad C_{n_p}=\frac{\partial C_n}{\partial \frac{pb}{2V}} \qquad C_{m_q}=\frac{\partial C_m}{\partial \frac{q\bar{c}}{2V}}$$

$$C_{m_{\dot{\alpha}}}=\frac{\partial C_m}{\partial \dot{\alpha}} \qquad C_{l_{\delta_a}}=\frac{\partial C_l}{\partial \delta_a} \qquad C_{n_{\delta_a}}=\frac{\partial C_n}{\partial \delta_a}$$

$$C_{n_{\delta_r}}=\frac{\partial C_n}{\partial \delta_r}$$

Subscripts:
MAX maximum
DYN dynamic

NONLIFTING BODIES

It may be recalled that astronauts Glenn and Carpenter both experienced unstable oscillations of their Mercury spacecraft after expending all their control fuel during the final subsonic portion of descent, and it was necessary in both cases to deploy the drogue parachute early in order to stablize the spacecraft. (See refs. 1 and 2.) An illustration of this form of dynamic instability is presented in figure 51–1 which shows the oscillations obtained in free-flight tests of a Mercury-type spacecraft model in the Langley 20-foot free-spinning tunnel. The angle of attack measured in the plane of the oscillation is plotted against full-scale time for
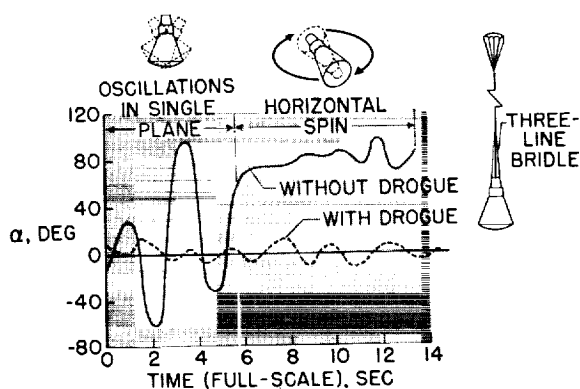
FIGURE 51-1.—Dynamic stability of nonlifting vehicle.

FIGURE 51-2.—Stability parameters of nonlifting vehicle.

the model with and without a drogue parachute installed. The oscillation for the model without the drogue is very unstable and builds up quickly to very large angles, after which the model starts a horizontal spinning motion at high angles of attack. With the drogue deployed, however, the amplitude of the oscillation is restrained to an acceptably small value. These model tests apparently predicted quite well the character of the oscillations experienced on the full-scale Mercury spacecraft. (The drogue of the full-scale spacecraft was deployed in both cases before the horizontal spinning motion could develop.)

Some of the important aerodynamic parameters involved in this dynamic stability problem of blunt-faced Mercury-type spacecraft are shown in figure 51-2. Plotted against angle of attack (from 0° to 180°) are shown low-speed test data for the parameters C_{N_α} (which is roughly equivalent to C_{L_α}, the lift-curve slope), C_{m_α} (the static-longitudinal-stability parameter), and $C_{m_q}+C_{m_{\dot\alpha}}$ (the damping-in-pitch parameter). The data show that at 0° angle of attack, which represents vertical descent with the blunt face down, the value of C_{N_α} is negative, indicating a reversed lift-curve slope, the value of C_{m_α} is also negative, indicating positive static stability, and the damping parameter $C_{m_q}+C_{m_{\dot\alpha}}$ is positive, indicating negative damping of any pitching motion that develops. This combination of parameters, which results from the separated flow condition behind the blunt face of the spacecraft, is primarily responsible for the unstable oscilla-
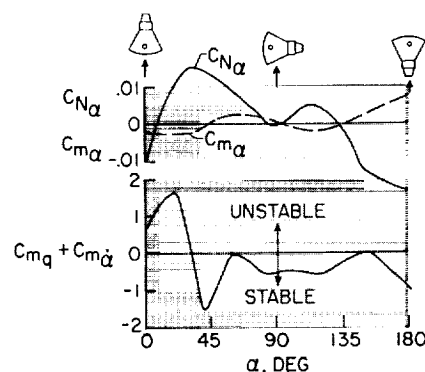
tions obtained in flight. Research has shown that these characteristics are not peculiar to the particular Mercury configuration but are common to all bluff-body nonlifting configurations of this general type which descend vertically with the blunt face down.

LIFTING BODIES

Three examples of lifting-body configurations are shown in figure 51-3. These lifting-body vehicles may be considered to bridge the gap between the vertical-descent and glide-landing types since they can be designed to have subsonic lift-drag ratios from less than 1 to as high as 4 or 5. The configuration in the upper left-hand part of figure 51-3 is a blunt half-cone, which has an L/D less than 1 and therefore requires some auxiliary landing device. Configurations of this general type are usually quite stable in their steep subsonic descent and do not experience the unstable oscillations ob-
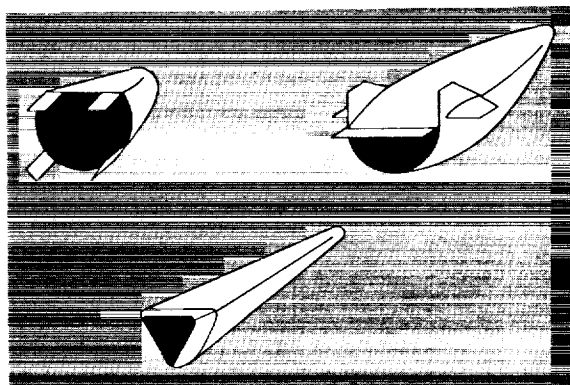

FIGURE 51-3.—Lifting-body vehicles.

205

tained with the blunt-faced Mercury-type space-craft. The other two configurations shown in this figure are slender half-cone and pyramid shapes which can, by proper design, achieve lift-drag ratios high enough for performing glide landings. In order to obtain these values of L/D, careful use must be made of boattailing to reduce the large base area of the bodies. (See ref. 3.)

GLIDE-LANDING VEHICLES

Subsonic Lift-Drag Ratio

Figures 51-4 and 51-5 illustrate what can be done to increase the subsonic L/D of both lift-ing-body and winged reentry vehicles. Figure 51-4 shows the maximum subsonic L/D for a variety of configurations plotted against a non-dimensional volume parameter (volume to the two-thirds power divided by wing area). The results shown are for trimmed conditions and a small amount of longitudinal stability. These data show that, as would be expected, the higher values of L/D are associated with the winged configurations which have the least fuselage and wing volume for a given wing area, whereas the lower values are associated with the lifting bodies which have the greater vol-ume-to-wing-area ratios. These data were ob-tained at low Reynolds numbers; a few tests at higher Reynolds numbers have indicated that L/D values for the corresponding full-scale reentry vehicle in some cases may be as much as 0.5 to 1.0 greater than these values. The configurations illustrated in figure 51-4 were designed primarily with the hypersonic flight
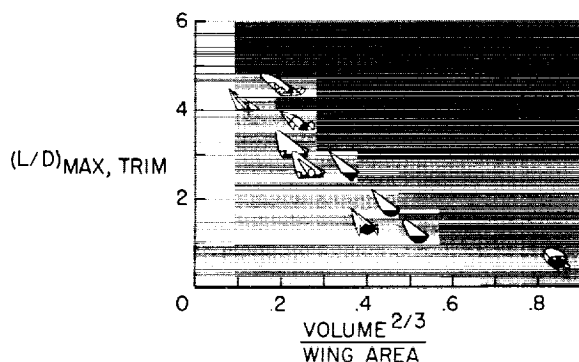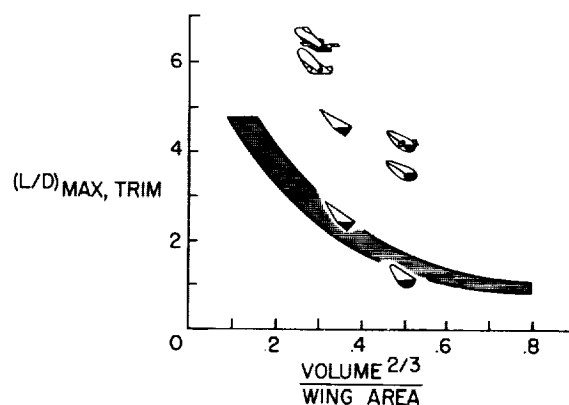

FIGURE 51-5.—Configurations designed for higher lift-drag ratio. Trimmed conditions.

condition in mind and with little or no atten-tion given to obtaining a good subsonic L/D. Despite this, some of the winged configurations have a fairly good subsonic $(L/D)_{MAX}$.

Figure 51-5 shows that substantial increases in subsonic L/D for both winged and lifting-body vehicles can be attained when some effort is made to design the vehicles for the low-speed case. The shaded area represents the region in which the $(L/D)_{MAX,TRIM}$ values for the con-figurations of figure 51-4 were located. Boat-tailing the base of the half-cone and pyramid-shaped vehicles increased the L/D values substantially. Adding control surfaces to the half-cone vehicle resulted in a further increase in L/D. In the case of one winged reentry con-figuration, an $(L/D)_{MAX}$ of about 6 was ob-tained when the configuration was specially modified to achieve high L/D at low speeds. With these modifications, this configuration had a thick, highly cambered wing and a teardrop fuselage with a small base area. The hyper-sonic L/D was reduced by these changes, but the hypersonic L/D values for the half-cone and pyramid-shaped vehicles were relatively unaf-fected by boattailing. Another method for ob-taining high L/D for landing is the use of a variable-geometry vehicle, such as the one shown at the top of figure 51-5, which has a sub-sonic $(L/D)_{MAX}$ of about 7.

Variable-Geometry Vehicles

Some subsonic aerodynamic data for the var-iable-geometry vehicle shown in figure 51-5 are
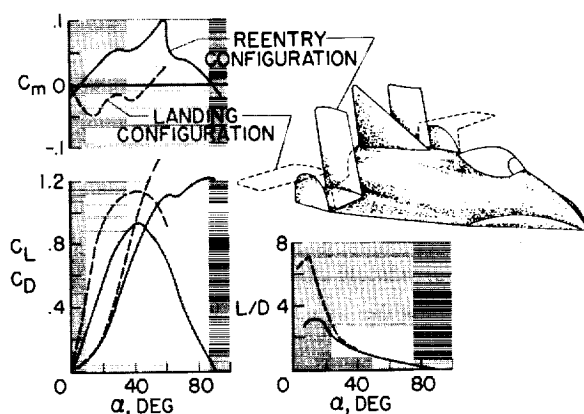

FIGURE 51-4.—Maximum lift-drag ratio. Trimmed conditions.

FIGURE 51-6.—Aerodynamics of variable-geometry vehicle.

FIGURE 51-7.—Aerodynamic-center location at low subsonic speed.

presented in figure 51-6. (See refs. 4 and 5 for additional information.) In the reentry configuration, the wing tips of this vehicle are folded up to protect them from high heating rates during reentry at high angles of attack. For landing, the surfaces are folded down. The pronounced increase in L/D produced by extending the surfaces is shown in the plot at the lower right. The pitching-moment plot at the upper left illustrates the basic principle of the variable-geometry concept. In the reentry configuration with the wing tips retracted, the vehicle is designed to have zero pitching moment at an angle of attack of about 90° so as to be trimmed for vertical or near-vertical descent. The negative slope of the pitching-moment curve at $\alpha=90°$ indicates static longitudinal stability for this condition; but, like the blunt-faced Mercury-type vehicles discussed earlier, this configuration has a negative lift-curve slope and negative damping in pitch at an angle of attack of 90° and, consequently, has an unstable pitching oscillation in subsonic vertical descent. In the landing configuration, the extended surfaces provide longitudinal stability and trim in the low angle-of-attack range. This variable-geometry configuration is, of course, only one of many possible variable-geometry schemes which have been considered.

Stability and Control of Glide-Landing Vehicles

Some of the effects of wing sweep on the stability and control characteristics of glide-landing reentry vehicles with highly swept
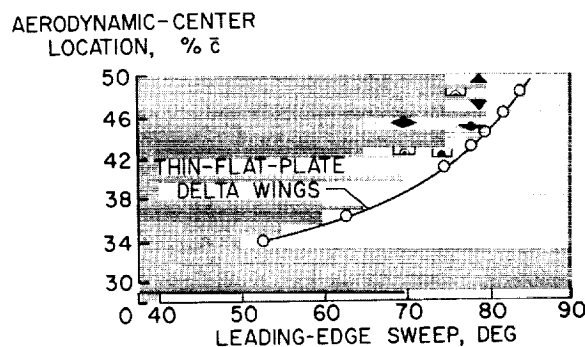
wings are presented in figures 51-7 to 51-10. Figure 51-7 shows the variation of aerodynamic-center location with leading-edge sweep for thin-flat-plate delta wings. The aerodynamic center must, of course, be aft of the center of gravity for longitudinal stability. The data indicate that there is a systematic variation in aerodynamic-center position with sweep approaching the theoretical value of 50 percent $\overline{C}$ at 90° sweep. Also shown in figure 51-7 are the aerodynamic-center locations for several reentry vehicles as given by symbols showing their cross-sectional views. These data indicate that a rearward (or stabilizing) shift in aerodynamic center generally results when the wing is very thick, when a large fuselage is added, or when wing-tip vertical tails are used.

For this same series of thin-flat-plate delta wings, figure 51-8 shows the variation with sweep angle of the effective-dihedral parameter C_{l_β}, the damping-in-roll parameter C_{l_p}, and the ratio of the yawing moment of inertia to the rolling moment of inertia I_Z/I_X. Although these data are for thin delta wings at a lift coefficient of 0.60, the trends shown are considered to be generally representative of highly swept reentry configurations for a fairly wide lift-coefficient range. As the sweep angle increases, the effective dihedral $(-C_{l_\beta})$ increases to very large values, the damping in roll $(-C_{l_p})$ drops off and even becomes unstable at the higher angles, and the ratio of yawing inertia to rolling inertia becomes very large. This combination of changes leads to a lightly damped Dutch roll oscillation and, as would be expected with a high yawing inertia
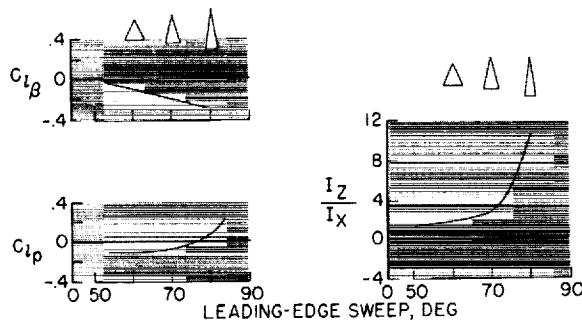
FIGURE 51-8.—Aerodynamic and inertia parameters of thin delta wings. $C_L=0.60$.

and low rolling inertia, the oscillation is almost a pure rolling motion about the body X-axis. (See ref. 6.)

An illustration of the Dutch roll stability problem for a typical highly swept, glide-landing reentry vehicle is presented in figure 51-9. In the left-hand plots, the calculated period and damping of the Dutch roll oscillation for subsonic flight are plotted against angle of attack. The decrease in the damping parameter $\frac{1}{T_{1/2}}$ with increasing angle of attack indicates a reduction in Dutch roll damping to unsatisfactorily low values at angles of attack around 30°. In model flight tests of this configuration in the Langley full-scale tunnel, a very lightly damped oscillation, involving primarily a rolling motion about the body axis, was obtained.

Research has indicated that a very effective means of obtaining satisfactory Dutch roll damping with highly swept reentry vehicles of this type is to use a roll-rate damper, that is, an automatic stabilization device which operates the roll control in response to rate of roll. The plot on the right-hand side of figure 51-9 shows the relative effect of roll and yaw dampers for this reentry configuration. The damping factor $\frac{1}{T_{1/2}}$ is plotted against values of the damping-in-roll derivative $-C_{l_p}$, the damping-in-yaw derivative $-C_{n_r}$, and the cross derivative C_{n_p} (yawing moment due to rolling velocity). These results show that an increase in $-C_{l_p}$ (representing the use of a roll damper) produced a large increase in the damping of the Dutch roll oscillation, whereas an increase in $-C_{n_r}$

(representing the use of a yaw damper) produced only a very small increment of damping. Another point of interest here is that the derivative C_{n_p} also has a large effect on the damping. This effect can be significant in cases where the ailerons used for roll damping produce large yawing moments. In such cases, the damper will produce C_{n_p} as well as C_{l_p}; and the C_{n_p} contribution will be stabilizing when the yawing moments are adverse and destabilizing when the yawing moments are favorable.

Figure 51-10 presents some information on directional stability which indicates that highly swept reentry configurations are not likely to experience directional stability problems. Plotted against sweep angle are values of two directional stability parameters, C_{n_β} and $(C_{n_\beta})_{DYN}$, for the same series of thin-flat-plate delta wings covered earlier. The values of the static directional stability parameter C_{n_β} are low and become negative at the higher sweep angles. On the other hand, the dynamic directional stability parameter $(C_{n_\beta})_{DYN}$, which is defined as $C_{n_\beta}-C_{l_\beta}\frac{I_z}{I_x}\sin\alpha$, increases rapidly to large positive values at high sweep angles because of the large positive increases in I_z/I_x and negative increases in C_{l_β}. It has generally been found that the parameter $(C_{n_\beta})_{DYN}$ is a better criterion for directional divergence than the static stability parameter C_{n_β}. For example, it has been found possible to fly airplane models with large negative values of C_{n_β} as
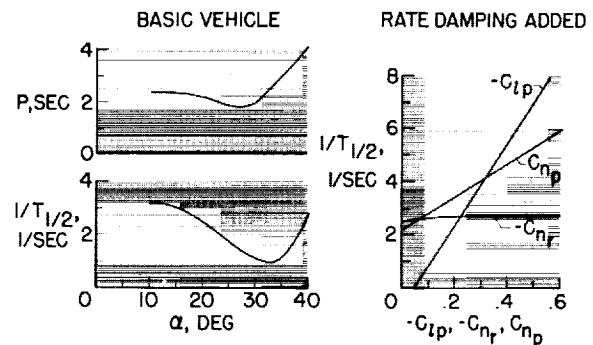

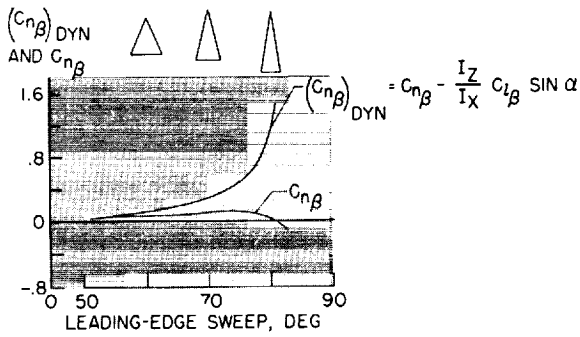FIGURE 51-9.—Dutch roll stability. Glide-landing reentry vehicle.

FIGURE 51-10.—Directional stability parameters of thin delta wings. $C_L=0.60$.

long as $(C_{n_\beta})_{DYN}$ remains positive. It would appear, therefore, that directional-divergence problems are not likely to be experienced with highly swept reentry vehicles because of their large values of effective dihedral and large ratios of yawing inertia to rolling inertia.

It has been found, however, that directional problems can be encountered with such configurations because of the adverse yawing moments produced by aileron control. This point is illustrated by the data of figure 51-11. The upper part of the figure shows the ratio of yawing moment to rolling moment produced by aileron deflection $C_{n_{\delta_a}}/C_{l_{\delta_a}}$ for two reentry configurations—one having wing-tip vertical tails and the other a single center vertical tail. The data show that aileron deflection produced small favorable yawing moments over most of the angle-of-attack range for the configuration with the center tail but produced large adverse yawing moments for the wing-tip tail configuration. The large adverse aileron yawing moments are associated with the large induced loads produced on the vertical-tail surfaces by differential deflection of the ailerons. The plot at the bottom of figure 51-11 shows that the rudder effectiveness $C_{n_{\delta_r}}$ remained about constant with angle of attack for the center-tail model, but decreased with increasing angle of attack for the model with the wing-tip tails and became practically zero at an angle of attack of 40°.

The significance of these results was clearly shown in model flight tests of the wing-tip tail configuration. It was not possible to fly the model with ailerons-alone control because the large adverse yawing moments produced by the ailerons resulted in directional divergences. At the lower angles of attack these yawing moments could be counteracted by the use of rudder control, and successful flights could be made. At the higher angles of attack where the rudder effectiveness had dropped off appreciably, however, the adverse yawing moments produced large yawing motions and the model became uncontrollable. It appears that configurations of this type with wing-tip tails will need a powerful rudder control and may require interconnection of the ailerons and rudders for satisfactory lateral control at subsonic speeds.

AUXILIARY LANDING AIDS

Since the conventional parachute has been under development for so long and its characteristics generally understood, it will not be discussed in this paper except to point out that the Mercury recovery system involves the use of main and reserve parachutes of the ring-sail type which are deployed first in a reefed condition to minimize the opening shock loads. These are rather porous parachutes which provide a relatively stable descent.

An interesting development of the conventional parachute that has been receiving some attention is the steerable parachute which is intended to provide enough maneuvering capability to afford some choice of landing site. One example of the steerable parachute is illustrated in figure 51-12. This is a flapped parachute which was tested in the Ames 40- by 80-foot tunnel. (See ref. 7.) The flap was formed
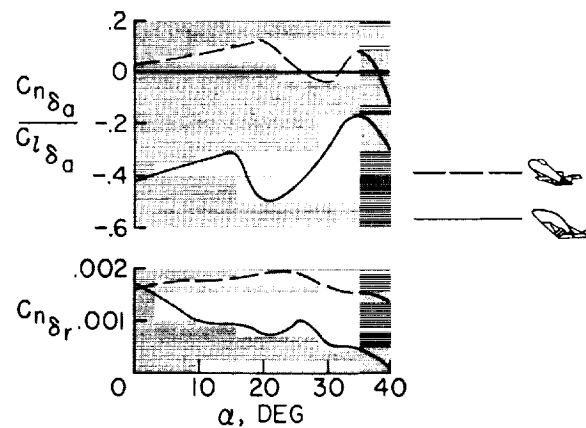

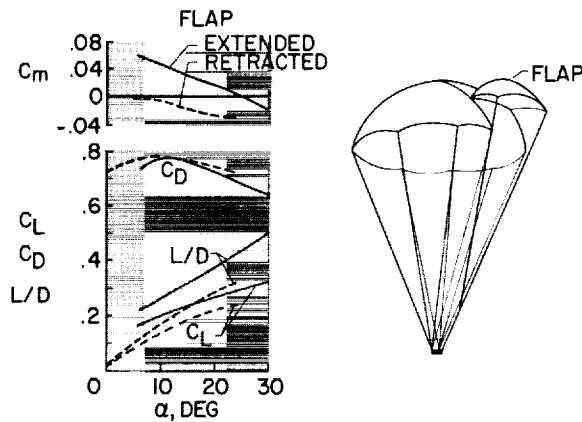FIGURE 51-11.—Lateral control parameters.

209

FIGURE 51-12.—Aerodynamics of steerable parachute.

by allowing a portion of the skirt to deflect upward as illustrated in the sketch. The pitching-moment data in the upper left-hand plot show that extending the flap caused the parachute to trim at an angle of attack of about 25° (compared with 0° with the flap retracted). At this angle of 25° with flap extended, an L/D of about 0.4 or 0.5 was obtained. This result indicates that the flap does provide a limited amount of glide-path control.

Parawing Recovery Systems

A recovery device which provides a much greater degree of maneuvering capability is the parawing which is now being developed for use in the Gemini program as a replacement for the parachute. (See refs. 8 and 9.) Figure
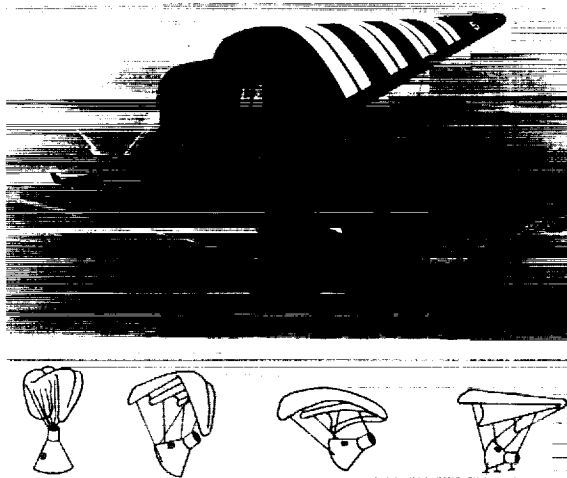

FIGURE 51-13.—Parawing recovery system.

51-13 is an artist's conceptual drawing of the Gemini parawing recovery system. This illustration is not accurate in all details but does serve to illustrate the system. It is anticipated that the glide capability provided by such a system will greatly increase the chances of reaching a safe landing site. But it is generally agreed that in order to provide greater capability than the parachute, the parawing will almost certainly be a more complex system and is also likely to have more aerodynamic problems than the parachute. Maneuvering of the parawing vehicle is accomplished by differential lengthening and shortening of the fore-and-aft lines for pitch control and of the wing-tip lines for roll control. In other words, the center of gravity of the system is effectively shifted to provide control moments. The main structural members of the parawing—the keel and leading edges—are inflatable tubes which are stowed in the deflated condition prior to deployment.

The proposed deployment sequence for the Gemini recovery system, illustrated schematically at the bottom of figure 51-13, involves a carefully timed series of steps including release of the stowed parawing, inflation of the keel and leading edges, and extension of all the supporting lines. Research to date has indicated that careful attention must be given to parawing deployment to insure success since a slight error in rigging or timing may lead to serious stability and trim problems which could prevent a successful recovery.

Figure 51-14 presents some low-speed aerodynamic data obtained in tests of a large-scale model of a parawing with a thick rounded leading edge generally similar to that being considered for the Gemini recovery system. In this figure are shown various coefficients and parameters plotted against the angle of attack of the keel from negative to large positive angles. It should be noted that the lift curve is very nonlinear near zero lift between angles of attack of about −5° and 15°. This is the range in which the fabric of the parawing goes slack, resulting in a fabric flapping problem which may be experienced even up to angles of attack of 20° or 25° in some cases in the form of a trailing-edge flutter. It is of interest to note that at an angle of attack of 55° and a lift
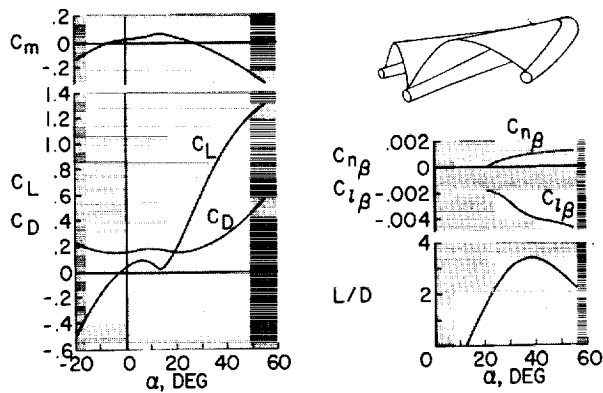
FIGURE 51-14.—Aerodynamics of parawing.

coefficient of about 1.3 the wing has not yet stalled. In the plot at the top of figure 51–14 it can be seen that the pitching-moment curve has a normal stable slope at angles of attack above about 15°, but below this angle the parawing is statically unstable. Research has indicated that this instability at low angles of attack, which is an inherent characteristic of the parawing because the fabric goes slack, can be a serious problem and may under some conditions even result in a tendency to enter an end-over-end tumbling motion. It thus appears desirable to operate the parawing at all times well away from this critical low-angle-of-attack range in order to avoid this problem.

The upper plot in the right-hand side of figure 51–14 shows small positive directional stability (C_{n_β}) and a large value of effective dihedral $(-C_{l_\beta})$ which are typical values for parawings. As for dynamic lateral stability, the Dutch roll damping observed in parawing flight tests to date has been generally satisfactory, but there have been some cases of poor Dutch roll damping when very large destabilizing bodies such as boosters were suspended beneath the parawing.

The plot at the bottom right-hand side of figure 51-14 shows that a maximum L/D of about 3.5 was obtained at an angle of attack of almost 40°. This is a typical value for parawing configurations tested to date with large inflatable leading edges. It is possible to realize considerably higher values of L/D by going to configurations with smaller leading edges, higher aspect ratio, and changes in the wing canopy shape as indicated in figure 51–15.

This figure presents data for parawings with rigid, streamlined leading edges having two different aspect ratios (2.8 and 6), and two different canopy shapes which may be called conical and cylindrical. With the conical canopy shape, which has been used on most parawings to date, the canopy assumes the shape of a portion of the surface of a cone; whereas with the cylindrical canopy, the canopy assumes the shape of a portion of a cylinder having its axis parallel to the keel. The long-dash—short-dash curve shows a maximum L/D of about 6 for the aspect-ratio-2.8 conical-canopy wing. The fact that the L/D of this wing is higher than that for the wing of figure 51–14 is attributed primarily to its smaller, more streamlined leading edges. The long-dash line shows that increasing the aspect ratio of the conical-canopy wing to 6 causes an increase in L/D to almost 8. Changing to the cylindrical-canopy shape increases the L/D to 10 for the aspect-ratio-2.8 wing and to almost 14 for the aspect-ratio-6 wing. It should be pointed out that these large increases in L/D are obtained at the expense of a somewhat more complicated structure and that more information is needed on these higher L/D configurations before it can be determined how practical they will be. In any event, one important conclusion that can be drawn from these data is that it should eventually be possible by careful design and development to increase the L/D of parawing re-
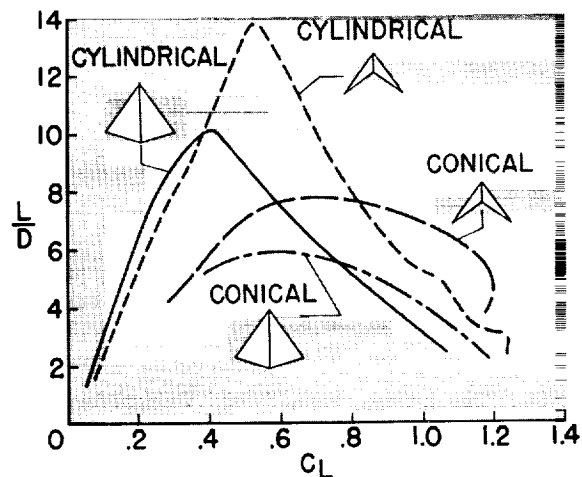
FIGURE 51–15.—L/D values for parawings with conical and cylindrical surfaces.
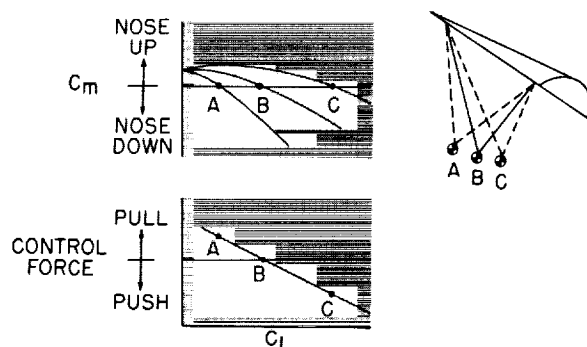
FIGURE 51-16.—Parawing longitudinal control.

FIGURE 51-17.—Parawing lateral control.

covery systems considerably above the value of about 3.5 expected for Gemini.

The basic characteristics of parawing longitudinal control by center-of-gravity shift are illustrated in figure 51-16. The upper plot in this figure shows the pitching-moment curves resulting when the center of gravity is shifted forward from B to A or rearward from B to C. When the center of gravity is shifted forward to trim at a lower lift coefficient (point A), an increase in stability is also obtained as indicated by the increased slope of the curve. Conversely, there is a reduction in stability when the parawing is trimmed to the higher lift coefficient (point C). Presented in the plot at the lower left is a typical variation of control force with lift coefficient which shows that the stick forces are unstable—that is, a pull force is required for trim at the lower lift coefficients and a push force at the higher lift coefficients. (Additional information on parawing control forces is presented in ref. 9.) Because the stick forces are unstable and also rather large for a parawing large enough to carry the Gemini spacecraft, a powered control system is indicated for such applications.

Figure 51-17 illustrates the parawing lateral control, which is obtained by a lateral center-of-gravity shift that also corresponds to a banking of the wing for control. The formula and sketch at the upper left indicate that the net rolling-moment coefficient produced is not only a function of the lift coefficient and the distance the lift vector passes from the center of gravity but is also affected by the factor in parentheses which includes the effective dihedral parameter $-C_{l_\beta}$, the directional stability parameter C_{n_β},
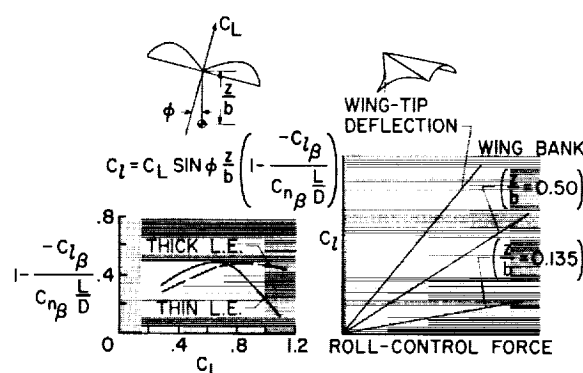
and the lift-drag ratio L/D. This factor is used to account for the fact that a wing-bank control produces adverse yawing moments which act through the stability parameters to effectively reduce the rolling moment. At the lower left, values of this factor for parawings with thick and thin leading edges are shown plotted against lift coefficient. The factor never gets larger than about 0.5 and, in the case of the thin-leading-edge parawing, drops to about 0.1 at the higher lift coefficients. A zero value of the factor would, of course, indicate no control effectiveness.

In the plot on the right of figure 51-17, the roll-control forces experienced with the wing-bank control are compared with those for a wing-tip control which may be considered equivalent to an aileron control on a conventional wing. Two values of z/b are shown for the wing-bank control, the value of 0.50 corresponding to that used on the Gemini parawing recovery system and the value of 0.135 being a value used on one research configuration. The point to be made from this plot is that for a given rolling moment, the control forces with a wing-bank control system will be considerably higher than those with an aileron-like wing-tip control. Here again, it appears that a powered system is required to operate the wing-bank control on a Gemini-sized parawing.

A photograph of a parawing research vehicle built and flown at the NASA Flight Research Center at Edwards, Calif., is shown in figure 51-18. The vehicle is towed to altitude by an airplane and then cut loose to glide back to earth while performing various studies of parawing flight characteristics. Control is achieved
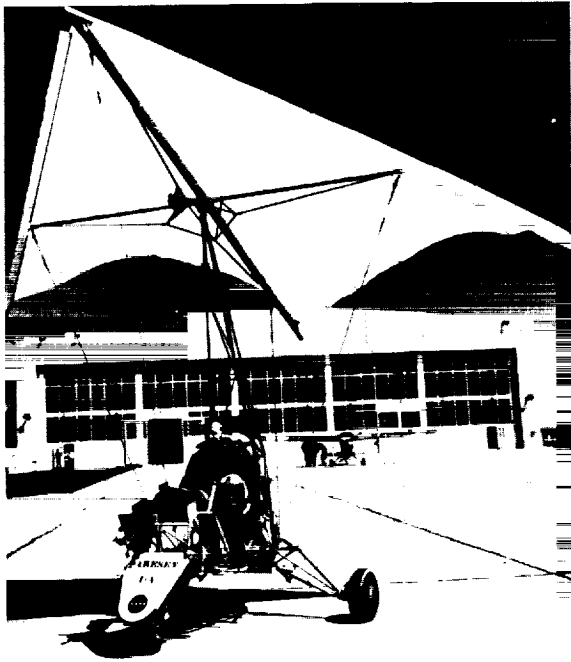
FIGURE 51-18.—NASA parawing research vehicle.

by tilting the wing with respect to the fuselage hanging underneath. Although some stability and control problems have been encountered in these tests, the results have been generally encouraging and have proved the feasibility of performing satisfactory flared landings with a parawing. Checkout flights will be made in the vehicle by some of our astronauts in the near future to provide some preliminary experience with a parawing vehicle having some of the same flight charactertistics as the Gemini recovery system.
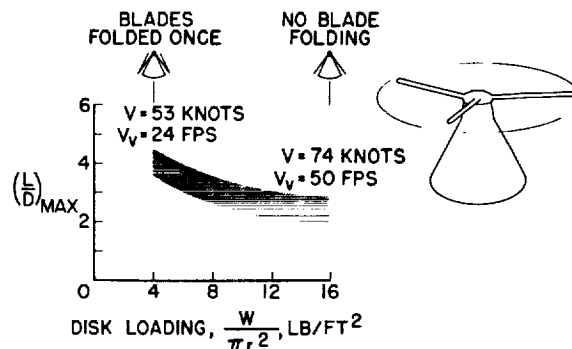
Rotor Recovery System

Figure 51-19 presents some information on a rotor recovery device, sometimes called a rotorchute. In this scheme, the rotor blades are stowed in some manner during reentry and are then extended for landing. The attractiveness of the rotorchute lies in its capability for both gliding and vertical flight with the ability to perform flared landings with essentially zero vertical and horizontal ground speed. Figure 51-19 shows calculated values of $(L/D)_{MAX}$ for a spacecraft-rotorchute recovery system having a gross weight of 8,000 pounds with disk loadings varying from about 4 to 16 lb/ft². For the disk loading of 16 lb/ft², the blades would not need to be folded except at the root; whereas for the disk loading of 4 lb/ft², a fold in the middle of the blades would also be required. The values of $(L/D)_{MAX}$ increase from about 2 to 4 as the disk loading is reduced. Experience to date with power-off helicopter landings indicates that flared landings of rotorchutes with a disk loading of 4 lb/ft² could be made fairly easily, but with a disk loading of 16 lb/ft² they would be extremely difficult to perform unless some automatic features were incorporated.

CONCLUDING REMARKS

Perhaps the principal significance of the information presented in the paper is that when a parachute is replaced by a glide-landing reentry vehicle or a glide-landing recovery device in order to give the astronaut greater latitude in the choice of a landing site, additional problems in low-speed aerodynamics are introduced, and careful attention must be given to the solution of these problems to insure a safe landing at the end of each space mission.

FIGURE 51-19.—Rotor recovery device. W=8,000 lb.

REFERENCES

1. ANON.: Results of the First U.S. Manned Orbital Space Flight February 20, 1962. Manned Spacecraft Center, NASA.
2. ANON.: Results of the Second U.S. Manned Orbital Space Flight May 24, 1962. NASA SP-6, 1962.
3. WARE, GEORGE M.: Low-Subsonic-Speed Static Stability of Right-Triangular-Pyramid and Half-Cone Lifting Reentry Configurations. NASA TN D-646, 1961.
4. STAFF OF LANGLEY FLIGHT RESEARCH DIVISION (compiled by Donald C. Cheatham): A Concept of a Manned Satellite Reentry Which Is Completed With a Glide Landing. NASA TM X-226, 1959.
5. WARE, GEORGE M.: Low-Subsonic-Speed Static Longitudinal Stability and Control Characteristics of a Winged Reentry-Vehicle Configuration Having Wingtip Panels That Fold Up for High-Drag Reentry. NASA TM X-227, 1960.
6. PAULSON, JOHN W., and SHANKS, ROBERT E.: Investigation of Low-Subsonic Flight Characteristics of a Model of a Hypersonic Boost-Glide Configuration Having a 78° Delta Wing. NASA TN D-894, 1961. (Supersedes NASA TM X-201.)
7. GAMSE, BERL, and YAGGY, PAUL F.: Wind-Tunnel Tests of a Series of 18-Foot-Diameter Parachutes With Extendable Flaps. NASA TN D-1334, 1962.
8. ROGALLO, FRANCIS M.: Paraglider Recovery Systems. Presented at IAS Meeting on Man's Progress in the Conquest of Space (St. Louis, Mo.), Apr. 30-May 1-2, 1962.
9. JOHNSON, JOSEPH L., JR.: Low-Speed Wind-Tunnel Investigation To Determine the Flight Characteristics of a Model of a Parawing Utility Vehicle. NASA TN D-1255, 1962.

52. The Aerodynamics of Hypersonic Cruising and Boost Vehicles

By Mitchel H. Bertram, David E. Fetterman, Jr., and John R. Henry

MITCHEL H. BERTRAM, *Head of the Hypersonic Aerodynamics Section, Aero-Physics Division, NASA Langley Research Center, received his Bachelor of Science degree in Aeronautical Engineering in August 1946 from New York University, Bronx, New York. Bertram is an authority in the field of hypersonic aerodynamics and especially in the field of boundary-layer interaction effects and effect of nose and leading-edge blunting. He was a member of the team at the Langley Research Center which in 1947, did research in the first regularly operating hypersonic tunnel in this country and perhaps the world. This team pioneered much of the ground which today forms the foundation of United States knowledge at very high speeds. Bertram is author of many NASA publications and has served as a reviewer of numerous papers for technical publications. He has been a frequent consultant to industrial and university representatives. He is an Associate Fellow of the Institute of the Aerospace Sciences and a member of the Hypersonics Committee of the American Rocket Society.*

DAVID E. FETTERMAN, JR., *Aero-Space Engineer, Hypersonic Branch, Aero-Physics Division, NASA Langley Research Center, received his Bachelor of Science degree in aeronautical engineering from Pennsylvania State University in June 1952. Fetterman joined the Langley staff in June 1952 and has been working in the fields of aerodynamic performance—stability and control. He is author of several NASA technical reports on research which he has conducted at Langley. He is a member of the Institute of the Aerospace Sciences, Tau Beta Pi, and Sigma Tau honorary fraternities.*

JOHN R. HENRY, *Assistant Head, Internal Aerodynamics Branch, Aero-Physics Division, NASA Langley Research Center, received his Bachelor of Science degrees in mechanical and aeronautical engineering in 1942 from the University of Michigan. Henry joined the Langley staff after graduation and has specialized in the fields of internal flow, supersonic and hypersonic air-breathing propulsion, and hypersonic air inlets. He is author or co-author of 13 NASA technical reports on research which he has conducted at Langley.*

SUMMARY

The problems of efficient hypersonic flight of boost-glide and air-breathing vehicles are reviewed for the areas of aerodynamics, stability and control, heating, and air ingestion. The application of classical hyper-sonic solutions to this class of vehicles is shown although these solutions cannot always be applied without extensive modification. Particular attention is given to the problems of interference between major vehicle components and the internal flow problems of air breathers.

215

54

INTRODUCTION

In the development of an efficient hypersonic vehicle, all of the classic problems associated with lower speed aircraft must be resolved together with the additional problems imposed by the more severe environment encountered at hypervelocities.

Pictorially, figure 52–1 shows some of the aerodynamic problem areas that might be important to a given hypersonic vehicle. A review of the present technology as applied to these problems plus that of providing a machine with high lift-drag ratios is the subject of this paper. As a larger problem area, the airplane must be trimmable and the provision of stability about all three axes is desirable. Another general problem is that of predicting the aerodynamic heating to all parts of the vehicle. This problem not only includes predictions on smooth skins, leading edges, and nose, but also the effects of both production-type and temperature-induced surface roughnesses or distortions. Where surfaces intersect, the so-called "corner problem" occurs and the the effect on heating, for example, must be evaluated. Similarly, for the case of a shock which intersects parts of the airplane, flaps or fins used for control will have separate heating and viscous problems.

In a vehicle with provision for air-breathing propulsion such as the one shown here, another set of problems must be solved. The inlet, which is the main concern here, must be able to accept large quantities of air in as precompressed a form as possible. At the same time, the inlet lip and surfaces must survive the high heating rates to which they will be exposed and further compress the air for use by the propulsion system.

SYMBOLS

$\bar{c}$	wing mean aerodynamic chord, ft
$C_{D,min}$	minimum drag coefficient
C_L	lift coefficient
C_{L_α}	lift-curve slope at zero angle of attack
C_m	pitching-moment coefficient
$c_{p,w}$	specific heat of gas at wall temperature, $\dfrac{ft^2}{sec^2 - °F}$
D	drag, lb
h	heat-transfer coefficient; height
I_{sp}	specific impulse, sec
L	lift, lb
L/D	lift-drag ratio
l	length, ft
M	Mach number
M_c	Mach number at which combustion occurs
N_{St}	Stanton number
p	static pressure, psf
q	free-stream dynamic pressure, psf
R	Reynolds number
r	radius, ft
S	wing planform area, sq ft
T_w	wall temperature, °R
V	volume, cu ft
$V_{orbital}$	satellite velocity, fps
V_∞	free-stream velocity, fps
W	weight, lb
x	linear distance from nose apex or leading edge for two-dimensional wings
y	spanwise distance measured from corner
α	angle of attack, deg
δ	control deflection angle, deg
ϵ	emissivity
Λ	leading-edge sweep angle, deg
φ	angle of ray through wing vertex measured from center line, deg
ρ_o	density of gas at sea level, slugs/ft³

Subscripts:

Body	body length
c	wing root chord; capture
f	tip flap
inf	value for infinite cylinder
j	jet exit
max	maximum
n	nose
∞	free stream
t	throat
i	inviscid
w	wall

SHOCK INTERSECTION
CORNER HEATING
SURFACE ROUGHNESS
CONTROLS
INLET
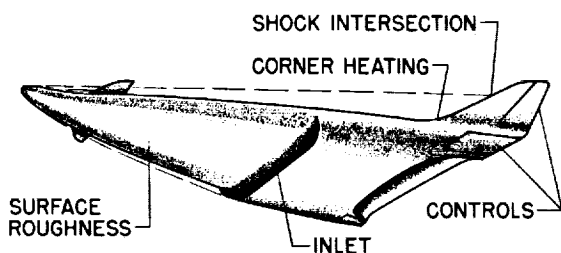
- TRIM AND STABILITY
- AERODYNAMIC HEATING

FIGURE 52–1.—Aerodynamic problem areas.

FIGURE 52–2.—Glider environment.

$$r = \frac{3.05 \times 10^3}{\epsilon^2 \rho_o \left(\dfrac{V_{orbital}}{1000}\right)^6} \frac{\left[\left(\dfrac{V_\infty}{1000}\right)^2 - \dfrac{2c_{p,w}}{1000}\dfrac{T_w}{1000}\right]^2}{(T_w/1000)^8} q \quad (1)$$

and for the earth atmosphere specifically

$$r = \frac{0.00436}{\epsilon^2} \frac{\left[\left(\dfrac{V_\infty}{1000}\right)^2 - 12\dfrac{T_w}{1000}\right]^2}{(T_w/1000)^8} q \quad (2)$$

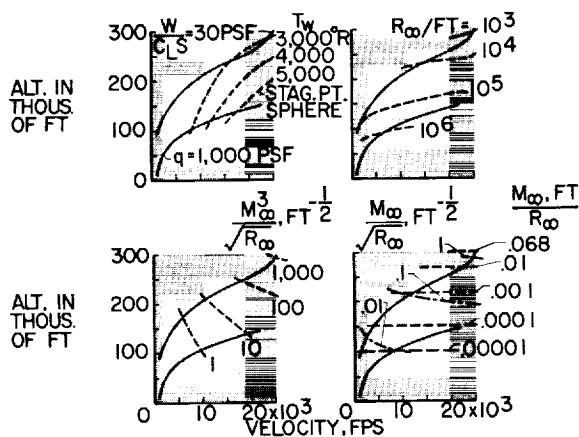## VEHICLE OPERATING ENVIRONMENT

At this point, it is instructive to examine the environment in which the hypothetical vehicle will be functioning. In figure 52–2 the solid lines outline the velocity-altitude corridor in which the vehicle must fly. The lower line represents a limitation imposed by the maximum load that the structure will support and the upper line indicates an altitude above which aerodynamic lift fails to support the airplane weight. The lower limit may be somewhat pessimistic but the upper limit is believed to be overly optimistic. For the purposes of this paper, they suffice.

The upper left-hand corner of figure 52–2 illustrates how aerodynamic heating can further limit the extent of the flight corridor. Assume that the nose of the vehicle is a sphere of radius 1 foot. If this sphere is radiation cooled, the temperature limitations of the material composing the sphere determine the path which the vehicle must follow so that the sphere remains intact.

The radius of a sphere required to maintain a given radiation equilibrium temperature at arbitrary dynamic pressures may be obtained by equating the classic equations for radiative heat transfer to those for aerodynamic heating. In this case Lees' approximate equation for the aerodynamic heating at the stagnation point of a sphere was used. (See ref. 1.) The result for planetary atmosphere, in general, is as follows:

By assuming various equilibrium wall temperatures that must be maintained with a surface emissivity of 0.8, the dashed lines were obtained. If the wall temperature of the spherical nose has to be as low as 3000° R, the maximum velocity is limited to about 15,000 feet per second. If a higher performance material is assumed, a neck opens in the corridor, although the allowable range of flight altitudes is limited. This condition occurs in the neighborhood of a Mach number of 20. If through advances in material technology the wall temperature of the spherical nose could be allowed to rise to 5000° R, a much lower altitude trajectory can be followed by the glider.

The other curves in figure 52–2 which intersect the flight corridor are concerned mainly with viscous effects. In the upper right-hand corner are shown curves along which various unit Reynolds numbers would be obtained. If vehicles with lengths on the order of 100 feet are of the proper size to be considered, when the numbers shown here are multiplied by 100 it is indicated that extensive regions of turbulent flow will probably occur on the vehicle over much of the corridor.

In the lower left-hand corner are shown curves for various values of the hypersonic interaction parameters $M_\infty^3/\sqrt{R}$ at a length of 1 foot. This parameter determines the importance of effects induced by thick hypersonic laminar boundary layers. These are the boundary-layer "displacement" or "self-induced" effects. (See refs. 2 and 3.) The larger the value of $M_\infty^3/\sqrt{R}$ the more important are the self-induced effects. It is clear that viscous effects involving thick boundary layers can be important in the same region that heating is critical, that is, in the region of a Mach number of 20.

217

The lower right-hand section of figure 52–2 contains parameters which are a form of the Knudsen number and indicate the regime of flow as outlined by Tsien. (See ref. 4.) The values of these parameters indicate that the main interest lies in the continuum flow region within the flight regime. It is only at the extreme altitudes that low-density effects might be significant. The more recent work of Probstein (ref. 5) on the delineation of the flow regimes for blunt bodies also gives this result.

PERFORMANCE AND STABILITY

Effect of Vehicle Shape on Lift-Drag Ratio

The importance of high lift-drag ratios for low to moderate hypersonic speeds has long been recognized. (See ref. 6.) The vehicle shapes that constitute the best approaches to obtaining high lift-drag ratios are still prime food for controversy. As shown in figure 52–3, three main vehicle types have been considered—the flat top or body suspended below wing, the flat bottom or body mounted above wing, and the intermediate shape which has the body symmetrically arranged on the wing. The principle of the flat-top type which utilizes favorable interference was independently suggested by several investigators. (See refs. 7 to 10.) This wing-body arrangement in its various forms utilizes upwash and pressure lift on the wing due to the body to obtain increased aerodynamic efficiency. Because of the behavior of the body pressure field with flight speed, optimum aerodynamic efficiency for these

FIGURE 52–3.—Configuration comparison on basis of aerodynamic efficiency. $M_\infty = 3$ to 10.

configuration types is Mach number limited. The flat-bottom type was proposed mainly as a means to put the body into a more shielded region and thus decrease the heating load on the configuration.

Linearized theory indicates the maximum lift-drag ratio of symmetrical wings is a function of the lift-curve slope divided by the minimum drag coefficients. Data for $(L/D)_{max}$ obtained by Clarence A. Syvertson, Hermilo R. Gloria, and Michael F. Sarabia at the Ames Research Center and William O. Armstrong and Charles L. Ladson at the Langley Research Center on the various random configuration types over a range of Mach and Reynolds numbers are shown as a function of $C_{L_\alpha}/C_{D,min}$ in figure 52–3. The solid line represents the prediction of linearized theory and the data arrange themselves about this line. In general, at the higher values of L/D the flat-top types have the highest maximum lift-drag ratios; the flat bottom, the lowest; and the symmetrical types, intermediate values. At the lower values of L/D, for example, about 4, the differences in L/D between the various shapes tends to disappear on this plot.

If a constant value of $(L/D)_{max}$ is examined, for example 5, a large range of the parameter $C_{L_\alpha}/C_{D,min}$ is covered. What this means, however, in terms of available volume and the accompanying wing area which affects the structural efficiency remains to be determined. In figure 52–4 the details of the vehicle configurations which generated this particular value of $(L/D)_{max}$ are shown. The lift-drag ratios of these configurations are shown in figure 52–5 as a function of the much used volumetric efficiency parameter, that is, volume to the $\frac{2}{3}$ power divided by the vehicle planform area. Note that the vehicle on the far right has a planform area less than 30 percent of that of the configuration on the far left even though the bodies of the two configurations are identical. Some penalty, however, accrues to the lift coefficient as the volumetric efficiency is increased as shown at the top of this figure. In proceeding from the lowest volumetric efficiency configuration to the highest, there is a loss of about 30 percent in lift coefficient.
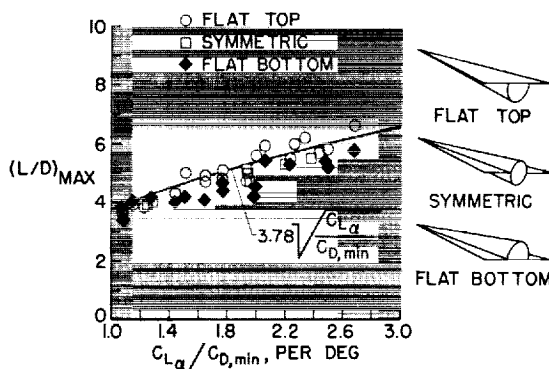
218

CONF. 1 CONF. 2 CONF. 3 CONF. 4
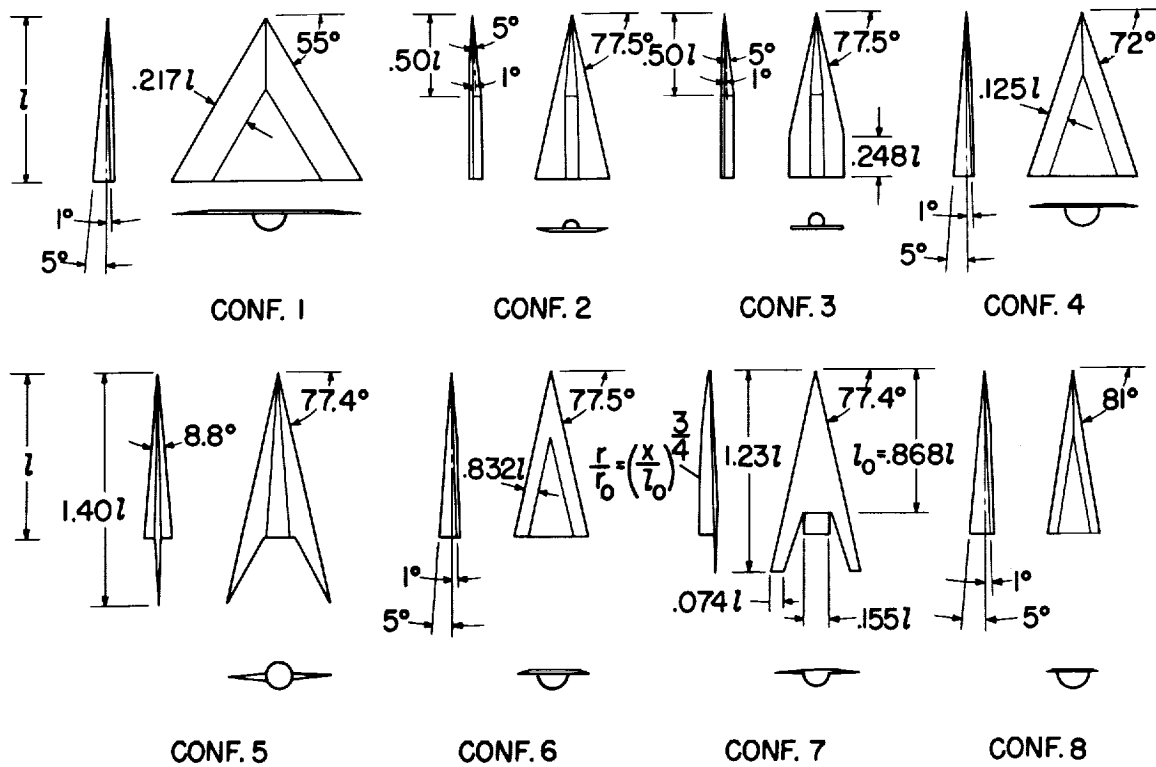
CONF. 5 CONF. 6 CONF. 7 CONF. 8

FIGURE 52–4.—Details of configurations used in aerodynamic efficiency study.

These data are for essentially constant body length. If results for other constraints such as constant volume or constant planform area were to be evaluated, the Reynolds numbers would have to be adjusted accordingly. Table 52–I gives volume, planform area, and length under the various geometric constraints as a ratio to its value for configuration 1. Note that, when the configurations are adjusted to constant body

FIGURE 52–5.—Volumetric efficiency variation at a given $(L/D)_{max}$.

volume, the body length does not vary greatly over this range of configurations.

It should be noted that any inference from figure 52–5 that $(L/D)_{max}$ is relatively independent of volume should be avoided. Actually, data not included herein indicate that for a given wing planform and wing-body orientation, an increase in volume can significantly lower the $(L/D)_{max}$ capability of a configuration. The data of figure 52–5, however, indicate that this result is not necessarily true when a variety of configurations are considered so that apparently a great deal more flexibility in configuration design is available to the aerodynamicist than was previously realized.

In the comparison, a wide range of volumetric efficiencies is covered by a number of miscellaneous shapes. Of course, one problem is to provide the volume distribution in such a way as to allow a proper weight distribution. For these purposes, a cone is poor. The second configuration from the right, where the body is a ¾ power shape, is an improvement over a cone in regard to volume distribution. This
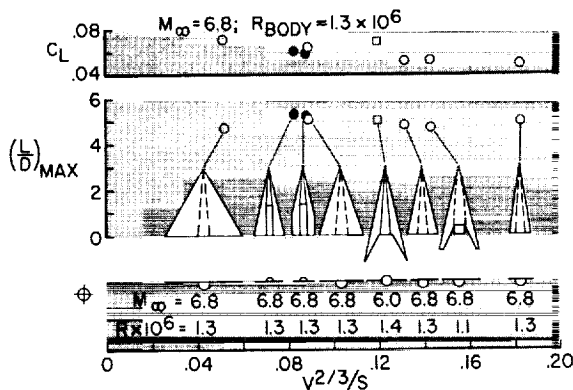
TABLE 52–I.—*Geometric Properties of Configurations With Various Constraints*

Configuration	$\dfrac{V^{2/3}}{S}$	Constant body length		Constant body volume		Constant planform area	
		V/V_1	S/S_1	l/l_1	S/S_1	l/l_1	V/V_1
1	0.052	1	1	1	1	1	1
2	.083	.50	.38	1.26	.61	1.62	2.11
3	.088	.50	.36	1.26	.57	1.67	2.33
4	.089	1	.56	1	.56	1.33	2.37
5	.120	1.24	.49	.93	.42	1.43	3.64
6	.132	1	.38	1	.38	1.61	4.22
7	.143	1.97	.55	.80	.35	1.35	4.80
8	.183	1	.28	1	.28	1.91	6.93

configuration type will now be examined further.

The body for this configuration was arranged on a fixed wing in three different ways: (1) with the body suspended below the wing as presented previously, (2) with the body above the wing, and (3) with the same volume distribution but with a circular cross section arranged symmetrically on the wing. Experimental results for these configurations are shown in figure 52–6. At Mach number 6.8, the flat-top and the midbody arrangements have about the same value of $(L/D)_{max}$ and are clearly superior in this respect to the flat-bottom arrangement. At Mach number 9.6, however, the value of $(L/D)_{max}$ is decreased and the flat-top and flat-bottom arrangements appear about equal, some superiority being exhibited for the midbody arrangement.

Based on the reasoning in terms of momentum considerations on which the flat-top development is based, this result might not be

expected since it indicates a high efficiency for the midbody. Actually, these results indicate inadequacies in the knowledge of predicting optimum aerodynamically efficient configurations with volumetric and linear-dimension constraints and the penalties incurred by operation at off-design conditions. Much additional work must be accomplished on a larger and more complex variety of configurations before sufficient information is in hand to allow competent preliminary designs of practical configurations. For instance, the merged-wing—body design appears theoretically promising but essentially no experimental information on this type is now available. Unfortunately, because of the com-
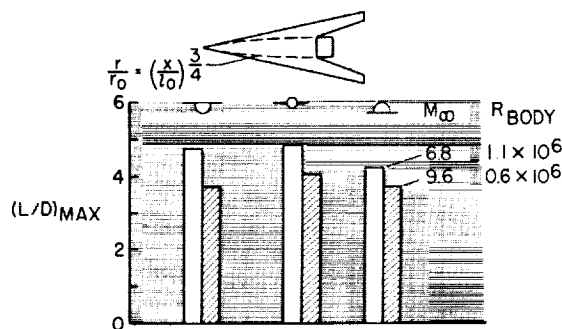

FIGURE 52–6.—Effect of wing location on $(L/D)_{max}$ of high-volume configuration.

FIGURE 52–7.—Jet expansion in base of configuration 7. $p_j/p_\infty = 467$; $M_\infty = 6.8$; $R_{Body} = 4 \times 10^5$.

plex interfering flow fields that occur over even the simplest of these configurations, experimental research must be depended upon to provide the necessary information since theoretical treatment is not reliable at present.

If air inlets have to be provided, research will have to determine how this capability can be provided with minimum aerodynamic penalty. One of the problems of integrating propulsion and airframe is shown in figure 52-7. A schlieren photograph of tests at a Mach number of 6.8 illustrates the potential interference between the jet exhaust field and the aft portion of a wing when the jet is highly expanded as at high altitudes. The jet boundary also induces a separated-flow region over the aft portion of the fuselage which could also significantly affect vehicle stability.

Effect of Trim and Directional Stability on $(L/D)_{max}$

It should be noted that the foregoing data were primarily obtained on simple wing-body combinations with no provisions for nose or leading-edge blunting, longitudinal trim, or directional stability. In general, these complications will tend to reduce $(L/D)_{max}$ values below those previously shown; however, some information is available which indicates that trim penalties need not be excessive. These results were obtained at a Mach number of about 6.8 and are shown in figure 52-8. On the left of the figure the pitching-moment and the lift-drag ratio characteristics for the ¾ power body configuration, previously discussed, are shown for a representative center-of-gravity position at 46-percent mean aerodynamic chord. Data are presented for both the flat-top and flat-bottom versions of this configuration. The data indicate that the flat-top configuration trims $(C_m=0)$ near $(L/D)_{max}$ with no longitudinal control deflection necessary; thus, the trim penalty on $(L/D)_{max}$ for this configuration is essentially zero. On the other hand, the data for the flat-bottom version of the same configuration produces the negative pitching moments (characteristic of flat-bottom types) which must be overcome for trim with a negative control deflection if conventional trailing-edge controls are employed. Since negative control deflection
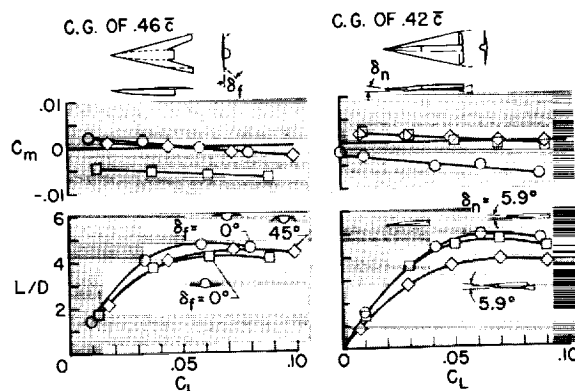

FIGURE 52-8.—Effect of trim and directional stability on $(L/D)_{max}$. $M_\infty = 6.8$.

implies primarily a loss in lift, it also implies a decrease in $(L/D)_{max}$ at trim for the flat-bottom types. However, a significant loss in L/D is not necessary; this fact is indicated by the data obtained by Robert W. Rainey at the Langley Research Center for the flat-bottom configuration shown at the right on figure 52-8. On this model, provisions were made for deflection of the forward portion of the nose. With the nose portion undeflected, the characteristic negative pitching-moment variation with lift coefficient results. With the nose portion deflected to give positive lift, however, the altered pitching-moment characteristics are similar to those of the flat-top configuration (on the left of fig. 52-8) so that trim is now obtained with only a slight reduction in $(L/D)_{max}$. Trailing-edge controls were also included on this configuration but, since the control area was insufficient to provide trim at $(L/D)_{max}$, these results have not been included. The trends of the data, however, indicated that, with this control alone, significant trim penalties in $(L/D)_{max}$ could be expected. The effects on trimmed $(L/D)_{max}$ of providing directional stability to these configurations are shown by the additional data included in figure 52-8. In order to provide directional stability, the wing tips of the configuration on the left-hand side of figure 52-8 were turned down 45° and wing-tip fins were added to the configuration on the right. In both cases these modifications had small effects on the resulting pitching-moment characteristics but significantly lowered the $(L/D)_{max}$ at trim.

HEAT TRANSFER

Heat Transfer to Lower Surface of Delta Wing

In order to present a clear picture of the overall distribution of heat-transfer rates and their relation to the external flow fields, the first part of this discussion will be based on fully laminar data at $M_\infty = 9.6$ obtained by James C. Dunavant at the Langley Research Center. Consider the sharp-leading-edge delta wing; it is geometrically simple but should still indicate the general behavior of the heat transfer to a blunt wing far from the leading edge. Figure 52-9 shows the trend of heat transfer with angle of attack for points along the center line of a flat delta wing. The results are presented in the form of the laminar flat-plate correlating parameter (Stanton number times the square root of Reynolds number based on distance from the nose) with fluid properties evaluated at free-stream conditions.

Up to an angle of attack of about 20°, the heat transfer increases with angle of attack about as expected for a flat plate, as shown by the solid curve in figure 52-9 labeled "strip theory." At higher angles of attack, the data depart from the strip theory trend and approach the dashed curve predicted by crossflow theory, which regards the wing as a succession of independent spanwise strips in two-dimensional crossflow. The crossflow approach neglects effects of the chordwise component of the flow. A more refined and more nearly correct approach is given by the streamwise divergence
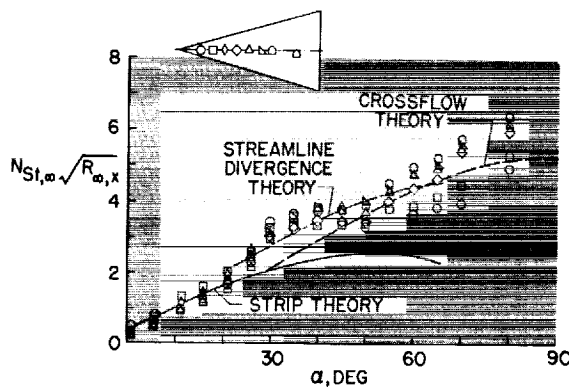
theory shown by the dot-dashed line which fits the data well. (See ref. 11.) Above an angle of attack of about 60°, the wing shock is curved and the correlation based on a single characteristic length, the distance from the nose, can be expected to break down.

The effect of turbulent flow is a larger unknown than that of laminar flow previously considered. As noted earlier, over a large part of the flight corridor the Reynolds numbers are high enough that considerable regions of turbulent flow might be anticipated on the vehicle. Heat-transfer data have been obtained by James C. Dunavant of the Langley Research Center over a wide range of Reynolds number on the same delta wing on which the results shown in figure 52-9 were obtained. These data however were taken at a Mach number of 6.8 and an angle of attack of 16°. In figure 52-10 only data on the center line of the flat delta wing are shown. The data were obtained at a stagnation temperature of about 650° F and a skin temperature of about 100° F.

The data are laminar up to a Reynolds number of about 400,000 as indicated by a comparison with laminar theory (Monaghan T' method, ref. 12). The flow is then transitional to a Reynolds number of about 10^6 and appears to be fully turbulent above this value of Reynolds number. The data of the highest Reynolds numbers show good agreement with the turbulent theory (Van Driest, ref. 13) even though the turbulent theory assumes turbulent flow from the leading edge.

FIGURE 52-9.—Heat transfer to the center line of a delta wing over angle-of-attack range from 0° to 90°. $\Lambda = 75°$; $M_\infty = 9.6$.

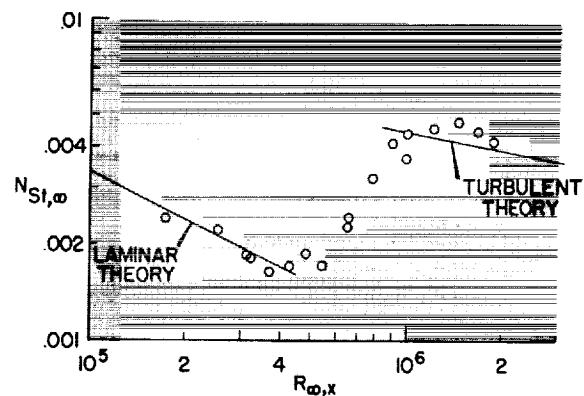FIGURE 51-10.—Heat transfer on center line of delta wing. Sharp leading edge; $\Lambda = 75°$; $M_\infty = 6.8$; $\alpha = 16°$.

The surface flow patterns obtained by James C. Dunavant corresponding to the heat-transfer data are shown in figure 52-11. These are tracings of oil-flow streak patterns formed by flowing lubricating oil impregnated with carbon black at a Mach number of 9.6. The patterns are shown in 15° increments from 0° to 60°. At the far left on figure 52-11 the pattern for zero angle of attack is shown. Here the surface flow is directed toward the center line of the wing because of the pressure gradient induced by the thick laminar boundary layer. This case was considered in some detail in reference 14 and additional information is given in a following section. With increasing angle of attack as shock loss effects start to predominate, the flow at the surface turns out from the center as shown in the three figures to the right. At an angle of attack of 15° the flow is away from the wing center line but still comes in across the leading edge. At an angle of attack of 30° the flow has turned out to such an extent that in the sense of the airflow direction the geometric leading edge has become a trailing edge. An interesting feature of the flow at an angle of attack of 30° is the appearance of a parting line at about 12° from the center line of the wing. At an angle of attack of 45° the flow is very close to radial in the center region of the wing and above this angle of attack the parting line is not a feature of the surface flow lines. At an angle of attack of 60° the flow lines which for the most part were more or less straight at lower angles of attack appear to be hyperbolic in nature. It may be seen that the patterns show conical symmetry at angles of attack of 30° and greater.
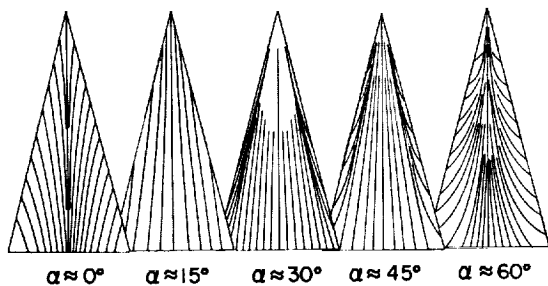

FIGURE 52-11.—Lower-surface flow patterns on flat delta wings. $\Lambda = 75°$; $M_\infty = 9.6$.

Much of the problem of predicting the heat transfer to a delta wing over a wide range of angle of attack is the changing flow pattern with angle of attack. Simple approaches to predicting the heat transfer will only be successful if the flow pattern peculiar to the angle-of-attack range under consideration is taken into account. For high L/D vehicles, it is the low angle-of-attack range that is generally of interest.

At low Reynolds numbers and high Mach numbers thick laminar boundary layers may have large effects on local pressure, skin friction, and aerodynamic heating. How these boundary-layer self-induced effects affect the chord force on a delta-wing configuration was shown in figure 5 of reference 15. The configuration analyzed was actually configuration 4 of the present paper (see fig. 52-4) tested at a Mach number of 9.6. Some additional information is now available on the local pressure and heat transfer to a delta wing at an angle of attack of 0°.

Consider first the $\alpha = 0°$ flow pattern presented in figure 52-11. The boundary-layer induced-pressure gradient has caused the low-energy air in the boundary layer near the surface to flow toward the center of the wing and to pile up along the center line. However, because of this very gradient, the streamlines external to the boundary layer must be away from the center of the wing. The angle between the surface flow direction and the external streamline increases with increasing Mach number. (See ref. 14.)

Pressures and heat transfer measured on a 75° sweep delta wing at three hypersonic Mach numbers by James C. Dunavant are shown in figure 52-12. Mach number 6.8 and 9.6 data are from tests in air and the Mach number 17.8 data are from tests in helium. The pressure data shown in figure 52-12(a) show reasonable agreement with the theoretical two-dimensional boundary-layer displacement pressures. However, the result is different for the heat-transfer data shown in figure 52-12(b) which were obtained at essentially the same three Mach numbers as the pressures. The heat-transfer results, shown in terms of the laminar correlation parameter (Stanton number times the
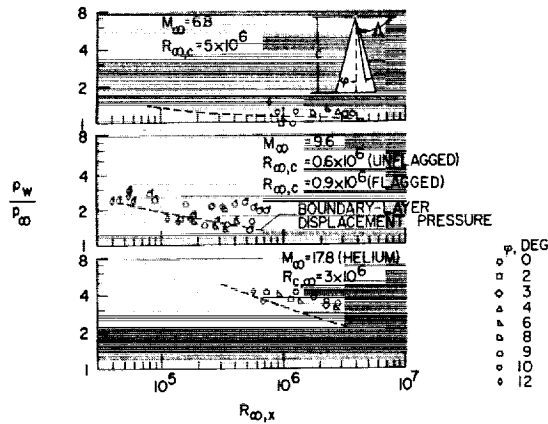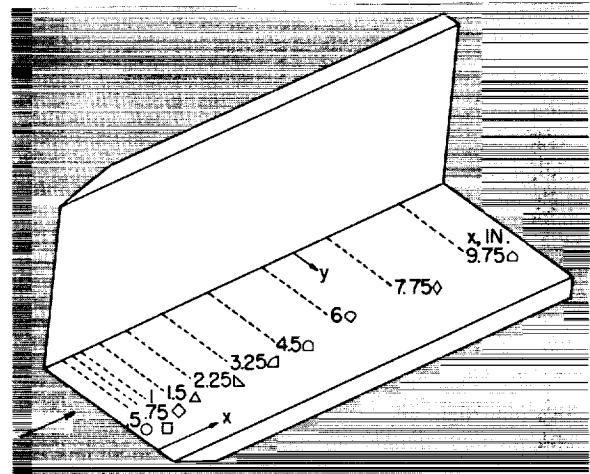
(a) Pressures.

FIGURE 52-12.—Variation of pressure and heat transfer with Mach number. $\Lambda=75°$; flat sharp-edge delta wing; $\alpha\approx0°$.

square root of Reynolds number based on tunnel test-section static conditions), are plotted against Reynolds number based on streamwise distance from the leading edge. At a Mach number of 6.6, the data in general group around the theory but the data in the region of the wing near the center line tend to lie below the theory (ref. 16). At Mach numbers of 9.6 and 17.8, the heat transfer is increased above the value from constant-pressure strip theory for the points nearest the leading edge. This increase is due to boundary-layer induced pressures. There is, however, a dropoff in the value of the heat-transfer parameter with distance from the leading edge, and at the farthest

(b) Heat transfer.

FIGURE 52-12.—Concluded.

distances from the leading edge there is a large discrepancy between data and theory. The deviation between theory and data increases with increasing Mach number and is attributed to the flow of low-energy air in the boundary layer toward the center line of the wing.
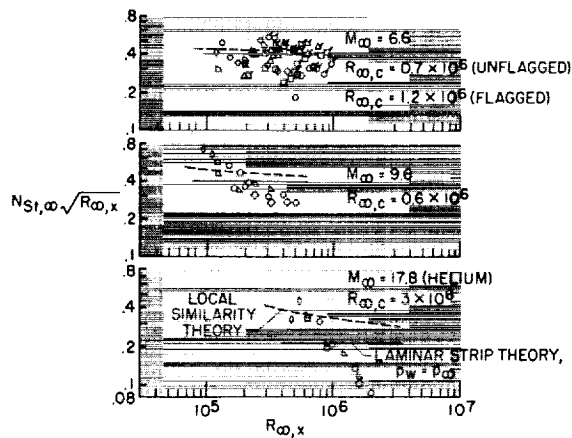
Corner Heating

As mentioned early in this paper, a corner problem exists wherever two surfaces which form part of the airplane intersect at an angle. For example, this could be the intersection of a wing with a body or a fin and could be an internal or an external corner. A knowledge of corner effects on local pressures and heating is

(a) Sketch of model.

FIGURE 52-13.—Heat transfer to a 90° corner at a Mach number of 8.

clearly necessary. Actually, not a great deal of work has been done on corner effects. Gersten in reference 17 summarizes the results obtained in incompressible flow. Stainback's results for pressure and heat transfer at a Mach number of 5 (ref. 18) are compromised by what appears to be tunnel interference. The Princeton results (ref. 19) give pressure measurements in a corner and the recent Boeing results (ref. 20) give both pressure and heat-transfer results at a Mach number of 16. Some recent heat-transfer data obtained by P. Calvin Stainback in the Langley Mach 8 variable-density tunnel on a simple 90° corner model are shown in figure 52-13. Each of the plates making up the model (fig.

52–13(a)) had a span of 4 inches and an overall length of 11 inches. The leading edges were unswept and sharp. Instrumentation extended from close to the corner to 2 inches from the corner. The symbols shown for the given values of longitudinal distance x are the coding used in figure 52–13(b).

Based on the incompressible results, the data in the form of the laminar heat-transfer correlating parameter were plotted against angular spacing from the corner as shown in figure 52–13(b) for the model surfaces alined with the flow. Data at two unit Reynolds numbers are shown, one of which is roughly 40 times the other. At the lowest unit Reynolds number the correlation on the basis of the parameters used is believed to be good. At large values of y/x where the corner does not influence the flow, the laminar flat-plate theory (ref. 12) closely predicts the level of heat transfer except for the stations closest to the leading edge. The increased heat transfer at these stations is attributed to boundary-layer displacement effects.

As the corner is approached, there is at first a general dip in the heat-transfer level. This dip occurs ahead of the free-stream location of the Mach wave from the vertical plate (vertical dashed line). Closer to the corner, there is a rapid increase in heat transfer to a peak roughly 40 percent greater than in the undisturbed flow far from the corner. Approaching the corner after the peak, there is a decrease in heat transfer as predicted by reference 21. Reference 21,
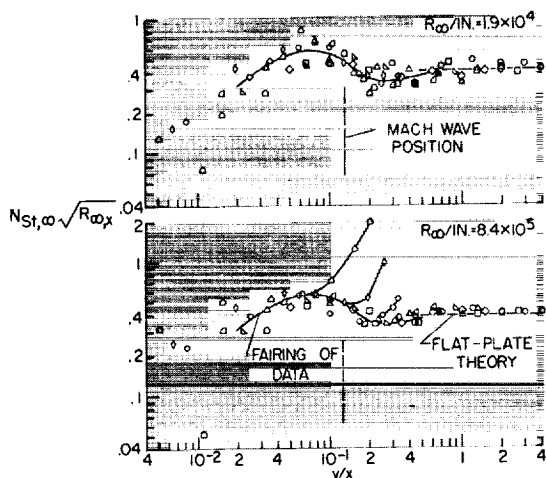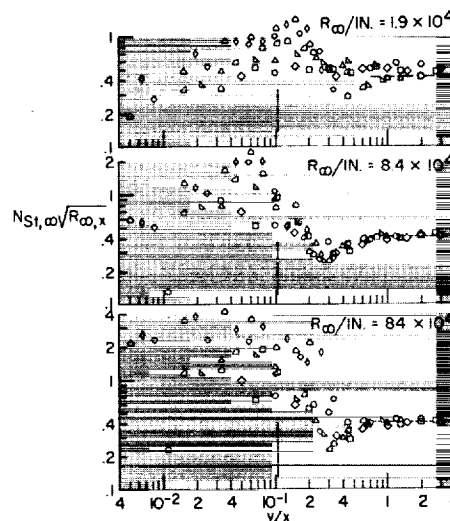

FIGURE 52–13.—(c) Model yawed 5°.

however, predicts only a uniform decrease from the flat-plate value to 0 in the corner. The general shape of the curve is similar to that obtained from local shear variations in a corner in incompressible turbulent flow. (See ref. 17.)

At the higher unit Reynolds number in figure 52–13(b), the description is much the same except that the stations farthest back on the model show evidence of transition. At the rear stations there is evidence that the turbulent flow is inhibited as the corner is approached, since the data from these stations close to the corner fair into similar data obtained at the more forward stations.

Because of the success in correlating the data with the surfaces alined with the flow, the same approach was taken with the results obtained at 5° yaw. In the yaw case, it is the vertical surface that is at an angle of attack of 5° and the horizontal instrumented surface is at an angle of attack of 0° although the leading edge has been rotated 5°. These data are shown in figure 52–13(c). The laminar flat-plate correlating parameter (Stanton number times square root of Reynolds number) is shown as a function of angular spacing from the corner. The correlation is good where the corner does not influence the flow (that is, large y/x) and laminar flat-plate theory closely predicts the level of heat transfer in this region. As the corner is approached, there is at first a general dip in the heat-transfer level. This dip occurs ahead of

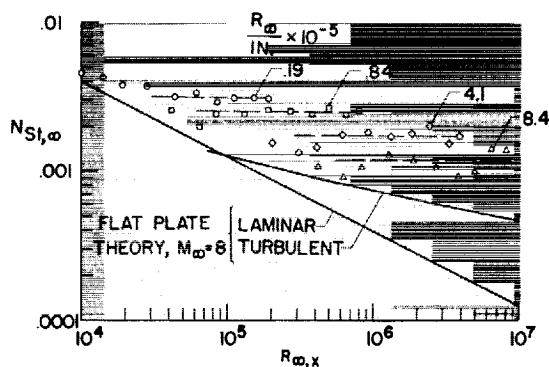FIGURE 52–13.—(b) Model alined with flow.

225

FIGURE 52-14.—Peak values of corner heating at a Mach number of 8 and with 5° yaw.

the free-stream location of the shock from the yawed plate shown by the vertical dashed line. Closer to the corner, there is a rapid increase in heat transfer to a peak generally much greater than in the undisturbed flow far from the corner.

The data in the high heating region close to the corner obviously do not correlate in the parametric form shown. The peak values of heating in the form of Stanton number alone were then taken and plotted against the Reynolds number based on distance from the leading edge at which this peak heating occurred. The data in this form are presented in figure 52-14. For reference purposes, laminar and turbulent flat-plate theory for a Mach number of 8 are included in this figure. The level of this flat-plate theory would be somewhat raised if the pressure increase behind a shock caused by a 5° deflection was taken into account.

At a given unit Reynolds number the peak heat-transfer coefficient is more or less independent of Reynolds number based on x-distance. The horizontal dashed lines are arbitrary fairings of these data at the various unit Reynolds numbers. The peak Stanton number, however, does decrease with an increase in unit Reynolds number. Thus some interesting results have been obtained but, as yet, the information is incomplete. For one thing, the peak heat-transfer coefficient is a function of a dimensional quantity. The pressure results corresponding to these heat-transfer data are not yet available and, when obtained, may aid in evaluating these results. The available infor-

mation would still be meager because practical leading edges would be blunted, probably swept, and may not meet at a 90° angle. Even less has been done on the external corner than on the interior corner. This is a problem that needs a great deal of future study.

Shock Impingement

Not much work has been done on shock-impingement effects as a separate problem although some of the results of corner investigations are probably applicable. Ivan E. Beckwith at the Langley Research Center has obtained some heat-transfer and pressure results on a rod protruding from a 8° wedge as shown in figure 52-15. The circular rod was swept back 60° from a normal to the free-stream flow direction. The measurements, when comparison is made with previous work (ref. 22), showed the flow over the rod, including the stagnation point, to be turbulent. No effect of the shock impingement can be detected in either the stagnation-line pressure or heat-transfer measurements. An appreciable increase in pressure and heat transfer can be found in the vicinity of the juncture of the rod and wedge. At least part of this increase can be attributed to the oblique shock which occurs near the base, although some boundary-layer separation may complicate the picture.

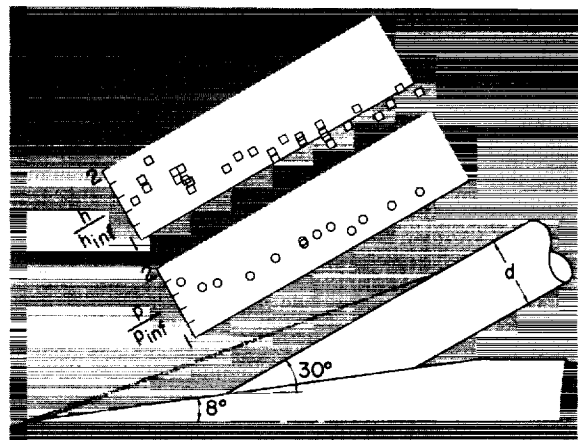It would appear that for these conditions, shock-impingement effects were not important;

FIGURE 52-15.—Effect of shock impingement on swept-cylinder stagnation-line pressures and heat transfer at $M_\infty = 4.15$ and $R_\infty d = 1.7 \times 10^5$.

however, much more work needs to be done before a definitive answer can be given. Experiments need to be made at higher Mach numbers, at various shock strengths and sweep, and for laminar and turbulent boundary layers.

Heating on Surface Distortions

In previous considerations of aerodynamic heating, the experimental data were obtained on smooth models. In the case of actual vehicles, however, the skin may be significantly irregular. Such irregularities may be the result of structures choice and the high heating rates and temperatures to which the vehicle surface is subjected. A recent experimental program at the Langley Research Center represented distortions to the surface in an idealized way. One main group of these irregularities represented a distortion as a single sine wave on a basically flat plate. Part of this work is presented in reference 23 for the laminar case; however, some turbulent data have also been obtained. These aerodynamic heating data are shown in figure 52–16 for concave and convex sine wave shapes on a flat plate with a sharp leading edge at an angle of attack of 20°. The convex shape is the mirror image of the concave shape and the length of the wave was 7½ times the depth or height of the wave. The thickness of the boundary layer just ahead of the sine wave shape was small compared with the depth or height of the wave. The data are shown in terms of the aerodynamic heating parameter

(Stanton number) as a function of Reynolds number based on distance from the leading edge. For each wave the data on the left of the figure represent results at a unit Reynolds number about one fourth that of the data on the right. The open symbols represent data obtained on a flat plate at locations the same as those for the distortion. The flat-plate data at the lower unit Reynolds number are laminar whereas those at the higher unit Reynolds number range from transitional to turbulent in nature.

With laminar flow over the concavity the flow separates a short distance after it turns to enter the concavity. The local heating drops under the separation, reaches a minimum, increases again, and reaches a peak of about 4 times the flat-plate value at about the point where reattachment occurs. For the turbulent case, the flat-plate heating is increased and the peak heating on the concavity is about 3 times the flat-plate turbulent values.

The convex sine wave shows a considerably increased peak heating. In this case for the laminar-flow results, separation due to the bump extends well ahead of the distortion and, at about the point of reattachment on the sine wave, the heat transfer peaks to a value about 17 times that on the flat plate. For the turbulent case, the peak increase in heating is only about 3½ times the flat-plate value.

These results are only part of the story because representative data would also include the case where the surface irregularity height or depth is of the same order to much thinner than the turbulent boundary layer as well as covering a large range of Mach number. Much more needs to be learned about surface irregularity effects.

Heat Transfer to Blunt Nose and Leading Edges

Up to this point no detailed consideration has been given to the blunt nose and leading edges. Actually, studies of these blunt shapes have been part of the literature for some time now and are already textbook material. Some of the sources of our knowledge of blunt-nose heat transfer will be pointed out.

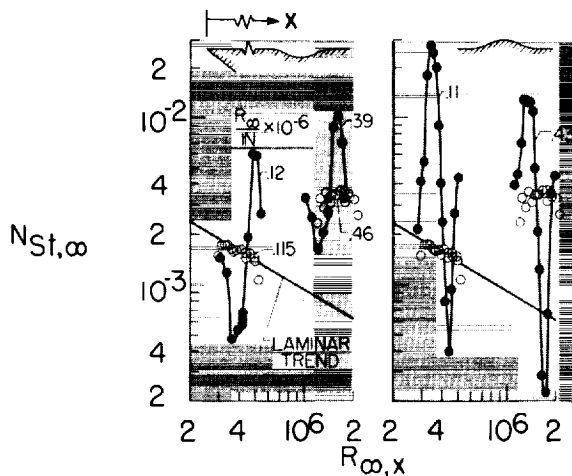Beckwith's theoretical work (ref. 24) together with experimental and further theoreti-

FIGURE 52–16.—Heating distribution on sine wave shapes. Sharp leading edge; $M_\infty = 6.8$; $a = 20°$.

227

cal work by Feller, Eggers, and Goodwin and their colleagues (refs. 25 to 27) showed the advantage of sweep in reducing the heat-transfer rates to blunt leading edges. The effect of sweep on the leading-edge heat transfer was further refined by Reshotko and Beckwith. (See ref. 28.) Lees introduced the concept of the frozen distribution of heat transfer over blunt bodies and thus simplified the problem of extrapolating the results of experiment. (See ref. 29.)

The well-known work of Fay and Riddell assessed the effects of equilibrium dissociation and gave correlation equations for the numerical results. (See ref. 30.) In later work which included the effects of transpiration cooling on the heat transfer to a yawed cylinder, Beckwith postulated that the stagnation-point heat-transfer parameter might be more dependent on the viscosity law assumed than on whether dissociation occurs. (See ref. 31.) Based on complete solutions of the boundary-layer equations for a dissociated gas in equilibrium, Cohen and Beckwith found this to be the case. (See ref. 32.)

Transition to turbulent flow on yawed cylinders has been investigated by Beckwith and Gallagher at a Mach number of 4 (See refs. 22 and 33.) They found streamline curvature to cause premature transition in many cases. The theory in reference 33 provides a means of evaluating the turbulent heat transfer on a yawed cylinder. By use of Cohen's theory (ref. 34), the heat transfer on a variety of blunt shapes with turbulent flow may be evaluated.

PROPULSION CONSIDERATIONS

As previously mentioned, air-breathing propulsion is being considered for high L/D hypersonic vehicles, primarily because of its inherent advantage of high thrust per unit fuel flow or specific impulse. This section of the paper will be devoted to a brief consideration of air-breathing engines from the aerodynamicist's point of view. Several types of engines would be required to utilize air-breathing propulsion over a wide range of flight speeds as illustrated in figure 52–17 by a bar-graph type of presentation. The total length of each bar denotes the probable applicable speed range for
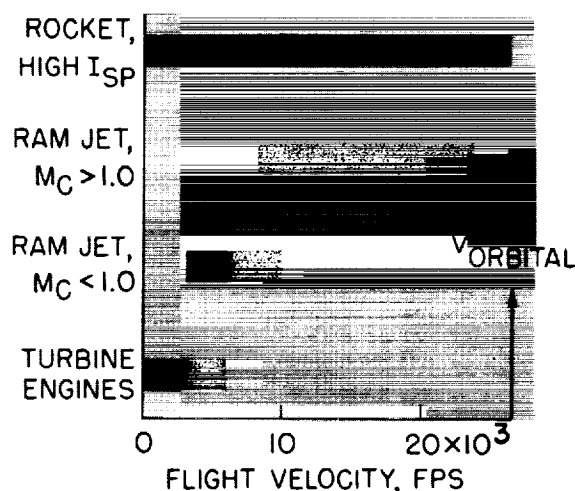

FIGURE 52–17.—Engine operating ranges.

each of the engines selected for illustration. The dark areas correspond to what may be attained with current technology, whereas the light areas would require extensions of the state of the art and extensive research in some cases. A turbojet engine could be used up to a velocity of 3,000 fps, at which point a ramjet with subsonic combustion velocities would take over and operate to some higher velocity (in the 6- to 10,000-fps range). At this point the ramjet employing supersonic combustion velocities would become effective and operate to the highest practical velocity. The high-impulse rocket is presented to indicate that it would be used to supplement air breathing in areas where air breathing proves to be marginal or not possible. In order to avoid duplication of hardware, the combination of two or more of these engines into a single unit appears to be practical. In some instances novel engine cycles are being investigated which may fulfill special mission requirements more efficiently. Extensive discussions of these considerations are given in the literature. (For example, see refs. 35 and 36.) Most of the lower speed engines which employ subsonic combustion are beyond the basic research stage; the remaining problems relate to the development of suitable hardware.

The concept of a ramjet engine which employs supersonic combustion velocities has excited a great deal of interest in the last few years since it offers the potential of operation

228

to high hypersonic speeds. (See refs. 35 and 37.) The practical realization of the concept requires the successful completion of much basic research, which is a matter of interest to universities as well as to the National Aeronautics and Space Administration. Consequently, the ramjet engine will be discussed briefly, particularly with regard to the aerodynamic aspects of the inlet.

Several features of the engine, which are directly related to supersonic combustion chamber velocities, are fundamental to its potential operation at high hypersonic speeds. The pressures and temperatures in the combustion chamber can be made low enough to bring the structural problem within reason. In addition, the combustion chamber pressures and temperatures can be maintained at levels where large amounts of dissociation of combustion products are avoided. In comparison with a subsonic combustion ramjet, the reduced amount of compression in the inlet and reduced expansion in the nozzle will result in higher performances for these components; however, these advantages will be offset somewhat by the higher entropy gains caused by combustion at supersonic velocities.

A diagrammatic cross section of the engine configuration is presented in figure 52–18 for the purpose of outlining the problem areas. If the aerodynamic design of the inlet is considered, boundary-layer growth is so rapid at high speeds that the throat of the inlet will be entirely filled with boundary layer. No research has been done on the effects of shocks on boundary layers under real-gas conditions. Leading edges will have to be blunted to avoid overheating, which will affect both the boundary-layer transition characteristics and the

Figure 52–18.—Supersonic combustion ramjet problem areas.

compression field. (See refs. 38 to 42.) The inclusion of boundary-layer bleeds or variable geometry in the design will introduce serious heating problems.

With regard to the rest of the engine, a great deal of research must be done on the combustion chamber to determine methods of obtaining proper fuel mixing with a minimum entropy gain (ref. 43) and to evaluate the combustion process in general. One of the critical problems associated with the nozzle is the requirement that the flow of exhaust products have a high degree of recombination. As mentioned previously, this problem can be controlled to a certain extent by the amount of compression in the inlet design. An overall problem of great importance is the cooling requirements for the entire engine and vehicle. Hydrogen fuel is an excellent heat sink; however, the required cooling at the high-speed end of a flight may require fuel-air ratios greater than stoichiometric and thus impair the specific impulse.

For the purpose of this paper the aerodynamic design of the inlet for a supersonic combustion ramjet was studied by computing two-dimensional point designs for several flight speeds. Table 52–II provides the input assumptions for the computations. To simplify the problem the initial shock was assumed to turn the flow 9° and all succeeding shocks 3°. The schedule of inviscid velocity reduction in the inlets was selected from studies similar to that of reference 35. The inviscid compression fields were computed by assuming a real gas and using references 44 to 48. Real-gas boundary-layer calculations were made by modifying the equations of reference 49 for laminar flow and those of reference 50 for turbulent flow. Turbulent boundary layers were assumed to have a $\frac{1}{7}$ power velocity profile. The boundary-layer parameters of reference 51 were modified to real-gas values. Inlet total-pressure recoveries and kinetic-energy efficiencies were based on a one-dimensional equivalent flow at the inlet throat obtained from conservation of mass, momentum, and energy considerations similar to those of reference 52. Real-gas properties were obtained from reference 53. Boundary-layer growth was computed along the main compression surface only. In order to deter-
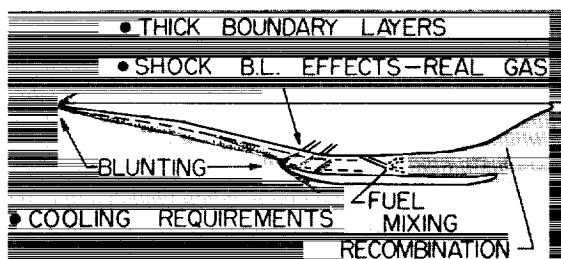
AERODYNAMICS

TABLE 52-II.—*Assumptions Used in Supersonic Combustion Ramjet Inlet Performance Calculations*

[Geometric capture height upstream of initial shock, 35 feet; turning angle of initial shock, 9°; turning through all other shocks, 3°; flow at inlet throat parallel to vehicle axis within 6° or less; and wall temperature, 2,000° F.]

Flight Mach number	Flight altitude, ft	Flight velocity, fps	Inviscid velocity reduction, fps	Total turning in compression field, deg
8	97. 0×10³	7. 98×10³	1495	48. 5
12	136. 0	12. 85	1065	30. 2
16	170. 0	17. 70	839	21. 2
20. 6	200. 0	21. 40	720	17. 0

mine a representative overall value of kinetic-energy efficiency, the sum of the losses in kinetic-energy efficiency due to the boundary-layer growth on the internal surface of the cowl and due to side-wall and corner effects was assumed to be equal to the loss in kinetic-energy efficiency computed for the boundary-layer growth along the main compression surface. The computed values of kinetic-energy efficiency were corrected for the reduction in total enthalpy produced by heat transfer through the walls on the assumption that the fuel would be used as the coolant and that the heat would be returned to the combustion chamber.

The geometric proportions computed for the inlet designs for inviscid, laminar, and turbulent flow are presented in figure 52–19. As indicated by the sketch, the geometric walls were

FIGURE 52-19.—Effect of velocity on inlet geometry.

determined by adding the boundary-layer displacement thicknesses to the inviscid-flow-field contours. For all laminar flow, figure 52-19 shows that the throat height is not significantly larger than the inviscid throat height because of the large capture height and Reynolds numbers assumed. For all turbulent flow, the throat height is considerably larger than the inviscid case on the high-speed end; in the actual case, the curve probably would fall between the laminar and turbulent results since there would have to be some length of run of laminar flow. These results clearly show the need for reliable methods for predicting the location of transition. Furthermore, the wide variation in required throat height obtained with changes in flight velocity indicates that variable geometry will be necessary unless the amount of compression is reduced at the lower speeds with some sacrifice in thrust.

Figure 52-19 also indicates that the required distance from the leading edge to the cowl lip l_c varies about 25 percent over the flight-velocity range. Although this variation would be modified by changes in the angle of attack with flight speed, fixed geometry probably will either introduce additive drag or subject the inlet to conditions where the shock enters the cowl and impinges on the boundary layer producing boundary-layer interaction effects. The most significant implication derived from the results given in figure 52-19 is that extensive trade-off analyses are required to determine the most practical designs incorporating either fixed geometry or a minimum of variable geometry.

The overall performance in terms of kinetic-energy efficiency computed by methods outlined
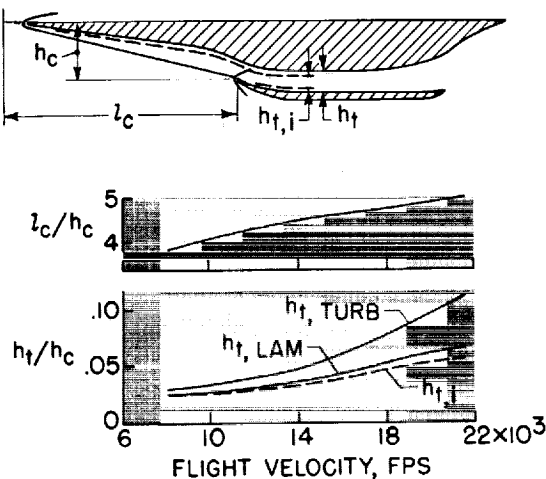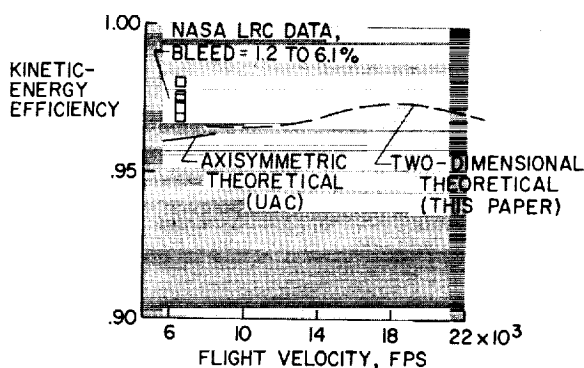
FIGURE 52-20.—Inlet efficiency.

previously is presented in figure 52-20. In order to attack significance to values of kinetic-energy efficiency, it should be realized that at speeds on the order of 20,000 fps, values of efficiency of approximately 90 percent are low enough to eliminate any thrust potential. Therefore, the efficiency must be substantially above the 90-percent level to obtain efficient operation. Figure 52-20 shows that the general level of efficiency obtained in the analysis of this paper is about 97 percent; the shape of the curve faired through the computed points has little significance because of the somewhat arbitrary assumptions of values for the flight trajectory and the amount of compression in the inlets. Theoretical performances for an axisymmetric inlet design computed by McLafferty and presented in reference 54 agree in general magnitude with the results of this paper. The experimental data points given in figure 52-20 represent wind-tunnel data for a two-dimensional inlet taken at a Mach number of 6.8 for several different arrangements of boundary-layer bleed and for several bleed quantities. The favorable effect of the boundary-layer bleed on the performance is believed to be the reason for the experimental efficiencies being higher than the theoretical curves.

From the preceding discussion one can deduce that a 1-percent increase in kinetic-energy efficiency would produce significant increases in thrust, particularly at high hypersonic speeds. Therefore, effort should be directed toward increasing the level of kinetic-energy efficiency by developing more efficient compression-field designs and by reducing viscous effects to a minimum.

CONCLUDING REMARKS

A great deal of information exists that is applicable to the high lift-drag ratio vehicle. However, much of this information is somewhat preliminary and is of the type that suggests further investigation rather than being directly usable. This discussion attempted to point out the many avenues of research which have to be more thoroughly explored before a better grasp of the total problem is in hand. Although this work will necessarily rely heavily on an experimental approach, because of the complexities involved, the theoretical aspects of the problem should also be pursued with equal vigor. Fortunately, much of this experimental work can be done at present in the conventional relatively cold facilities which have been available for some time; however, evaluation of the effects of a hypervelocity environment will eventually have to be made.

REFERENCES

1. LEES, LESTER: Recovery Dynamics—Heat Transfer at Hypersonic Speeds in a Planetary Atmosphere. Space Technology, ch. 12, Howard Seifert, ed., John Wiley & Sons, Inc., 1959, pp. 12-01—12-20.
2. LEES, LESTER, and PROBSTEIN, RONALD F.: Hypersonic Viscous Flow Over a Flat Plate. Rep. No. 195 (Contract AF 33(038)-250), Aero. Eng. Lab., Princeon Univ., Apr. 20, 1952.
3. BERTRAM, MITCHEL H.: Boundary-Layer Displacement Effects in Air at Mach Numbers of 6.8 and 9.6. NASA TR R-22, 1959. (Supersedes NACA TN 4133.)
4. TSIEN, HSUE-SHEN: Superaerodynamics, Mechanics of Rarefied Gases. Jour. Aero. Sci., vol. 13, no. 12, Dec. 1946, pp. 653-664.
5. PROBSTEIN, RONALD F.: Shock Wave and Flow Field Development in Hypersonic Re-Entry. ARS Jour., vol. 31, no. 2, Feb. 1961, pp. 185-194.

6. EGGERS, ALFRED J., JR., ALLEN, H. JULIAN, and NEICE, STANFORD E.: A Comparative Analysis of the Performance of Long-Range Hypervelocity Vehicles. NACA Rep. 1382, 1958. (Supersedes NACA TN 4046.)

7. FERRI, ANTONIO, CLARKE, JOSEPH H., and CASACCIO, ANTHONY: Drag Reduction in Lifting Systems by Advantageous Use of Interference. PIBAL Rep. 272 (Contract No. AF 18(600)–694), Polytechnic Institute of Brooklyn, May 1955.

8. EGGERS, A. J., JR., and SYVERTSON, CLARENCE A.: Aircraft Configurations Developing High Lift-Drag Ratios at High Supersonic Speeds. NACA RM A55L05, 1956.

9. ROSSOW, VERNON J.: A Theoretical Study of the Lifting Efficiency at Supersonic Speeds of Wings Utilizing Indirect Lift Induced by Vertical Surfaces. NACA RM A55L08, 1956.

10. EGGERS, A. J., JR.: Some Considerations of Aircraft Configurations Suitable for Long-Range Hypersonic Flight. Presented to Syposium on Hypersonic Flow (Univ. of Bristol, England), Apr. 6, 1959. (Sponsored by Colston Res. Soc.)

11. VAGLIO-LAURIN, ROBERTO: Laminar Heat Transfer on Blunt-Nosed Bodies in Three-Dimensional Hypersonic Flow. WADC Tech. Note 58–147, ASTIA Doc. No. AD 155 588, U.S. Air Force, May 1958.

12. MONAGHAN, R. J.: On the Behavior of Boundary Layers at Supersonic Speeds. Fifth International Aeronautical Conference (Los Angles, Calif., June 20–23, 1955), Inst. Aero. Sci., Inc., 1955, pp. 277–315.

13. VAN DRIEST, E. R.: The Problem of Aerodynamic Heating. Aero. Eng. Rev., vol. 15, no. 10, Oct. 1956, pp. 26–41.

14. BERTRAM, MITCHEL H., and HENDERSON, ARTHUR, JR.: Recent Hypersonic Studies of Wings and Bodies. ARS Jour., vol. 31, no. 8, Aug. 1961, pp. 1129–1139.

15. BERTRAM, MITCHEL H., and HENDERSON, ARTHUR, JR.: Effects of Boundary-Layer Displacement and Leading-Edge Bluntness on Pressure Distribution, Skin-Friction, and Heat Transfer of Bodies at Hypersonic Speeds. NACA TN 4301, 1958.

16. BERTRAM, MITCHEL H., and FELLER, WILLIAM V.: A Simple Method for Determining Heat Transfer, Skin Friction, and Boundary-Layer Thickness for Hypersonic Laminar Boundary-Layer Flows in a Pressure Gradient. NASA MEMO 5–24–59L, 1959.

17. GERSTEN, K.: Corner Interference Effects. Rep. 299, AGARD, North Atlantic Treaty Organization (Paris), Mar. 1959.

18. STAINBACK, P. CALVIN: An Experimental Investigation at a Mach Number of 4.95 of Flow in the Vicinity of a 90° Interior Corner Alined With the Free-Stream Velocity. NASA TN D–184, 1960.

19. BOGDONOFF, S. M., and VAS, T. E.: A Preliminary Investigation of the Flow in a 90° Corner at Hypersonic Speeds. Part I—Flat Plates With Thin Leading Edges at Zero Angle of Attack. D143–978–013 (ARDC TR 57–202, AD 150 023), Bell Aircraft Corp., Dec. 1957.

20. MILLER, D. S., HIJMAN, R., REDEKER, E., JANSSEN, W. C., and MULLEN, C. R.: A Study of Shock Impingements on Boundary Layers at Mach 16. Proc. 1962 Heat Transfer and Fluid Mechanics Inst. (Univ. Wash.), F. Edward Ehlers, James J. Kauzlarich, Charles A. Sleicher, Jr., and Robert E. Street, eds., Stanford Univ. Press, June 1962, pp. 255–278.

21. BLOOM, MARTIN H., and RUBIN, STANLEY: High-Speed Viscous Corner Flow. Jour. Aerospace Sci., vol. 28, no. 2, Feb. 1961, pp. 145–157.

22. BECKWITH, IVAN E., and GALLAGHER, JAMES J.: Local Heat Transfer and Recovery Temperatures on a Yawed Cylinder at a Mach Number of 4.15 and High Reynolds Numbers. NASA TR R–104, 1961. (Supersedes NASA MEMO 2–27–59L.)

23. BERTRAM, M. H., and WIGGS, M. MARGARETTE: Effect of Surface Distortions on the Heat Transfer to a Wing at Hypersonic Speeds. Paper No. 62–127, Inst. Aerospace Sci., June 1962.

24. BECKWITH, IVAN E.: Theoretical Investigation of Laminar Heat Transfer on Yawed Infinite Cylinders in Supersonic Flow and a Comparison With Experimental Data. NACA RM L55F09, 1955.

25. FELLER, WILLIAM V.: Investigation of Equilibrium Temperatures and Average Laminar Heat-Transfer Coefficients for the Front Half of Swept Circular Cylinders at a Mach Number of 6.9. NACA RM L55F08a, 1955.

26. EGGERS, A. J., JR., HANSEN, C. FREDERICK, and CUNNINGHAM, BERNARD E.: Theoretical and Experimental Investigation of the Effect of Yaw on Heat Transfer to Circular Cylinders in Hypersonic Flow. NACA RM A55E02, 1955.

27. GOODWIN, GLEN, CREAGER, MARCUS O., and WINKLER, ERNEST L.: Investigation of Local Heat-Transfer and Pressure Drag Characteristics of a Yawed Circular Cylinder at Supersonic Speeds. NACA RM A55H31, 1956.

28. RESHOTKO, ELI, and BECKWITH, IVAN E.: Compressible Laminar Boundary Layer Over a Yawed Infinite Cylinder With Heat Transfer and Arbitrary Prandtl Number. NACA Rep. 1379, 1958. (Supersedes NACA TN 3986.)

29. LEES, LESTER: Laminar Heat Transfer Over Blunt-Nosed Bodies at Hypersonic Flight Speeds. Jet Propulsion, vol. 26, no. 4, Apr. 1956, pp. 259–269, 274.

30. FAY, J. A., and RIDDELL, F. R.: Theory of Stagnation Point Heat Transfer in Dissociated Air. Jour. Aero. Sci., vol. 25, no. 2, Feb. 1958, pp. 73–85, 121.

31. BECKWITH, IVAN E.: Similar Solutions for the Compressible Boundary Layer on a Yawed Cylinder With Transpiration Cooling. NASA TR R–42, 1959. (Supersedes NACA TN 4345.)

32. COHEN, NATHANIEL B., and BECKWITH, IVAN E.: Boundary-Layer Similar Solutions for Equilibrium Dissociated Air and Application to the Calculation of Laminar Heat-Transfer Distribution on Blunt Bodies in High-Speed Flow. Presented at the Second International Heat Transfer Conference (Boulder, Colo.), Aug. 28–Sept. 1, 1961.

33. BECKWITH, IVAN E., and GALLAGHER, JAMES J.: Experimental Investigation of the Effect of Boundary-Layer Transition on the Average Heat Transfer to a Yawed Cylinder in Supersonic Flow. NACA RM L56E09, 1956.

34. COHEN, NATHANIEL B.: A Method for Computing Turbulent Heat Transfer in the Presence of a Streamwise Pressure Gradient for Bodies in High-Speed Flow. NASA MEMO 1–2–59L, 1959.

35. FERRI, ANTONIO: Possible Directions of Future Research in Air-Breathing Engines. Combustion and Propulsion Fourth AGARD Colloquium on High Mach Number Air-Breathing Engines, A. L. Jaumotte, A. H. Lefebvre, and A. M. Rothrock, eds., Pergamon Press (New York), 1961, pp. 3–15.

36. ZIPKIN, M. A., and NUCCI, L. M.: Composite Air-Breathing Systems. Combustion and Propulsion Fourth AGARD Colloquium on High Mach Number Air-Breathing Engines, A. L. Jaumotte, A. H. Lefebvre, and A. M. Rothrock, eds., Pergamon Press (New York), 1961, pp. 16–36.

37. DUGGER, GORDON L.: Comparison of Hypersonic Ramjet Engines With Subsonic and Supersonic Combustion. Combustion and Propulsion Fourth AGARD Colloquium on High Mach Number Air-Breathing Engines, A. L. Jaumotte, A. H. Lefebvre, and A. M. Rothrock, eds., Pergamon Press (New York), 1961, pp. 84–119.

38. MOECKEL, W. E.: Some Effects of Bluntness on Boundary-Layer Transition and Heat Transfer at Supersonic Speeds. NACA Rep. 1312, 1957. (Supersedes NACA TN 3653.)

39. BRINICH, PAUL F., and SANDS, NORMAN: Effect of Bluntness on Transition for a Cone and a Hollow Cylinder at Mach 3.1. NACA TN 3979, 1957.

40. BERTRAM, MITCHEL H.: Exploratory Investigation of Boundary-Layer Transition on a Hollow Cylinder at a Mach Number of 6.9. NACA Rep. 1313, 1957. (Supersedes NACA TN 3546.)

41. SEIFF, ALVIN, and WHITING, ELLIS E.: Calculation of Flow Fields From Bow-Wave Profiles for the Downstream Region of Blunt-Nosed Circular Cylinders in Axial Hypersonic Flight. NASA TN D–1147, 1961.

42. SEIFF, ALVIN, and WHITING, ELLIS E.: A Correlation Study of the Bow-Wave Profiles of Blunt Bodies. NASA TN D–1148, 1962.

43. PETERS, C. E., and WEHOFER, S.: Constant Area Mixing of Non-Isoenergetic Coaxial Compressible Streams. AEDC–TR–61–18 (Contract No. AF 40(600)–800 S/A 24(61–73)), Arnold Eng. Dev. Center, Jan. 1962.

44. MINZNER, R. A., CHAMPION, K. S. W., and POND, H. L.: The ARDC Model Atmosphere, 1959. Air Force Surveys in Geophysics No. 115 (AFCRC–TR–59–267), Air Force Cambridge Res. Center, Aug. 1959.

45. AMES RESEARCH STAFF: Equations, Tables, and Charts for Compressible Flow. NACA Rep. 1135, 1953. (Supersedes NACA TN 1428.)

233

46. HILSENRATH, JOSEPH, BECKETT, CHARLES W., ET AL.: Tables of Thermal Properties of Gases. NBS Cir. 564, U.S. Dept. Commerce, 1955.

47. ANON.: Handbook of Supersonic Aerodynamics. NAVORD Rep. 1488 (vol. 5), Bur. Ord., Aug. 1953.

48. HUBER, PAUL R.: Tables and Graphs of Normal-Shock Wave Parameters at Hypersonic Mach Numbers and Selected Altitudes. NACA TN 4352, 1958.

49. MONAGHAN, R. J.: An Approximate Solution of the Compresssible Laminar Boundary Layer on a Flat Plate. R. & M. No. 2760, British A.R.C., 1956.

50. ECKERT, E. R. G.: Engineering Relations for Heat Transfer and Friction in High-Velocity Laminar and Turbulent Boundary-Layer Flow Over Surfaces With Constant Pressure and Temperature. Trans. A.S.M.E., vol. 78, no. 6, Aug. 1956, pp. 1273–1283.

51. PERSH, JEROME, and LEE, ROLAND: Tabulation of Compressible Turbulent Boundary Layer Parameters. NAVORD Rep. 4282 (Aeroballistic Res. Rep. 337), U.S. Naval Ord. Lab. (White Oak, Md.), May 1, 1956.

52. WYATT, DE MARQUIS D.: Analysis of Errors Introduced by Several Methods of Weighting Nonuniform Duct Flows. NACA TN 3400, 1955.

53. MOECKEL, W. E., and WESTON, KENNETH C.: Composition and Thermodynamic Properties of Air in Chemical Equilibrium. NACA TN 4265, 1958.

54. McLAFFERTY, GEORGE H.: Hypersonic Inlet Studies at UAC Research Laboratories. Rep. M–2000–113, United Aircraft Corp., Dec. 1959. (Also available as Combustion and Propulsion Fourth AGARD Colloquium on High Mach Number Air-Breathing Engines, A. L. JAUMOTTE, A. H. LEFEBVRE, and A. M. ROTHROCK, eds., Pergamon Press (New York), 1961, pp. 138–155.)

53. Aerodynamic and Heating Problems of Advanced Reentry Vehicles

By Robert L. Trimpi, Frederick C. Grant, and Nathaniel B. Cohen

ROBERT L. TRIMPI *is Head of Reentry Physics Branch, Aero-Physics Division, NASA Langley Research Center. He received his Bachelor of Science degree in Mechanical Engineering in 1948 from Cornell University and his Master of Science degree in Aeronautical Engineering the following year. Mr. Trimpi, who joined the Langley staff in August 1949, has earned a national reputation as an authority on reentry heating, unsteady flow, real-gas flow, and heat conduction problems. He serves as a consultant on advanced technical problems in areas of reentry heating and unsteady flow, and he has produced many important contributions in basic flow phenomena. His theoretical investigations cover a variety of fields, and his publications include the subjects of supersonic inlet instability, hypersonic heat transfer, shock-tube attenuation, unsteady boundary layers, three-dimensional real-gas shock waves and flow fields, and transient aerodynamic heating of multilayer skins.*

FREDERICK C. GRANT, *Aero-Space Engineer, Reentry Physics Branch, Aero-Physics Division, NASA Langley Research Center, received his Bachelor of Science degree in aeronautical engineering from Massachusetts Institute of Technology in September 1947. He earned a Master of Arts degree in Physics from the College of William and Mary in August 1962. Grant joined the Langley staff in December 1947 as an aeronautical engineer and has been active in the fields of experimental and theoretical aerodynamics and flight mechanics. He is author or co-author of 16 technical publications on research he has conducted at Langley.*

NATHANIEL B. COHEN, *Assistant Head, Reentry Physics Branch, Aero-Physics Division, NASA Langley Research Center, received his Bachelor of Science degree in aeronautical engineering from the Polytechnic Institute of Brooklyn, Brooklyn, New York, in June 1950. He earned his Master of Science degree in aeronautical engineering from the University of Virginia in June 1956. Since joining Langley, he has been active in the fields of shock-tube research and boundary-layer and convective-heat-transfer theory. He developed a theory of laminar heat transfer in equilibrium air at flight velocities up to 41,000 feet per second. Working with Robert L. Trimpi, he developed a theory and carried out supporting experiments for shock-wave attenuation in a shock tube. Mr. Cohen is a member of the Institute of the Aerospace Sciences, and the American Rocket Society, and belongs to Tau Beta Pi and Sigma Xi honorary fraternities. He is author or co-author of 10 NASA technical publications on research he has conducted at Langley.*

42

SUMMARY

Reentry of manned lifting vehicles at parabolic (escape) velocity and reentry of unmanned nonlifting planetary probes at hyperbolic velocities are considered. A brief discussion is presented of the necessity of lift and lift modulation for the manned return; and the heating problems of aerodynamic and reaction controls are illustrated. Spatial and temporal convective and radiation heating distributions are predicted for a lifting spacecraft of the Apollo class.

Radiation heating will be the dominant mode for early planetary probes which, because of weight limitations, will be unmanned and will enter the atmosphere on nonlifting trajectories. The effect of vehicle shape on heating is first discussed for no-mass-loss (constant profile) vehicles. A section on reentry of high-mass-loss vehicles includes a preliminary study of the effects of (a) heat of sublimation on limiting entry velocity; (b) ratio of payload to total weight on limiting entry velocity; and (c) the size and total weight of a reentry vehicle necessary to return a specific payload to earth at a given high reentry velocity.

INTRODUCTION

Familiarity with near circular or satellite reentry is widespread as a result of the recent flights of the Mercury spacecraft. In this paper some of the aerodynamic and heating aspects of reentry from more advanced missions are discussed. The first part is concerned with parabolic reentry with emphasis on the manned lunar mission, and the second part with the unmanned reentry of high-speed planetary probes.

SYMBOLS

A	reference area
C_D	drag coefficient
C_H	total energy transfer coefficient, $H\left/\frac{1}{2} m_E V_E^2\right.$
C_L	lift coefficient
D	drag
d	vehicle diameter
G	acceleration in earth gravitational units
H	total heat absorbed by vehicle during reentry
L	lift
l	vehicle reference length
m_E	mass of vehicle at start of reentry
m_f	mass of vehicle at end of reentry
Q	heat of sublimation, Btu/lb
q	heating load per unit area, $\int \dot{q} dt$
$\dot{q}$	heating rate per unit area
$\dot{q}_{stag}$	stagnation-point heating rate per unit area
R	radius of curvature of front surface of vehicle
r_b	radius of body
s	distance along surface from axis
t	time
V	velocity
V_E	entrance velocity
$(V_E)_l$	limiting entrance velocity
W	vehicle weight, lb
w	vehicle density, lb/cu ft
y	altitude
α	angle of attack
γ_E	entrance angle
ρ	density
δ	flap-deflection angle
η	heat-transfer coefficient, $\dot{q}\left/\frac{1}{2} \rho_\infty V_\infty^3\right.$
θ_c	semicone angle
ϕ	roll angle

Subscripts:

∞	ambient conditions ahead of vehicle
MAX	maximum
l	limiting value
C	convective
ER	equilibrium radiative
NER	nonequilibrium radiative

REENTRY AT PARABOLIC VELOCITY

For the lunar mission the reentry velocity is parabolic and is about 36,500 feet per second at an altitude of 400,000 feet, which may be considered the outer edge of the atmosphere for aerodynamic effects. In this case, in contrast to that of the nonlifting Mercury spacecraft, a lifting capability is highly desirable. The use of lift can reduce the severity of certain reentry problems. In figure 53-1 is shown the effect of L/D on the reentry corridor height (ref. 1). This height, illustrated in the inset, is the difference between the vacuum perigees of the overshoot and undershoot boundaries. The
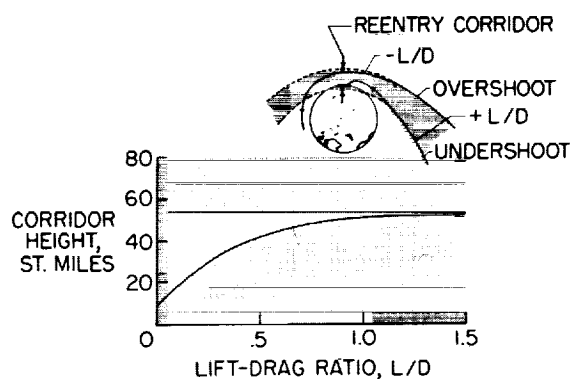

FIGURE 53-1.—Variation of reentry corridor height with lift-drag ratio.

$$V_E = 36,500 \text{ feet per second; } \frac{W}{C_D A} = 50 \text{ lb/sq ft.}$$

overshoot boundary in this case assumes a constant negative L/D during pull-up, with subsequent later modulation as required under the restriction that the trajectory never has an ascending phase; that is, $dy/dt \leqq 0$ (ref. 2). The undershoot boundary assumes constant positive L/D during pull-up with a maximum deceleration of $10G$. Note the appreciable gains in reentry corridor as L/D first increases from 0 up to approximately $\frac{1}{2}$ with diminishing gains thereafter. At $L/D=0$, the corridor is about 10 miles deep; at $L/D=\frac{1}{2}$, it has become about 40 miles deep, and at $L/D=1.5$, it has only increased to 50 miles.

The accessible landing area, or "footprint" as it is popularly called (ref. 3), increases significantly with L/D (fig. 53-2). The longitudinal range is approximately proportional to L/D and the lateral range varies roughly as L/D raised to a power between 1½ and 2. Note that the landing area for $L/D=\frac{1}{2}$ covers a major section of the continental United States.

The maximum deceleration during reentry from a given space orbit may also be significantly reduced by the application of lift. With a fixed lifting capability the air loads are reduced by using the lift force to decrease the flight-path angle continually to the horizontal and thus to lower the rate of density increase with time. If the lifting capability is variable, further peak-load reduction is possible by use of a change in attitude to reduce the resultant force. Details on this subject are given in references 4, 5, and 6.

The low lift-drag ratios that are sufficient for parabolic reentry may be obtained through
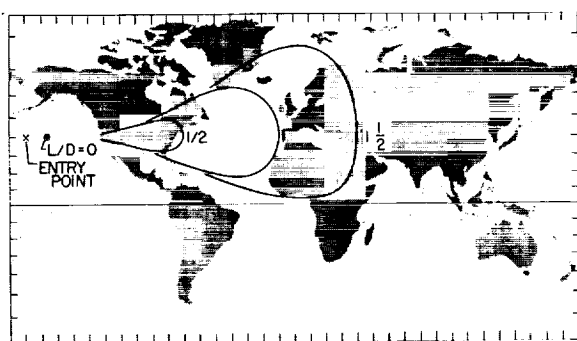

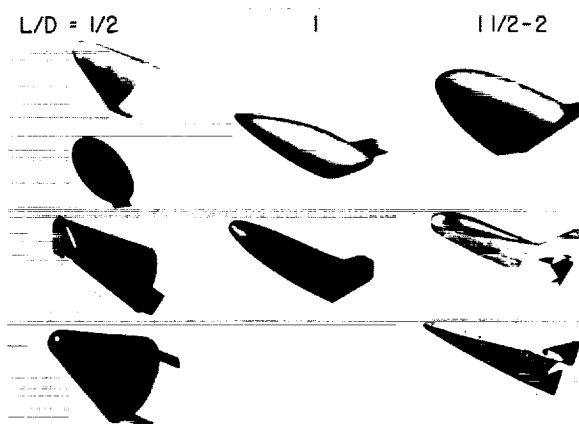FIGURE 53-2.—Variation of accessible landing area with lift-drag ratio for parabolic reentry.

FIGURE 53-3.—Hypersonic lift-drag capability of reentry shapes.

a variety of shapes (fig. 53-3). In the three columns are illustrative shapes having L/D's at high velocity of ½, 1, and 1½ to 2. The first column consists of blunt spacecraft types trimmed by internal packaging to place the center of gravity so that $L/D=\frac{1}{2}$ for the pull-up phase of reentry. The aerodynamic controls would be used for modulation after the pull-up. For these shapes the subsonic L/D is so low that auxiliary landing aids (parachutes or paragliders) are required.

Increased L/D capability is obtained, in general, by making the configuration more wing-like. The configurations with a hypersonic $L/D \approx 1$ have a subsonic L/D in the neighborhood of 4 and so are able to land horizontally without any auxiliary aids. The shapes for $L/D=1\frac{1}{2}$ to 2 appear more like conventional airplanes, and include the Dyna-Soar configuration for missions at satellite speed.

The L/D capability is very expensive in terms of vehicle weight. Configurations with higher values of L/D are not illustrated in figure 53-3, because analyses have shown that at an L/D somewhere between 1½ and 2, the weight of the ablation material required for heat protection from a parabolic reentry appears to be prohibitive. However, vehicles in this L/D range may be used for orbital missions by employing radiation-cooled surfaces.

The trade-off between L/D and weight is naturally dictated by the mission requirements. Studies are now in progress for various super-

circular missions utilizing $L/D \approx 1$ vehicles. This is the maximum L/D which appears feasible for parabolic reentry using present ablation techniques.

For the Apollo manned lunar mission which is planned for more or less ideal conditions, an $L/D \approx \frac{1}{2}$ appears sufficient in terms of corridor height, landing area, and G alleviation. Studies of such parabolic reentry vehicles have shown that although the critical heating problems are found at different parts of the vehicle for different shapes, the magnitude of the total heat load during reentry varied only moderately with vehicle shape, with the blunt spacecraft having a lower total heat load for most trajectories than the other $L/D \approx \frac{1}{2}$ shapes illustrated. However, this factor was not the deciding factor in the choice of the Apollo reentry module; several other factors, such as the structural advantages of a symmetric body, ease of integration of the reentry module with the service module and launch vehicle, the packaging of components so that the center of gravity would permit the desired trim, the more direct applicability of experience gained from the Mercury, Gemini, and similar projects, determined the selection of a blunt reentry module for the Apollo mission.

Although the pull-up phase of the Apollo reentry is now visualized as a constant L/D maneuver, modulation is to be exercised immediately after the pull-up. Figure 53–4 shows two methods of modulation for obtaining the required orientation of the lift vector, namely, pitch modulation with varying C_L
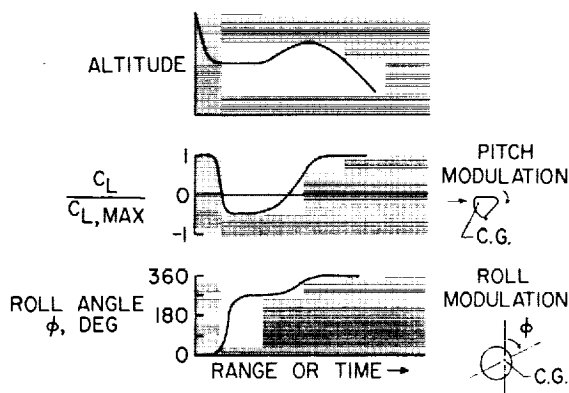

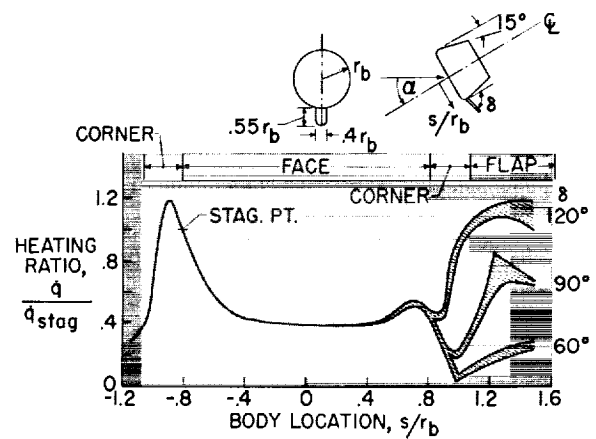FIGURE 53–4.—Simplified examples of pitch and roll modulation.

FIGURE 53–5.—Chin-flap heating on flat-faced model. $M=8$; $\alpha=30°$.

and C_D or roll modulation at constant L/D. At the top of the figure is a plot of altitude as a function of time (or range) for a typical reentry from the middle of the corridor and having a landing point near the center of the footprint. Immediately after completion of the pull-up maneuver in this typical reentry, negative lift is required and is obtained by either pitching to negative angle of attack or rolling at least 90°, respectively, in the two cases. More gradual changes are subsequently required until the reentry finally terminates in a positive-lift equilibrium glide. Not illustrated are the various maneuvers required for additional lateral or longitudial ranges such as those discussed in references 3 and 7. Note that a rapid variation in lift and vehicle orientation is required at the time of peak dynamic pressure at the bottom of the pull-up.

Control heating problems are evident in both of these modulation techniques. The heating problems of a "chin" flap on a flat-faced body of revolution with rounded corners are depicted on figure 53–5. These data were obtained in the Langley Mach 8 hypersonic tunnel at a free-stream Reynolds number, based on model diameter, of 0.22×10^6. This Reynolds number is representative of parabolic reentry for full-scale vehicles at altitudes near 230,000 feet. The ratio of local heating along the plane of symmetry to the stagnation-point heating is plotted as a function of body location. The shaded bands for the flap heating represent the spanwise data variation at a particular position

s/r_b on the flap. The flap heating has a peak approximately 20 percent of the stagnation-point value for $\delta=60°$. At $\delta=120°$, the local heating exceeds the stagnation-point value, and in addition the heating on the body itself ahead of the flap has been increased from under 10 percent of the stagnation value to 100 percent. This last increase is due to the interaction of the shock wave generated by the flap with the flow over the face of the model. Additional information on flap heating may be found in reference 8. Flap heating problems (such as those illustrated) plus the large hinge moments required for rapid attitude change under high dynamic-pressure conditions have led to the conclusion that modulation by roll control using reaction jets is more desirable.

However, reaction jets are not without interference heating problems. Figure 53-6 is a sketch illustrating the results of a temperature-sensitive-paint test for such interference heating. In this technique a model is coated with a paint which changes color with temperature. The model is then suddenly inserted into the test airstream and the color changes are recorded photographically. The heating patterns shown were obtained in the Langley Mach 8 variable-density tunnel with a cold jet located 90° from the plane of symmetry and exhausting upward nearly tangential to the surface (roll jet) or perpendicular to the surface (yaw jet). Note the localized high heating rates (indicated on the sketch by the shaded areas) due to the interaction between the cold reaction jets and the afterbody flow.

At present there is no theory to describe this interaction heating phenomena adequately. However, the rolling moments required are simply inertial and thus are not sensitive to the high dynamic pressures. Furthermore, the other jets, such as pitch and yaw jets, are used only for minor variations in attitude or to counteract the cross coupling of the roll jets and are located away from the windward side. Consequently, these jets will be operative only a small fraction of the time and the heating problem can be handled by adding a little extra heat protection in these critical areas. An experimental investigation is in progress at the
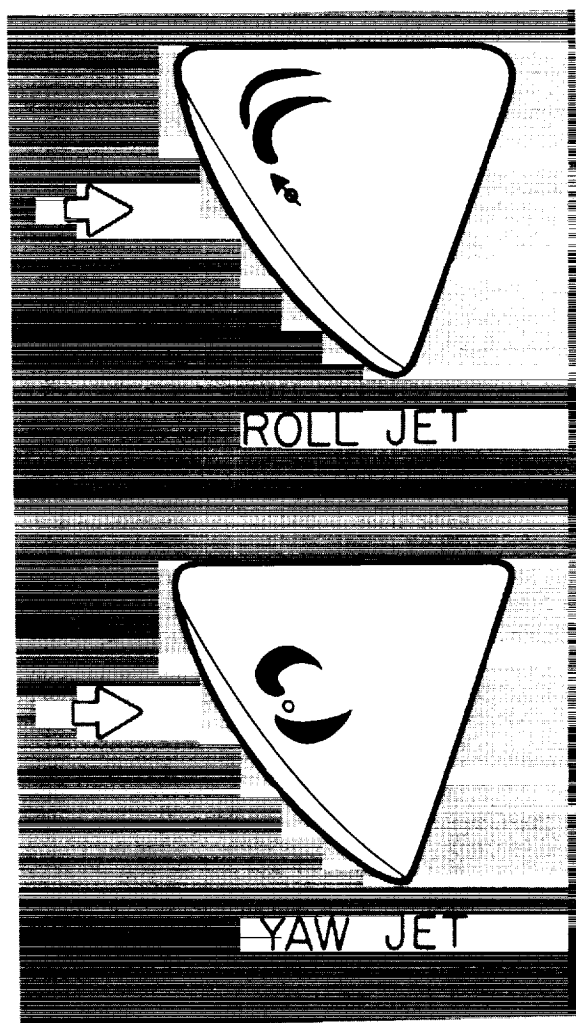

FIGURE 53-6.—Effect of reaction controls on afterbody heating of lunar module.

Langley Research Center to study this problem further.

Another problem associated with reaction jets is the heating to the jet nozzle cavities during the long times when the jets are not operative. This problem is similiar to the heating of cavities discussed in references 9 and 10.

The theoretically predicted heating history of the stagnation point of a 12-foot-diameter lunar reentry module during a 3,500-nautical-mile reentry is shown in figure 53-7. For this prediction, the location of the stagnation point and the stagnation-point velocity gradient were obtained from pressure measurements in the

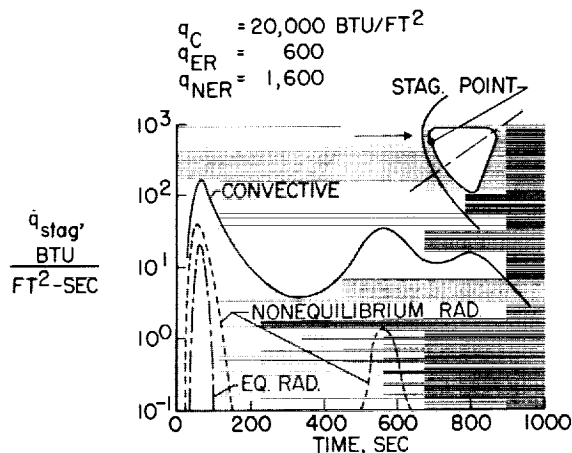q_C = 20,000 BTU/FT^2
q_{ER} = 600
q_{NER} = 1,600

FIGURE 53-7.—Stagnation point heating history for 12-foot-diameter lunar reentry module.

Langley Mach 8 variable-density tunnel. These experiments were necessary because of the lack of a simple adequate theory suitable for configurations in which the stagnation point is located near the rounded corner of an otherwise blunt body at angle of attack. The convective heating q_C was computed by the two-dimensional method of reference 11 for real air in thermochemical equilibrium. Nonequilibrium radiation was computed by use of the data of references 12, 13, and 14 and includes a simple model for the profile of radiation intensity behind the shock wave. The nonequilibrium radiation arises from the very high temperatures (as high as about 60,000° K) which occur just behind the shock wave when all the thermal energy is essentially in the translational and rotational modes excited by a very few molecular collisions. The thermal and chemical relaxation which follows as more collisions take place reduces the temperature toward the equilibrium value, which is of the order of 12,000° K at parabolic entry speed. The nonequilibrium radiation is truncated when the relaxation process has not had sufficient time for completion before the gas has left the stagnation region and started to flow around the body. The nonequilibrium phenomena are discussed more fully in reference 15, as well as in the aforementioned references. Equilibrium radiation q_{ER} was computed from the correlation of reference 16 (based on the absorption coefficients of ref. 17) and a shock shape which was determined by

correcting the shape obtained in the $M=8$ tunnel tests at low density ratios to account for the high density ratios of actual flight. Note that the detachment distance shown in figure 53-7 is exaggerated. More elaborate methods, such as that of reference 18, are available, but these are not uniformly valid for arbitrary shapes and rely on a prior knowledge of certain parameters, such as sonic-point location on the body.

For this trajectory, the stagnation-point convective heating rate and load dominate over the radiative heating rate and load; this result is generally true for lunar reentry. The total radiative load to the stagnation point $q_{ER} + q_{NER}$ indicated on figure 53-7 is only 10 percent of the total convective load q_C for the case illustrated. The equilibrium radiation is very low because the vehicle remains at high altitude (above 200,000 ft) for much of this long-range trajectory. For trajectories of shorter range, the peak equilibrium radiation would be somewhat increased while the peak nonequilibrium value would remain essentially unchanged. The dominant convective peak is about one order of manitude higher than that experienced at the stagnation point of the Mercury spacecraft. The three peaks in convective heating result from a moderate skip after the first pull-up and two subsequent pull-up maneuvers for this trajectory.

The theoretical distribution of heating rate on the lunar reentry module in the plane of symmetry is presented in figure 53-8 for the time of peak stagnation point heating during
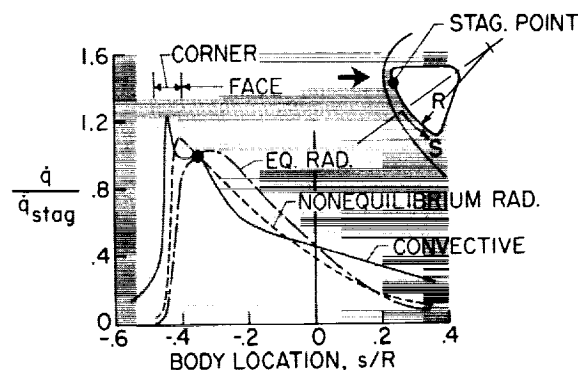

FIGURE 53-8.—Center-line heating rate distribution for lunar reentry module.

240

the reentry shown in figure 53–7. The convective distribution was predicted from a local similarity theory of reference 19 for laminar two-dimensional flow with the real-air boundary-layer results of reference 11. Other theories (refs. 20 and 21) would predict distributions not differing significantly from that shown. Streamline divergence effects (refs. 22 and 23) are not included but should be negligible. Again the Mach 8 variable-density tunnel (ideal gas) pressure distribution was employed. The implication that such a pressure distribution can be used for the prediction of high-velocity heat-transfer distributions is based on the insensitivity of pressure distribution to gas properties and Mach number for blunt forebodies at high Mach number. The heat-transfer theory, itself, is valid for real air in equilibrium. Well-defined experiments are still not available for real air at high enthalpies to validate these methods on asymmetric shapes.

The peak convective heating rate occurs on the rounded corner because of the high local pressure gradient combined with the occurrence here of sonic flow. The convective heating rate decreases rapidly beyond this peak as the flow progresses around to the windward afterbody (on which the heating rates are roughly only 10 percent of the stagnation value). A more gradual decrease is apparent down along the module face, and of course the leeward portions of the afterbody will experience even lower heating rates than will the windward portions. The predictions of afterbody heating are not on too firm ground, especially away from the windward ray, because of the effects of separation and reattachment. Cold-tunnel data obtained in the absence of real-gas effects but with sting or strut support interference is of questionable value in this case. In addition, transition to turbulent flow may be a factor during pull-up for steeper entry angles and this phenomenon is still not well understood.

The peaks in radiative heating are also located at points other than the stagnation point; the nonequilibrium peak is nearer the corner and the equilibrium peak is a short distance down the face. At each point the nonequilibrium radiation was assumed equal to that

emanating from behind a plane two-dimensional shock wave having an incident velocity equal to the local normal component of the free-stream velocity. This approximation appears reasonable when the relaxation length is small compared with the detachment distance, as is the case at peak heating in this trajectory. The nonequilibrium peak on the body thus is located where the bow shock is normal to the free stream—in this case near the corner. The equilibrium radiation distribution was estimated by assuming that each point on the body center line is irradiated by a semi-infinite slab of gas having an emission coefficient equal to the average of the value just behind the local oblique shock and the value at the surface. The slab thickness is given by the local detachment distance and was determined from the Mach 8 variable-density tunnel shock shape scaled to high-speed flight as discussed previously. Thus the peak in this curve on the face below the stagnation point results from the condition that the larger detachment distance more than compensates for the decreased emission coefficients. More elaborate methods for calculations of this type can be made if a knowledge of the flow-field properties and emission-coefficient variation across the shock layer is available. (See refs. 24 and 25.)

In order to design the reentry-module heat protection system, it is necessary that the distribution of heating rate be known away from as well as on the plane of symmetry. Various approximate methods are available. For example, if the surface streamlines and pressure distributions are known, the three-dimensional methods of references 22 and 23 are applicable as long as crossflow is small. Alternately, on the plane through the module center line normal to the plane of symmetry, it has been found that the heat-transfer distribution is adequately predicted by the distribution at zero angle of attack normalized to the value at the center line at angle of attack. Below this plane, the heat transfer on the forebody is roughly constant, and above this plane interpolation may be used to estimate the heating distribution.

The radiative heating histories and distributions do not account for either the absorption of incident radiation by the products of ablation

from the heat shield or for any reradiation from these ablation products to the front face or afterbody. The absorption problem has been investigated (ref. 26) in an overall manner but little appears to have been done on the problem of radiation from the ablation products.

The status of the convective-heating predictions for the manned lunar module might be summed as follows: For the forebody where the heating loads are greatest, predictions appear to be reaching the point where each new refinement to the distribution results in only a small percentage change in the total heat load. In regard to the afterbody, the case is far from settled, but the heating level is so low that even doubling the presently predicted level would change the module heat load by only about 20 percent. However, ablators have a low efficiency for these low heating rates on the afterbody. Thus the afterbody is more important when viewed from weight considerations than when viewed from heating-load considerations. Furthermore, if heating protection for the afterbody were to be provided through reradiation from the hot surface, uncertainty by a factor of 2 in heating rate would result in a 20-percent uncertainty in skin temperature, which could be very significant. Experiments are being conducted on this problem but data obtained in cold tunnels with sting supports is questionable. Finally, although the forebody radiative heating may be uncertain within a factor of 2 (refs. 17, 27, and 28), the design of the forebody heat shield is not critically affected because the contribution of radiation to the total load is so small (about 10 percent).

ENTRY OF PLANETARY PROBES

When the entry of planetary probes is considered, it is found that the velocities encountered are significantly above parabolic. The velocity range of interest for the near future is indicated in figure 53–9. This figure is a plot of the minimum earth entry velocity (for no retrorocket braking) which occurs after a return from Venus or Mars with a given transit time. The minimum-energy (Hohman) transfer velocities are only slightly in excess of parabolic (38,000 feet per second) but require long trip times (259 days for Mars and 146 days for
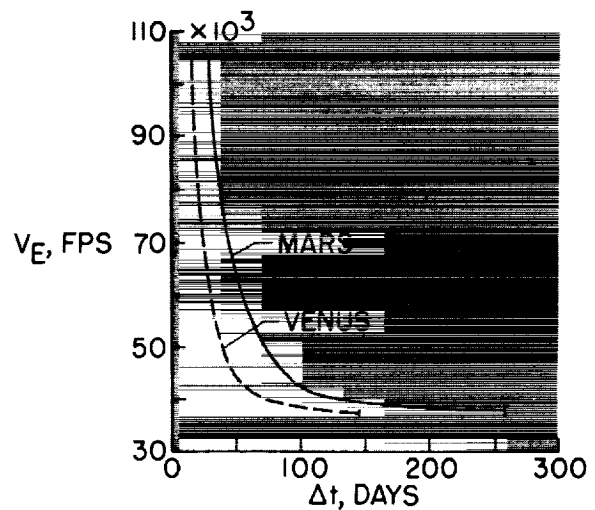

FIGURE 53–9.—Minimum Earth entry velocity as a function of transit time from Mars and Venus.

Venus). In order to reduce this time by a factor of 4, entry velocities of about 50,000 feet per second are required, and to reduce the transit time from Mars to 1 month would require a velocity of 100,000 feet per second.

The principal consideration for such high velocities is the added care which must be given to radiative heating. This fact is evident in figure 53–10 where the total heating load to a 2-foot-diameter sphere in vertical entry is plotted against entry velocity. Contours are also indicated for values of the energy transfer coefficient C_H, which is the ratio of the total heat load during reentry to the kinetic energy of the
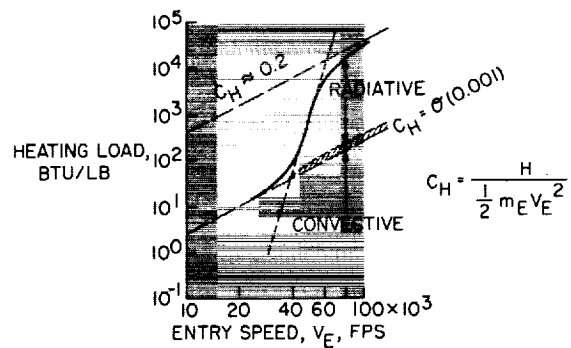

FIGURE 53–10.—Heating load variation with entry speed for 2-foot-diameter sphere.

$$\gamma_E = -90°; \frac{W}{C_D A} = 50 \text{ lb/sq ft.}$$

vehicle at start of reentry. The convective heating contribution has a C_H of the order of 1/1000. The shaded area for $V_E > 40,000$ feet per second represents the present uncertainty in predicting convective heating due to ionization effects on the thermal conductivity of air (refs. 11 and 29 to 32). The short-dashed line is an optically thin adiabatic approximation for the equilibrium radiation heating based on reference 16. The total-heat-load curve deviates from this approximation when the effects of optical thickness and energy loss due to radiation become significant (refs. 33 and 34). The radiative contribution is two orders greater than the convective contribution at the high velocity end of the curve and approaches $C_H \approx 0.2$, an approximate upper limit at high velocities found in reference 35, in which blackbody radiation was assumed and energy loss was accounted for in an approximate manner. This result is consistent with the highest values of radiative heating rates in reference 33, which were about ¼ to ⅓ of the oncoming fluid kinetic energy flux ($\frac{1}{2}\rho_\infty V_\infty^3$) for velocities up to 60,000 feet per second.

Slenderizing the reentry vehicle is one obvious way of alleviating the radiation heating. This possibility is illustrated in figure 53–11 which shows self-illuminated frames from high-speed motion pictures obtained by Jim J. Jones and John A. Moore in the Langely pilot expansion tube (reference 36). The two parts of the figure are reproduced to a scale such that the dotted outlines of the models shown have the same
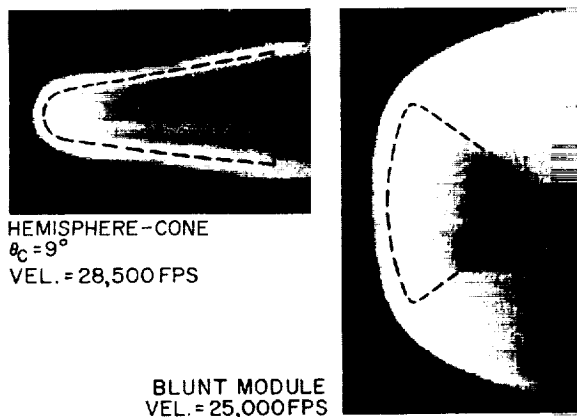

HEMISPHERE-CONE
$\theta_C = 9°$
VEL. = 28,500 FPS

BLUNT MODULE
VEL. = 25,000 FPS

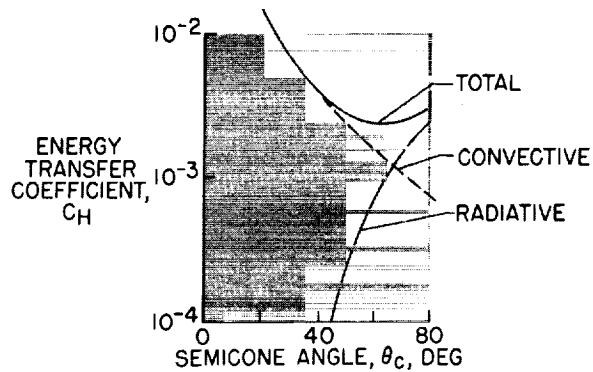Figure 53–11.—Radiation from models in expansion tube.

Figure 53–12.—Heating load variation with θ_c for 2-foot-diameter pointed cones. $V_E = 45,000$ feet per second; $\lambda_E = -90°$; $\frac{W}{C_D A} = 50$ lb/sq ft.

volume. The radiation from the blunter model is much more intense, even though the velocity is much lower (ambient densities are approximately equal).

Since the local radiation intensity varies mainly as the local normal component of the free-stream velocity, further gains in radiative heating can be realized by pointing the blunt nose of the cone. However, elimination of the blunt nose will result in increased convective heating. Figure 53–12 shows the variation with cone angle of radiative, convective, and total heating for a sharp cone. The case illustrated is that of a 2-foot-base-diameter cone with $V_E = 45,000$ feet per second, $\gamma_E = -90°$, and $W/C_D A = 50$ pounds per square foot. (The density of the reentry vehicle thus must change with cone angle.) In this instance, a minimum in the total load appears at $\Theta_c \approx 60°$. The value of Θ_c for minimum heating is, of course, different for other initial conditions and depends upon the radiation model assumed. (See refs. 37 and 38.)

In the preceding discussions of this paper it has been assumed that even though ablation heat shields were employed, the mass loss and vehicle profile change were negligible. Nevertheless, with very high reentry speeds, conditions resulting in high mass loss can arise, and such cases will be considered in the remainder of this paper. These high-mass-loss results are excerpted from a recent analysis made by F. C. Grant of the Langley Research Center, as yet

243

unpublished. The analytical model for this study is shown in figure 53–13. Mass loss is assumed to occur only at the front faces of the cone and cylinder; whereas the sphere loses mass uniformly over its entire surface. Although investigations of such shrinking spheres have been previously made by others (refs. 35, 39, 40, and 41), the sphere is included for completeness. Newtonian drag is assumed for entry into an exponential density atmosphere with a scale height (height for change of a factor e in density) of about 25,200 feet. The reentry is steep with a straight-line trajectory and the gravitational force neglected (ref. 42). The final mass m_f, which might consist of payload instrumentation plus an allowance for structure and other weights, is so located that it generates no aerodynamic forces. The heating rate per unit area follows the law $\dot{q}=\eta(\tfrac{1}{2}\rho_\infty V_\infty^3)$, where η is assumed constant during reentry. An upper boundary of $\tfrac{1}{2}$ for η appears reasonable. If radiation is the predominant heating mode, then at most $\tfrac{1}{2}$ of the total energy flux will be radiated toward the body and $\tfrac{1}{2}$ will be radiated back into the atmosphere ahead of the vehicle. (The case of the absorption of this forward radiation by the atmospheric gases ahead of the shock, which then approach the vehicle with increased energy, is not considered herein but is discussed in ref. 37.) In reference 33 the theoretical predictions of η on a one-dimen-
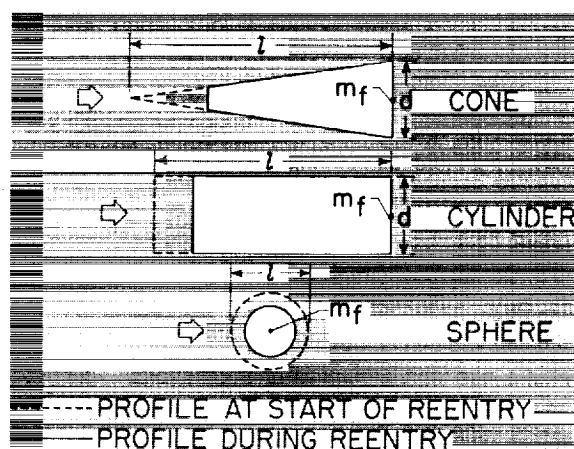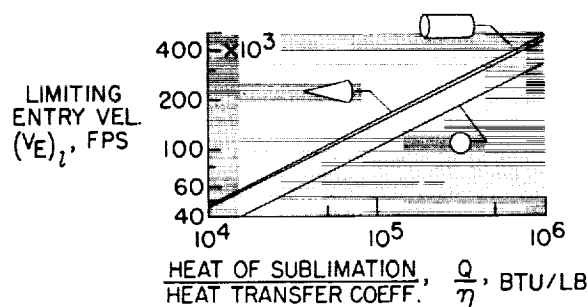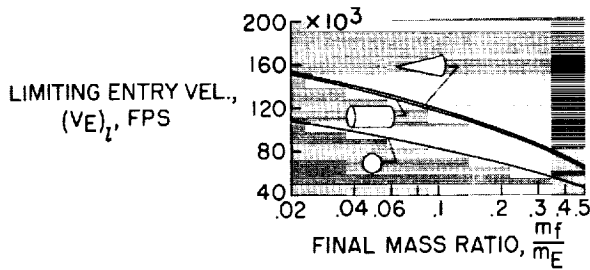

FIGURE 53–14.—Effect of heat of sublimation and heat-transfer coefficient on $(V_E)_l$.

$$\frac{m_f}{m_E}=0.125;\ \theta_c\approx 8.5°.$$

sional basis for velocities up to 60,000 feet per second are less than approximately $\tfrac{1}{4}$ for altitudes below 100,000 feet, which is the limit of the altitude range of interest for this analysis.

Before this matter is discussed further, it should be noted that although the cones are shown to be sharp in the illustrations, the assumption is made that an arbitrarily small initial bluntness exists, which will then grow rapidly as a result of radiation heating. Reference 38 discusses the possibility of special body contouring in order to realize the appreciable gains of a body which can retain a pointed shape during mass loss.

The next problem to be discussed is concerned with the effect of certain parameters on the limiting entry velocity $(V_E)_l$. This velocity is defined as that entry velocity which will cause ablation during reentry of all the mass of the vehicle with the exception of the final mass m_f. The variation of $(V_E)_l$ with the quotient Q/η (heat of sublimation divided by heat-transfer coefficient) is plotted in figure 53–14 for a final mass ratio $m_f/m_E=0.125$. The cone angle $\theta_c=8.5°$ so that heating of the conical flanks is negligible. The heat of sublimation is employed rather than the effective heat of ablation because radiation is the predominant heating mode during the period of high mass loss for the reentries considered. The difference between the heat of ablation and heat of sublimation may be considered then to block the convective heating. At a given value of Q/η, the limiting velocity is nearly the same for the cone and cylinder while that of the sphere is 50 percent


FIGURE 53–13.—Model used for high-speed high-mass-loss analysis.

HEATING LAW: $\dot{q}=\eta\left(\dfrac{1}{2}\rho_\infty V_\infty^3\right)$

FIGURE 53-15.—Effect of final mass ratio on $(V_E)_l$.

$$\frac{Q}{\eta}=\frac{15,000}{1/4}=60,000 \text{ Btu/lb}; \ \theta_c=8.5°.$$

smaller. The limiting velocity varies as the square root of Q/η.

The effect of final mass ratio on limiting velocity is shown in figure 53-15. The value of $Q/\eta=15,000/(¼)=60,000$ Btu per pound (selected for illustration) is composed of values of Q representative of the heat of sublimation for graphite together with a conservative value of ¼ for η. As expected, $(V_E)_l$ decreases as the final mass ratio increases; however, even for this conservative value of Q/η, velocities of 70,000 feet per second are possible with mass fractions of ½.

The data in figures 53-14 and 53-15 indicate that very high limiting entry speeds are possible with substantial final mass fractions and that the pointed cones and cylinders are superior to the sphere. However, one of the prices that must be paid for such reentries appears in figure 53-16, which is a plot of maximum decel-
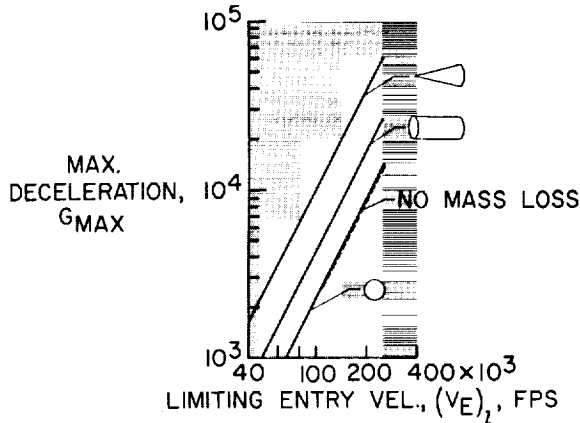
FIGURE 53-16.—Relation between G_{max} and $(V_E)_l$.

$$\frac{m_f}{m_E}=0.125; \ \theta_c \approx 8.5°.$$

eration, in earth gravitational units, as a function of $(V_E)_l$. The G-magnitude is extreme, ranging from 10^3 to 10^5, and varies as the square of the entry velocity. Much higher loadings are experienced by the cone and cylinder than by the sphere. For the case of zero mass loss at an entry velocity equal to $(V_E)_l$ the maximum deceleration is nearly identical to that of the high-mass-loss sphere. After a quick inspection of this curve it is obvious that such reentries will be unmanned.

An interesting point regarding figures 53-14, 53-15, and 53-16 should be mentioned. First, there is no dependency of $(V_E)_l$ on the size $(_l)$ of the vehicle. This independence results from the fact that in these figures no restriction was placed on the lower extent of the atmosphere; that is, the atmosphere has been assumed to increase exponentially as the altitude decreases until the vehicle has completed its deceleration without regard to the final altitude. Of course, when the practical boundary condition that the vehicle must have finished its deceleration before impact with the earth's surface is imposed, then the size of the vehicles becomes limited since the G-pulse occurs at lower altitudes for larger $_l$. Inasmuch as the velocity ultimately has an exponential decay with altitude, the deceleration never vanishes completely. Thus, some convention must be adopted to define the end of the deceleration pulse. In this paper the limiting size will be defined as that value of $_l$ which puts the peak G point at 1 and 2 scale heights above sea-level for the cones and cylinders, respectively. The vehicles are then so limited in size that the velocity at sea level is less than 1,000 feet per second for the cones and 150 feet per second for the cylinders at $m_f/m_E=½$. For smaller values of m_f/m_E, smaller sea-level velocities occur. The values of 1,000 and 150 feet per second are for a Q/η value of 60,000 Btu per pound, but may be readily scaled to other Q/η values since all velocities scale as $\sqrt{Q/\eta}$.

This limiting vehicle size is shown in figure 53-17 for the cone $(\theta_c=8.5°)$ and cylinder. The sphere is not shown because it has negligible size under the aforementioned impact-velocity restrictions. The curves are drawn for $Q/\eta=60,000$ Btu per pound, and a material density w of 140 pounds per cubic foot, a value
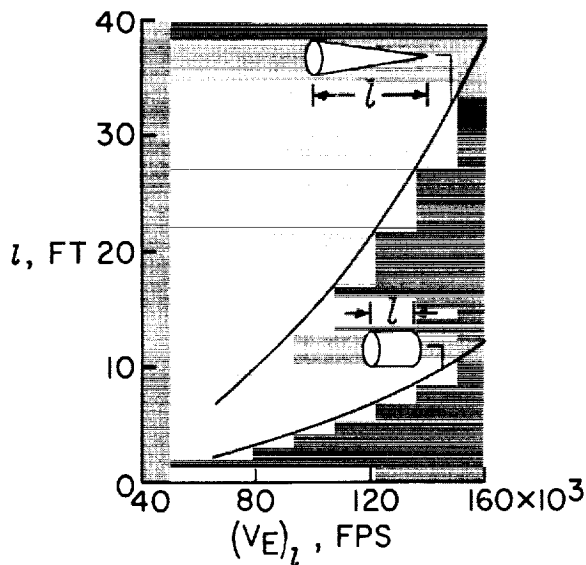
FIGURE 53-17.—Limiting size for deceleration before impact. $w=140$ lb/cu ft; $Q/\eta=60,000$ Btu/lb; $\theta_o=8.5°$.

also typical of graphite. The value of the final mass fraction m_f/m_E varies along these curves with the lower values occurring at the higher velocities. At $(V_E)_i=100,000$ feet per second, the limiting length of an 8.5° cone is 15 feet.

The weights (sizes) required to return a specified final weight to earth after entry from a particular limiting velocity are illustrated in figure 53-18. Curves are drawn for cylinders of $d/l=0.3$, 0.6, and 1.2 and for the cone with $\theta_c=8.5°(d/l=0.3)$. Again the impact velocity is restricted and values of $Q/\eta=60,000$ Btu per pound and a density of 140 pounds per cubic foot are used. The ticks on the curve give the gross vehicle weight at start of reentry. If curves of these gross entry weights were to be cross plotted one would find that the cone is

only slightly more efficient (smaller entry weight for given final weight) than the cylinders. For cylinders at a given $(V_E)_i$ the d/l must increase as the final weight increases because l and m_f/m_E are constant; and at a given final weight, the d/l ratio decreases with increasing $(V_E)_i$. A typical example using this figure would show that a 2,000-pound final weight could be reentered at about 65,000 feet per second using a graphite cylinder with a $d/l=1.2$. The entry vehicle would have a gross weight of 4,000 pounds, a diameter of 2.8 feet, and a length of 2.3 feet. The w/C_DA would vary from 310 to 155 during reentry.

The estimates of this high-mass-loss analysis indicate that sizable payload fractions can be recovered after the reentry of unmanned high-speed planetary probes having gross weights and sizes compatible with future launch vehicles. However, the final optimization and sophistication of these reentry probes must be preceded by further knowledge and detailed studies of the radiative and convective heating at these extreme speeds.
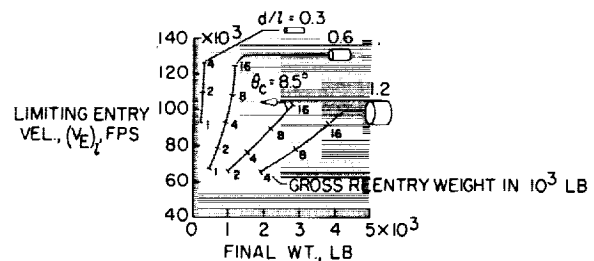

FIGURE 53-18.—Limiting entry velocity and final weight for deceleration before impact.

$$\frac{Q}{\eta}=\frac{15,000}{1/4}=60,000 \text{ Btu/lb}; \; w=140 \text{ lb/cu ft.}$$

REFERENCES

1. CHAPMAN, DEAN R.: An Analysis of the Corridor and Guidance Requirements for Supercircular Entry Into Planetary Atmospheres. NASA TR R-55, 1960.
2. BARADELL, D. L.: Range Control During Initial Phases of Supercircular Reentries. Thesis sumbitted to Virginia Polytechnic Institute in Partial Fulfillment of the Requirements for the Degree Master of Science in Aerospace Engineering, May 1962.
3. BECKER, J. V., BARADELL, D. L., and PRITCHARD, E. B.: Aerodynamics of Trajectory Control for Reentry at Escape Speed. Astronautica Acta, vol. VII, 1961, pp. 334-358.

4. LEES, LESTER, HARTWIG, FREDERIC W., and COHEN, CLARENCE B.: The Use of Aerodynamic Lift During Entry Into the Earth's Atmosphere. ARS Jour., vol. 29, no. 9, Sept. 1959, pp. 633-641.

5. GRANT, FREDERICK C.: Importance of the Variation of Drag With Lift in Minimization of Satellite Entry Acceleration. NASA TN D-120, 1959.

6. GRANT, FREDERICK C.: Analysis of Low-Acceleration Lifting Entry From Escape Speed. NASA TN D-249, 1960.

7. BARADELL, DONALD L.: Lateral Range Control by Banking During Initial Phases of Supercircular Reentries. NASA TN D-1511, 1962.

8. JONES, ROBERT A.: Heat-Transfer and Pressure Distributions on a Flat-Face Rounded-Corner Body of Revolution With and Without a Flap at a Mach Number of 8. NASA TM X-703, 1962.

9. BERTRAM, MITCHELL H., FETTERMAN, DAVID E., JR., and HENRY, JOHN R.: The Aerodynamics of Hypersonic Cruising and Boost Vehicles. NASA University Conference, 1962. (Paper No. 55 of present compilation.)

10. CHARWAT, A. F., DEWEY, C. F., JR., ROOS, J. N., and HITZ, J. A.: An Investigation of Separated Flows—Part II: Flow in the Cavity and Heat Transfer. Jour. Aerospace Sci., vol. 28, no. 7, July 1961, pp. 513-528.

11. COHEN, NATHANIEL B.: Boundary-Layer Similar Solutions and Correlation Equations for Laminar Heat-Transfer Distribution in Equilibrium Air at Velocities up to 41,000 Feet Per Second. NASA TR R-118, 1961.

12. CAMM, J. C., KIVEL, B., TAYLOR, R. L., and TEARE, J. D.: Absolute Intensity of Non-Equilibrium Radiation in Air and Stagnation Heating at High Altitudes. Res. Rep. 93 (AFBMD TR 60-184), AVCO-Everett Res. Lab., Dec. 1959.

13. TEARE, J. D., GEORGIEV, S., and ALLEN, R. A.: Radiation from the non-equilibrium Shock Front. Res. Rep. 112, AVCO-Everett Res. Lab., Oct. 1961.

14. CANNING, THOMAS N., and PAGE, WILLIAM A.: Measurements of Radiation from the Flow Fields of Bodies Flying at Speeds up to 13.4 Kilometers Per Second. Presented to the Fluid Mechanics Panel of AGARD (Brussels, Belgium), Apr. 3-6, 1962.

15. CANNING, THOMAS N.: Recent Developments in the Chemistry and Thermodynamics of Gases at Hypervelocity. NASA University Conference 1962. (Paper No. 59 of present compilation.)

16. THOMAS, P. D.: Air Emissivity and Shock Layer Radiation. Jour. Aerospace Sci. (Readers Forum), vol. 29, no. 4, Apr. 1962, pp. 477-478.

17. MEYEROTT, R. E., SOKOLOFF, J., and NICHOLLS, R. W.: Absorption Coefficients of Air. Rep. No. LMSD 288052, Lockheed Aircraft Corp., July 1960.

18. KAATTARI, GEORGE E.: Predicted Shock Envelopes About Two Types of Vehicles at Large Angles of Attack. NASA TN D-860, April 1961.

19. BECKWITH, IVAN E., and COHEN, NATHANIEL B.: Application of Similar Solutions to Calculation of Laminar Heat Transfer on Bodies with Yaw and Large Pressure Gradient in High-Speed Flow. NASA TN D-625, 1961.

20. LEES, LESTER: Laminar Heat Transfer Over Blunt-Nosed Bodies at Hypersonic Flight Speeds. Jet Propulsion, vol. 26, no. 4, Apr. 1956, pp. 259-269, 274.

21. KEMP, NELSON H., ROSE, PETER H., and DETRA, RALPH W.: Laminar Heat Transfer Around Blunt Bodies in Dissociated Air. Jour. Aero/Space Sci., vol. 26, no. 7, July 1959, pp. 421-430.

22. VAGLIO-LAURIN, ROBERTO: Laminar Heat Transfer on Three-Dimensional Blunt Nosed Bodies in Hypersonic Flow. ARS Jour., vol. 29, no. 2, Feb. 1959, pp. 123-129.

23. BECKWITH, IVAN E.: Similarity Solutions for Small Cross Flows in Laminar Compressible Boundary Layers. NASA TR R-107, 1961.

24. WICK, BRADFORD H.: Radiative Heating of Vehicles Entering the Earth's Atmosphere. Presented to the Fluid Mechanics Panel of AGARD (Brussels, Belgium), Apr. 3-6, 1962.

25. ANON.: Study of Thermal Radiation Associated with Non-Equilibrium Flow in the Apollo Flight Regime. Doc. No. AERL 62-702, Ser. A (Contract No. NAS 9-156), AVCO-Everett Res. Lab., Sept. 1962.

26. HOWE, JOHN THOMAS: Shielding of Partially Reflecting Stagnation Surfaces Against Radiation by Transpiration of an Absorbing Gas. NASA TR R-95, 1961.

27. KIVEL, B., and BAILEY, K.: Tables of Radiation From High Temperature Air. Res. Rep. 21 (Contracts AF 04(645)-18 and AF 49(638)-61), AVCO Res. Lab., Dec. 1957.

28. Breene, R. G., Jr., and Nardone, Maria: Radiant Emission from High Temperature Equilibrium Air. R61SD020, Space Sci. Lab., Gen. Elec. Co., May 1961.

29. Adams, Mac C.: A Look at the Heat Transfer Problem at Super-Satellite Speeds. [Preprint] 1556–60, American Rocket Soc., Dec. 1960.

30. Hoshizaki, H.: Heat Transfer in Planetary Atmospheres at Super-Satellite Speeds. ARS Jour., vol. 32, no. 10, Oct. 1962, pp. 1544–1551.

31. Scala, Sinclaire M., and Warren, Walter R.: Hypervelocity Stagnation Point Heat Transfer. ARS Jour., vol. 32, no. 1, 1962, pp. 101–102.

32. Fay, James A.: Hypersonic Heat Transfer in the Air Laminar Boundary Layer. Presented at AGARD Hypersonic Specialists' Conference (Brussels, Belgium), Apr. 3–6, 1962.

33. Yoshikawa, Kenneth K., and Chapman, Dean R.: Radiative Heat Transfer and Absorption Behind a Hypersonic Normal Shock Wave. NASA TN D–1424, 1962.

34. Kennet, H., and Strack, S. L.: Stagnation Point Radiative Transfer. ARS Jour., vol. 31, no. 3, Mar. 1961, p. 370.

35. Riddell, Frederick R., and Winkler, Howard B.: Meteorites and Re-Entry of Space Vehicles at Meteor Velocities. ARS Jour., vol. 32, no. 10, Oct. 1962, pp. 1523–1530.

36. Trimpi, R. L.: A Preliminary Study of a New Device for Producing High-Enthalpy, Short-Duration Gas Flows. For presentation at Second National Hypervelocity Techniques Symposium (Denver, Col.), March 19–20, 1962.

37. Allen, H. Julian: Hypersonic Aerodynamic Problems of the Future. Presented to the Fluid Mechanics Panel of AGARD (Brussels, Belgium), Apr. 3–6, 1962.

38. Allen, H. Julian: Gas Dynamic Problems of Space Vehicles. NASA University Conference, 1962. (Paper No. 57 of present compilation.)

39. Öpik, Ernst J.: Physics of Meteor Flight in the Atmosphere. Interscience Publishers, 1958.

40. Hoppe, J.: Die physikalischen Vorgänge beim Eindringen meteorische Körper in die Erdatmosphäre. Astronmomische Nachrichten, vol. 262, 1937, pp. 169–198.

41. Hansen, C. Frederick: The Erosion of Meteors and High-Speed Vehicles in the Upper Atmosphere. NACA TN 3962, March 1957.

42. Allen, H. Julian, and Eggers, A. J., Jr.: A Study of the Motion and Aerodynamic Heating of Ballistic Missiles Entering the Earth's Atmosphere at High Supersonic Speeds. NACA Rep. 1381, 1958.